A ONE DIMENSIONAL DRY FRICTION MICROCONVEYOR PLATFORM: MODELLING AND ANALYSIS OF MICROPART MOTION DUE TO SURFACE EXCITATION

by

MOHSIN RIZWAN

Presented to the Faculty of the Graduate School of
The University of Texas at Arlington in Partial Fulfillment
of the Requirements
for the Degree of

DOCTOR OF PHILOSOPHY

THE UNIVERSITY OF TEXAS AT ARLINGTON

December 2011

To My Beloved Father

ACKNOWLEDGEMENTS

I would like to express my deepest gratitude to everyone who contributed and helped me complete this research work. I am thankful to my dissertation advisor P. S. Shiakolas for his intellectual contribution and moral support. Without his thoughtful guidance and technical support, I would have not been able to complete this dissertation. Thanks to my advisory committee: Dr. Seiichi Nomura, Dr. Kent Lawrence, Dr. Alan Bowling and Dr. Pranesh Aswath. I am thankful to the Mechanical and Aerospace Engineering Department for their continuous support in helping me achieve this milestone successfully.

I would have not been able to accomplish this success without the encouragement and support of my family. I am highly indebted to my parents who encouraged me to continue the studies. I am thankful to my brother and my sisters who managed my share of family affairs which allowed me to have spare time and concentrate towards my research. This milestone would have never been achieved without their love and encouragement.

November 21, 2011

ABSTRACT

A ONE DIMENSIONAL DRY FRICTION MICROCONVEYOR PLATFORM: MODELLING AND ANALYSIS OF MICROPART MOTION DUE TO SURFACE EXCITATION

Mohsin Rizwan, PhD

The University of Texas at Arlington, 2011

Supervising Professor: P. S. Shiakolas

Many approaches are used for micropart manipulation ranging from individual pick and place to manipulation through a workcell comprising of arrays of actuators. Existing approaches provide discrete actuation and have limitations on the lower bound on the size of the micropart to be handled. In this research, the active surface concept for non-contact micropart manipulation is investigated. The active surface deformation is generated by a set of controlled microactuators and provides for continuous micromanipulation while alleviating limitations of existing approaches.

The drastic increase of surface area to volume ratio from macroscale to microscale requires the consideration of surface forces (such as van der Waals and Casimir) in any dynamic model for micropart motion. In this research, the dynamics of micropart (approximate dimensions of 100 um) on a flexible surface is developed accommodating this shift of dominance from body to surface forces. The dynamic bidirectional effects of the nanoscale surface roughness and microscale forces on each other are analysed and studied in a dynamic model to assess the friction force between the micropart and carrier surface based on augmenting the Kogut-Etsion friction model. The developed highly nonlinear dynamic model is then applied to study the motion of a micropart on a carrier surface under controlled deformation

due to an attached microactuator. The effects of the various system parameters on the controlled micropart translocation are studied where is found that there are ranges in which translocation takes place or that the micropart becomes airborn and detaches from the carrier surface. The developed model is expanded and applied for an array of microactuators for the realization of a continuous microconveyor platform in a dry friction environment through parametric studies and constrained optimization approach indicating that a microconveyor platform could be realized based on the proposed approach and model.

TABLE OF CONTENTS

LIST OF ILLUSTRATIONS

FIGURES PAGE

LIST OF TABLES

Table Pages

CHAPTER 1

INTRODUCTION

For a long time in the history of technological advancement, the innovation was limited to the introduction of new theories and new concepts and their applications. Driven by the requirement of ease of handling and the concept of multifunctionality, a new area in technical advancement emerged which was to reduce existing hardware size while keeping the desired functionality of the system. This desire of miniaturization led to the beginning of MEMS era. In addition to fulfilling the requirement of existing hardware, these systems could be operated with higher accuracy and produce more precise results. MEMS development does not require only a simple reduction on manufacturing scales but requires also the consideration of physical phenomena giving rise to new fields in science and engineering. MEMS design, manufacturing, handling, assembly and operation require the development of fundamentally new technologies and the definition of new parameters not accounted for at the macro scale. Because of the fast pace of ongoing research in this field which is pushed by comparatively low probability of successful MEMS operation compared to meso and macro scales, each of the above mentioned areas turned into a field of specialization in itself. This research is an effort to addresses a small area relating to micropart or MEMS handling and manipulation.

1.1 Motivation

Micropart manipulation and handling methodologies are different from those found at the macroscale. The scale differences require consideration of microforces and microscale phenomena as fundamental modeling components. The continuous advancement in micropart handling is the result of the need to produce accurate manipulation approaches and augment the existing methodologies with improved fidelity mathematical models. This research is influenced by similar motivations and a new approach for micropart manipulation is explored through modeling, simulation and optimization principles.

Manipulation of small parts is essential in microassembly automation in order to improve assembly processes for mass production of homogeneous and heterogeneous MEMS. The conventional approach to handle microparts is to pick and assemble individual workpieces as required. For individual handling, the workpiece needs to be located precisely or the system needs to be supported by visual assistance and feedback. The alternate approach is to use a workcell to manipulate and accurately locate a workpiece.

Various types of workcells have been proposed with a large variety in design and operation mechanisms. These workcells employ mechanical, pneumatic or electromechanical manipulation mechanisms to move and locate the workpiece at a desired position. Most of the existing methodologies discuss the workpiece convergence to the desired location and the operation of the manipulation mechanism but they do not explain the interaction of the micropart with the workcell. The proposed approach addresses this issue through the development of a mathematical model of the workpiece interacting with the workcell which is employed to study the workpiece motion based on the various physical and control parameters. The performance characteristics of the proposed method can be determined, and the system can be fine-tuned to meet performance requirements using the developed mathematical model.

1.2 Contributions

The proposed manipulation approach consists of a surface and a series of attached microactuators to controllably deform the surface. The controlled surface deformation imparts an inertia force on the micropart initiating the motion of the micropart along the deformed surface. An array of actuators forms a microconveyor platform which could be used for controlled translocation of microparts.

This research focuses on the development of the proposed microconveyor concept by introducing the necessary parameters required to define the system, developing a mathematical model for micropart motion on a flexible surface considering the dynamically changing microforces and eventual motion analysis of the micropart. The contributions of this research are presented in summary form.

1.2.1 *Development of a mathematical model considering microscale forces and phenomena and numerical approach for micropart motion*

The system mathematical model is developed to simulate the micropart motion in a dry friction environment on a flexible surface. The milestones in developing the mathematical model are

- Identify the dominant forces for microscale system modeling.
- Conduct a comprehensive study of the surface contact models in the open literature, select the surface model suitable for microscale system modeling and evaluate the attraction force and friction force as function of surface roughness.
- Identify the governing equations for micropart motion considering dominant surface forces. Augment the dynamic motion modeling equations with the surface contact model. Invert the surface contact model to accommodate the sequential evaluation of unknown parameters from the system inputs.
- Establish the feasibility of micropart motion using the developed mathematical model and identify lower and upper bounds on microactuator motion parameters.

1.2.2 *Sensitivity analysis of micropart motion*

The translocation distance of a micropart depends on the system physical and control parameters. The influence of each individual parameter on the system output is analyzed through a qualitative and quantitative analysis.

1.2.3 *Micropart motion analysis for multiactuator system with discrete firing*

- The feasibility of array of actuators is established. The new parameters for a complete definition of multiactuator system are defined. The effect of additional parameters on the system performance is estimated.
- The optimum set of system parameters for a desired system performance is estimated using constrained optimization.

1.2.4 *Analysis of effect of surface stretch on surface stretch and micropart motion*

The surface stretching during deformation affects the roughness of the deformable surface. The changes in surface roughness and their effects on the micropart translocation are analyzed. A mathematical model is developed to estimate the changes in surface roughness characteristics as function of dynamically deformed surface geometry.

1.3 Summary

Following this introduction, a detailed survey of existing techniques of part manipulation is presented. Manipulation methodologies along with their respective limitations are discussed. In chapter 3, a new method of MEMS manipulation based on the concept of active surface has been proposed. A micropart resting on a flexible surface can be manipulated using controlled deformation of the flexible surface. A workcell consisting of a series or an array of actuators could translocate the microparts from one place to the other. The mathematical model for the system dynamics is developed along with a review of contact models used to model surface roughness. Micropart motion feasibility, dynamic analysis and workcell functionality only in one dimension are discussed and established. A sensitivity analysis of micropositioning as function of material and workcell parameters due to a single actuator is performed with a discussion of both the qualitative and quantitative results.

The microconveyor concept as a series of microactuators is introduced and modeled in order to evaluate its performance in Chapter 4. The interaction of cascading actuators and their effects on system output are discussed. The system response for multi-actuator setup is studied for various input parameters along with an optimization scheme (based on genetic algorithms/differential evolution) to estimate the best parameter values for a particular system output.

The assumption of constant surface roughness is relaxed in chapter 5, and the effects of surface stretching on the surface roughness are calculated and accommodated in the resultant output. The outputs from constant and relaxed surface roughness models are compared to understand the effects of the dynamic change of surface roughness.

The last chapter deals with the conclusions of the research and some recommendations and suggestion for the future work. The future work discusses the possibility to invert the information of the resultant surface for a given input and calculate system input depending upon the requirement for a given target position.

CHAPTER 2

HISTORY OF MICROPART MANIPULATION

2.1 Introduction

Micropart manipulation has been of interest in the MEMS community. The micropart manipulation approaches cover a wide range of techniques from pick and place of an individual item using a microgripper to the automatic handling of microparts using various types of workcells. The basic idea of automatic manipulation started from the requirement of automatic orientation of macro scale parts on a conveyor belt to help automated packaging of goods and to conduct manufacturing operations such as stamping, injection etc. Depending upon the requirement of the process, many types of micromanipulation approaches have been proposed which can be categorized in two broad categories: Contact micromanipulation and contactless micromanipulation.

Contact micromanipulation refers to a broad range of approaches covering workpiece manipulation with physical contact with an end effector or workcell. The physical contact generates the required force for controlled manipulation. These techniques include inertial and thermodynamic microgrippers, vacuum nozzles, microtweezers, and workcells comprising of an array of actuators for direct manipulation.[1]

Contactless micromanipulation refers to those methodologies where the workpiece has no direct physical contact with an actuator and the medium between the two transfers the actuator force to the workpiece. Optical tweezers, pneumatic tweezers, microfluidic assisted acoustic manipulation, compressed air assisted manipulation and ice grippers are some of the examples where the workpiece is not in direct contact with the actuator. [1, 2]

Another broader classification of part manipulation methodologies is based on the number of actuators; single actuator devices such as microgrippers, tweezers, graspers and actuator platforms comprising of a pattern of actuators.

The actuator platform type workcells are equipped with arrays of actuators that can translocate the micropart in a controlled fashion and depending upon the process requirement, may eliminate the need of grippers. For mass production of MEMS components, the platform type workcell can be used along with a single micropart manipulator to arrange, translocate and assemble the parts from a random initial orientation and location to a pre-defined final destination and orientation. In addition actuator platforms can handle workpieces with a wide variety of shapes whereas grippers usually have capability to handle only limited types of shapes.

In this research a new approach for micropart manipulation is proposed. The existing workcells consist of cascades of discrete actuators to manipulate the workpiece. The new proposed approach provides continuous actuation along the surface of the workcell.

A brief overview of the evolution of workpiece micromanipulation is presented. In addition, the hardware of various available types of workcells, their functionality and their advantages and limitations will be discussed. The requirements for a new manipulation technique which can overcome some of the constraints of the existing approaches of micropart handling will be discussed.

2.2 Historical Background

The area of automated part handling emerged in early 1960's when pushed by the need to handle the randomly oriented macro/meso scale parts and achieve final orientation for automatic assembly or packaging. [3] To orient the random-shaped parts with random unknown initial orientation, a computer controlled manipulator with an open box attached to a vibrator, was proposed by Grossman and Blasgen [4]. Parts when dropped into the box assume one of the finite possible orientations. The manipulator orients the macro sized parts into the desired orientation once a particular stable orientation in the box is established.

Erdman, inspired by the work from Grossman and Blasgen, proposed a tilting tray apparatus and developed a planner to orient and position the objects [5]. The basic idea of the tilting tray orienter is shown in Figure 2.1 where simple meso-size objects such as allen keys were used to prove the proposed algorithm. Utilizing the developed planner, for a given shape, the number of tilts of a rectangular tray could be calculated to obtain a final desired orientation. Depending upon the number of nodes (number of corners of a polygonal workpiece) of the objects the final orientation could be obtained for most of the parts but there was no solution for parts with rotational symmetries such as cylindrical sections and the sufficient condition to establish that a task was not solvable could not be established. The approach was used mainly for macro sized workpieces.

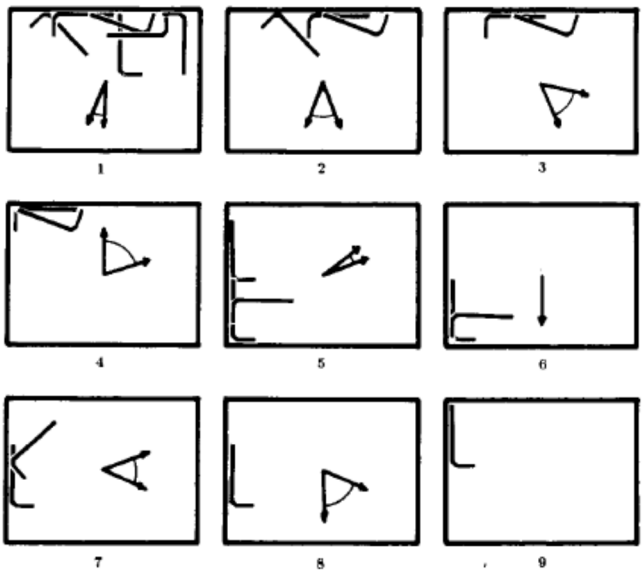

Figure 2.1: The calculated tilt of tray with the resultant movement of an allen key. Each operation is represented by an interval of azimuths. The azimuth arrows indicate the direction of steepest ascent [5]

Hitakawa proposed a parts feeder that uses an array of nests cut into a vibrating plate [6]. The nests and the vibratory motions are designed so that the part will remain in the nests only in a particular orientation. By tilting the plate and letting parts flow across it, the nests eventually fill up with parts in the required orientation. For parts with infinite friction the final orientation, if one exists, can be achieved within $O(n^4)$ times where n is the number of the sides of the polygon[7]

Goldberg developed algorithms to help in orientating the objects using a parallel jaw gripper [8]. The schematic of the process is shown in Figure 2.2 with series of parallel jaw grippers to achieve the final orientation. He proposed algorithms to calculate the number of moves by the parallel gripper to orient an object from a random initial orientation to a predefined final orientation. For a convex shape with "n" nodes, the required orientation can be achieved within $O(n^2 log(n))$ moves. The algorithms were applicable only to convex shapes. Concave shapes were handled by replacing their outline with an equivalent convex shape. Macro sized parts were handled with the parallel jaw gripper to reach the final desired orientation.

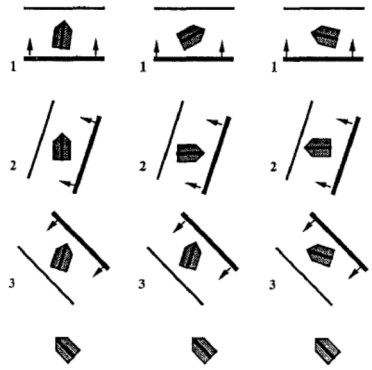

Figure 2.2: Part coming in different initial configuration, passing through a series of parallel jaw gripper, converge to a unique final orientation [8]

With the advancements in technology and to extend the existing techniques for miniature applications, the research and manufacturing trend shifted towards development of MEMS in the last couple of decades. Among other problems at the micro-nano scale, one of the biggest issues is controlled micropart placement for assembly. Micron-sized parts are placed at the required location and pick and place technique is used to help with micro assembly. For microparts the weight of the part is a negligible quantity compared to the surface forces such as van der Waal's force, electrostatic force of attraction and Casimir attraction etc. Thus, traditional pick and place cannot be used successfully for smaller parts. For smaller sized parts the surface area to volume ratio is very high making the surface forces to dominate the weight of the part. Any approach for micropart handling must be appropriately modified to accommodate these surface forces.

Bohringer, continuing and extending Goldberg's idea, proposed the concept of force-field to move and orient workpieces. Using the force field approach Bohringer proposed that starting from a random initial orientation; a particular final orientation can be reached through a force field generated by a set of actuator arrays that could generate the force field [9]. At the macro scale the idea was implemented with the help of a vibrating plate as shown in Figure 2.3 [10]. The forced vibration of a plate at a controlled frequency will excite specific natural modes of vibration. While on the vibrating plate, the workpiece will have tendency to reach the nodal position and orient itself. At the micro scale, it was implemented with the help of arrays of micromanipulators [11]. The convergence of motion of the workpiece translocated to the desired orientation by the workcell was proven using the limit surfaces[12].

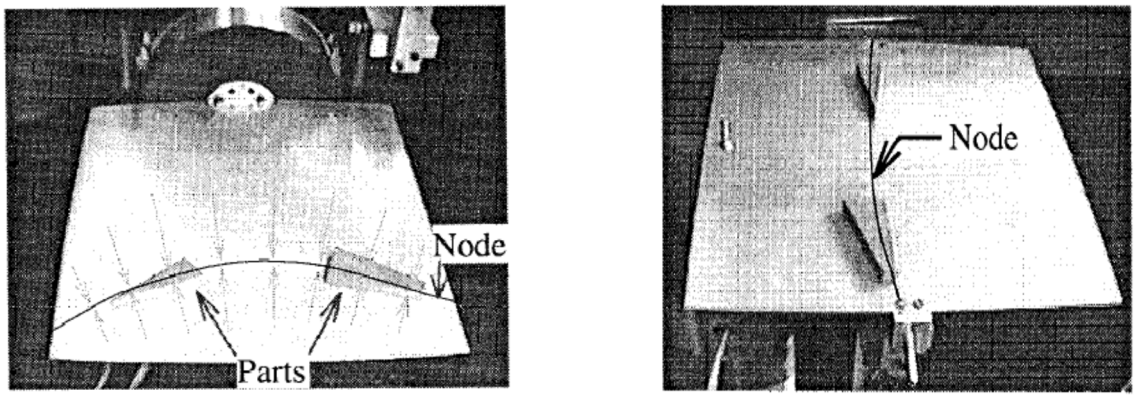

Figure 2.3: Vibrating plate with parts converging due to imposed vibrations, variation of input frequency varies the mode shape and the location of node [10]

Many kinds of sub-millimeter scale actuators were proposed with a variety of motion mechanisms. Used in the form of arrays, two of these kinds are polyimide microcilia thermo-bimorph developed by Suh et al [13] shown in Figure 2.4 and single crystal silicon micro-actuators shown in Figure 2.5. Millimeter order objects were moved with these small scale actuators. Thermo-bimorph actuators were fabricated by sandwiching a metal heater within two layers of polyimide with different expansion coefficient (Figure 2.5(a)). Applying the voltage on the metal heater will increase the temperature of both layers of polyamide and will force them to expand unevenly resulting in changing the shape of the thermo-bimorph cantilever beam. One actuator can provide motion only along one direction

and a set of four actuators will be a single unit to provide motion in all directions along a surface. A workcell comprises of multiple cascades of these units.

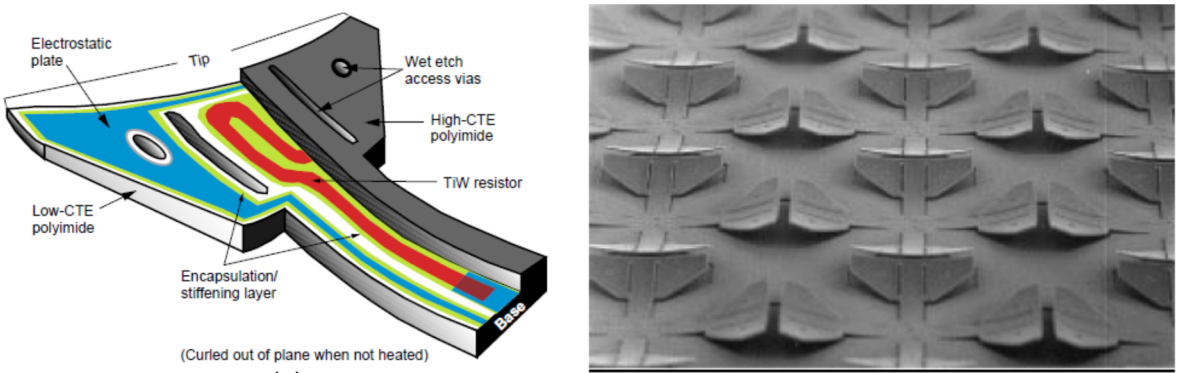

Figure 2.4: Thermobimorph cantilever (a) cross section of a cantilever (b) workcell with cascades of actuator units [11]

Single crystal silicon actuators were fabricated by modified single crystal reactive etching and metallization (SCREAM) process [11]. The application of voltage on the rectangular grid would deflect each actuator. Due to asymmetry in the design as shown in Figure 2.5(c), if activated each actuator generates motion in one specific direction otherwise it acts as a passive frictional contact.

Small movement of a glass object was observed during experimentation and some resonance was observed at certain operating frequencies depending upon the part location with respect to the actuator. Larger travelled distances were not observed and no movement could be achieved with paper on the actuators because of the expected higher roughness of paper surface. The time of movement was not discussed and neither the interaction between parts and base surface. In the process of workpiece convergence, the friction characteristics are expected to follow the Coulomb friction law at macro and millimeter scale.

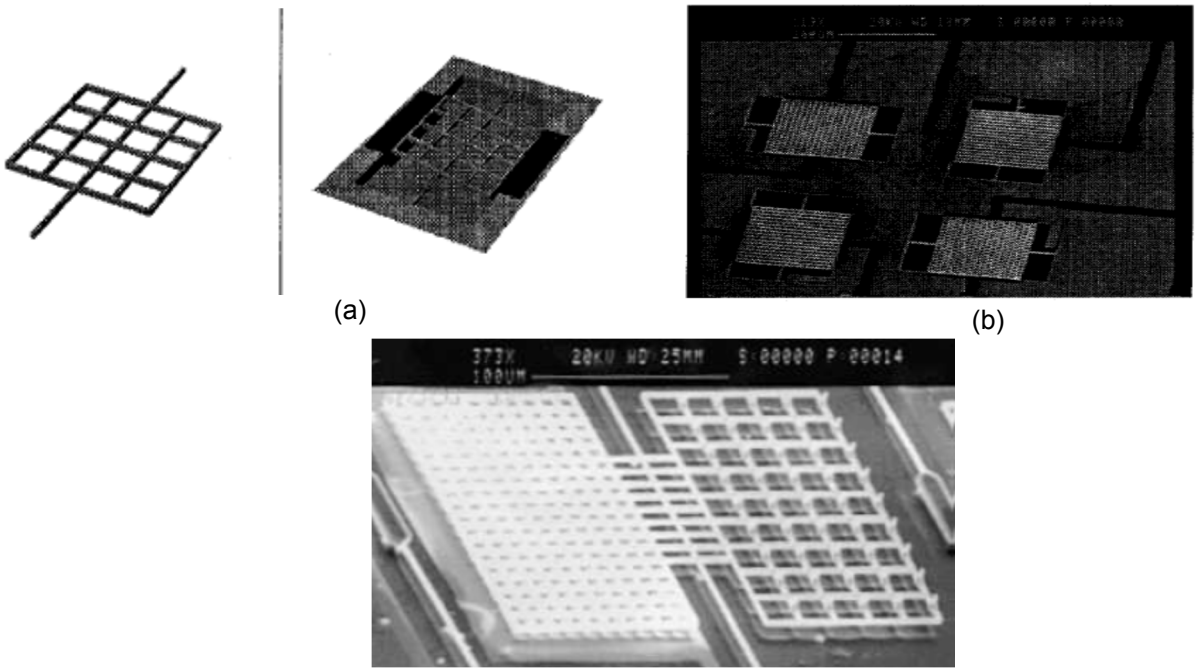

Figure 2.5: (a) Torsional resonator grid with suspending beam (left) resonator and electrode (right) (b)prototype motion pixel [11] (c) asymmetric actuator with left side more dense than right side with aluminum electrode underneath the denser side [9]

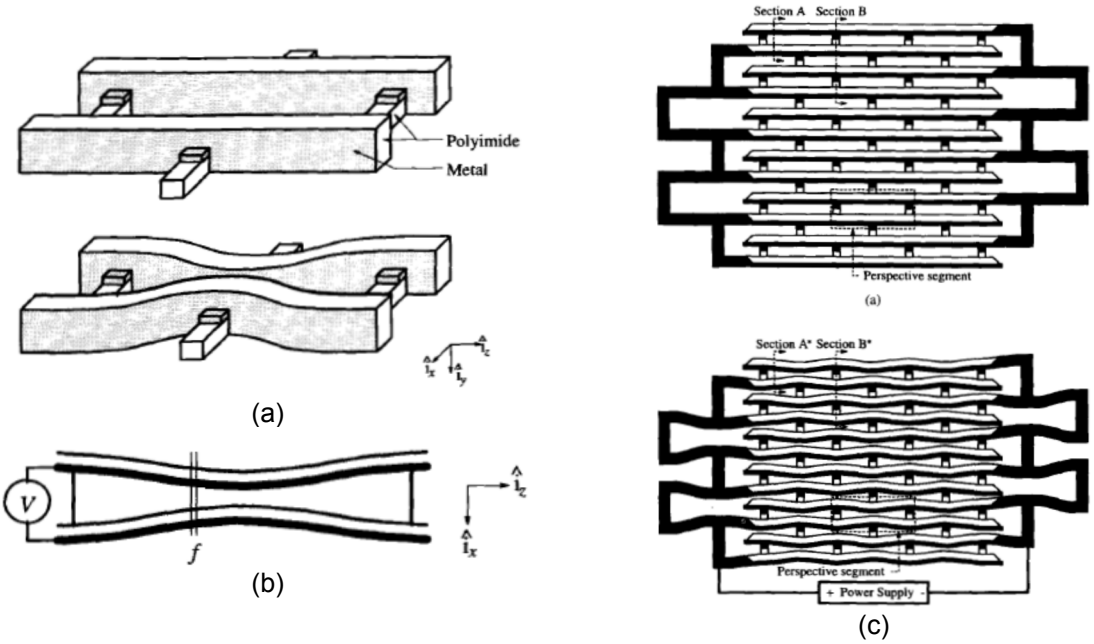

Figure 2.6: Integrated force array [14] (a) representative unit of integrated force array demonstrating partial contraction (b) single unit under electrostatic forces (c) sub-array in unpowered and partially contracted powered configuration

Jacobson et al. introduced integrated force arrays for part manipulation [14]. The schematic of the proposed approach is shown in Figure 2.6. Insulated conductive elastic members were placed parallel to each other with spacers between them. The application of opposite voltage on neighboring members will attract them towards each other, while voltage of same polarity will repel them and increase their spacing. This spacing variation between the elastic struts will move the part resting on the mesh. The amount of deflection is modeled by treating the system equivalent to a capacitor. The elastic energy stored in the workcell per unit length is modeled as a function of the charge stored in the capacitor. The separation between the members is a function of the stored surface energy. To avoid the difficulty of coupling between the electrostatic and elastic forces in the model, finite element analysis is used to model the device.

Hiroyuki et al. proposed the concept of Autonomous Distributed Machines (ADM) [15]. The concept of ADM and its functionality is shown in Figure 2.7. Small scale actuators, each integrated with its own sensor and controller, eliminate the requirement of wiring and compose a servo system which has minimum amount of information exchange. The information exchange between neighboring modules will complete a required task. Two types of microactuation approaches were proposed for part manipulation based on the ADM concept. The mechanism and functionality of both of these approaches are shown in Figure 2.8. One uses thermally driven cantilevers (cilliary motion system (CMS)) and the other uses controlled air flow from micro nozzles to carry flat objects on the workcell. CMS comprises of actuator with two layers of polyimide with different thermal expansion coefficients mounted on a heater. Aluminum is used as sacrificial material. The polyimide used in the upper layer has larger coefficient of thermal expansion. When the current flows in the heater, the temperature rises and the cantilever bends down. The frequency response without any type of artificial cooling is around 10 Hz. The dimension of the cantilever are 500 μm in length and 100 μm in width.

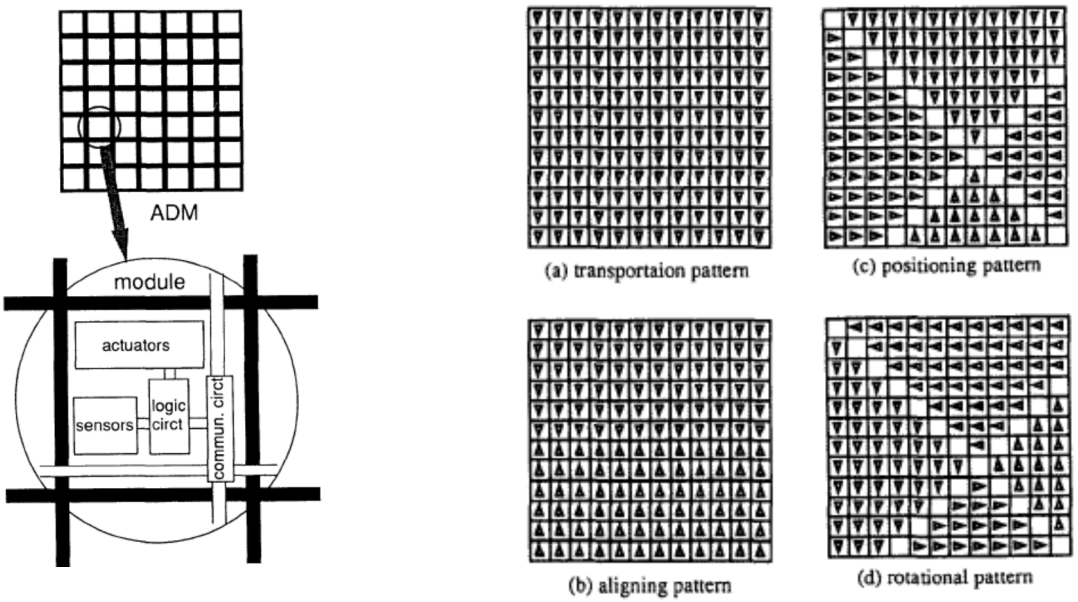

Figure 2.7: A schematic view of autonomous distributed micro-machines (left). Motion pattern of actuators of a planar positioned with many micromodules (right) [15]

The second approach comprises of micronozzles with supply of compressed air. The direction of air coming out of the nozzles can be changed by adjusting the position of the polyimide cover on the nozzle. Not only the part levitates on a layer of compressed air with a reduced friction between the part and workcell surface but the direction of compressed air moves the part as well. A single piece of 1mm x 1mm silicon was moved with this proposed workcell. The applied pressure in the reported experimental setup was 2 kPa. No data has been presented for the minimum size and weight of a micropart to be translated, or for the positional accuracy of the workcell.

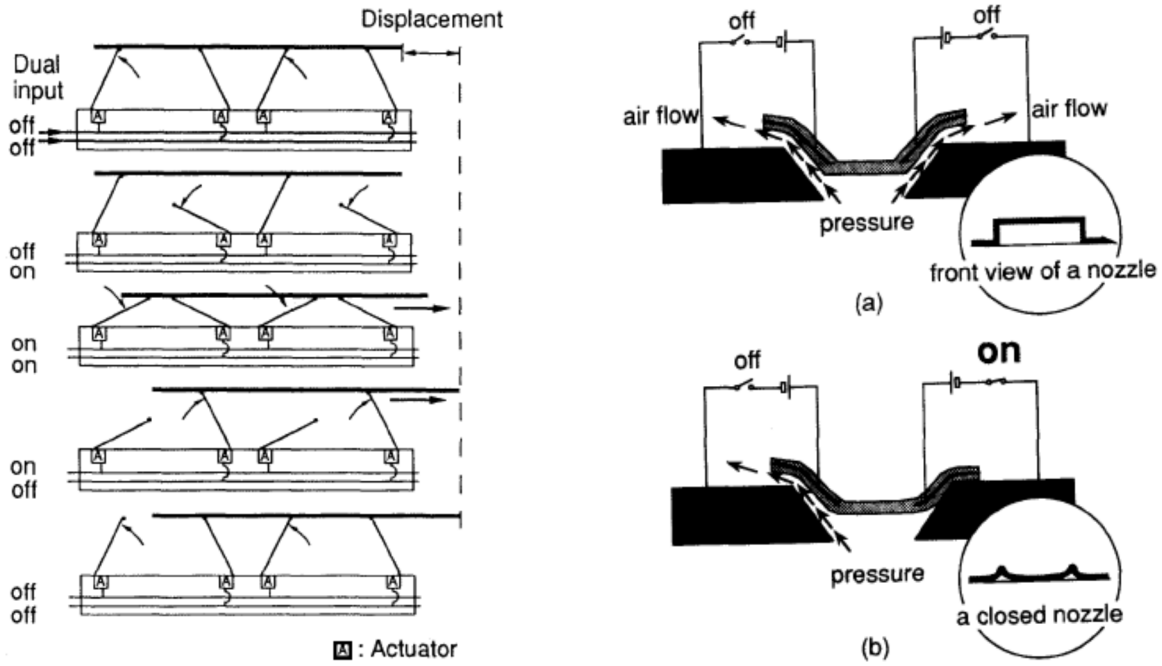

Figure 2.8: (Left) sequence of motion of CMS to translocate a plate (Right) mechanism of motion of an actuator (a) initial configuration of nozzle with compressed air (b) powered configuration with directional flow of air [15]

Pister et al. proposed a platform with air nozzles on the base along with electrodes for actuation as shown in Figure 2.9 [16]. The cushion of compressed air will help levitate the platform, reduces the friction between the object and platform to negligibly low values. Parallel electrodes are attached to the base which applies an electrostatic force on the platform to move it in the required direction. The component of electrostatic force parallel to the base surface moves the platform while the component perpendicular to the surface reduces the gap between the platform and base. Reduction of the thickness of air bearing between the platform and the base will increase the parallel (driving) component of force to several orders of magnitude and can increase the possible acceleration of the platform to about 1g. This model requires better mathematical modeling of the air bearing and better instrumentation and measuring techniques

Furuhata et al. proposed the design of ultrasonic micro actuators [17]. The actuators consisted of vertical pin like structures with transducers at the base. The hardware and functionality of the actuator is

explained in Figure 2.10. The to-and-fro motion of the pins generated the resultant motion of an object placed on them. The transducers at the base can be of two types; piezoelectric or electrostatic.

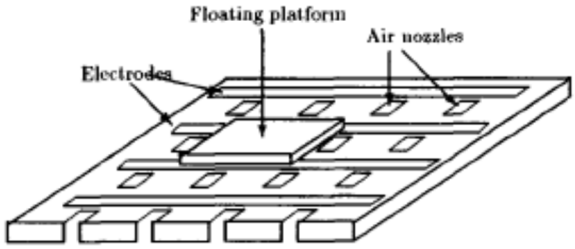

Figure 2.9: Schematic of a platform with electrodes and nozzles to generate the air bearing below a floating platform [16]

Piezoelectric type modules consist of 200μm think layer of PZT on both sides with the module cross-section shown in the Figure 2.10(a). Electrostatic force type modules are the second type of proposed actuation mechanism. The electrostatic force between the electrodes reduces the gap and tilts the actuator on one side. Sub-micron order of displacement can be achieved with the proposed mechanism with an applied voltage of 30*V*. The authors reported testing only fundamental operation of piezo-electric type micro-actuators while no other data has been presented.

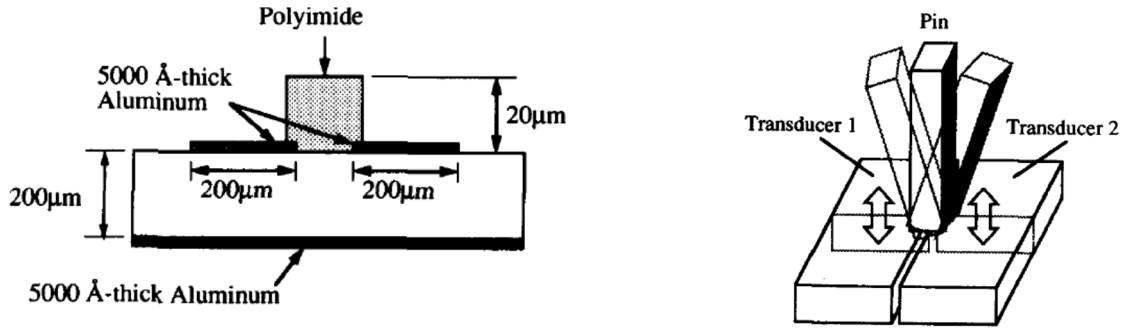

(a) (b)

Figure 2.10: (a) Cross-section of microactuator, transducers are at base on both side of actuator (b) movement of actuator as a result of the voltage applied to transducer [17]

Turitto et al. proposed a microfeeding device based on the principle of distributed manipulation [18]. The microfeeder consists of an array of micro-nozzles. Air is used to keep the parts suspended on the base platform. The direction of air is controlled to move the parts in the required direction. The squared cross-sectioned nozzles, shown in Figure 2.11(a), are opened or closed by electrostatic

actuation. In the neutral position the control pin is at the center and air coming out of the nozzles is distributed equally in all directions and the object hovers above the platform without any lateral force. To move the object in a required direction, the central cursor is attracted towards one of the walls and the corresponding air flow path is closed as shown in Figure 2.11(b). The unequal flow of air in all directions moves the objects in the required direction.

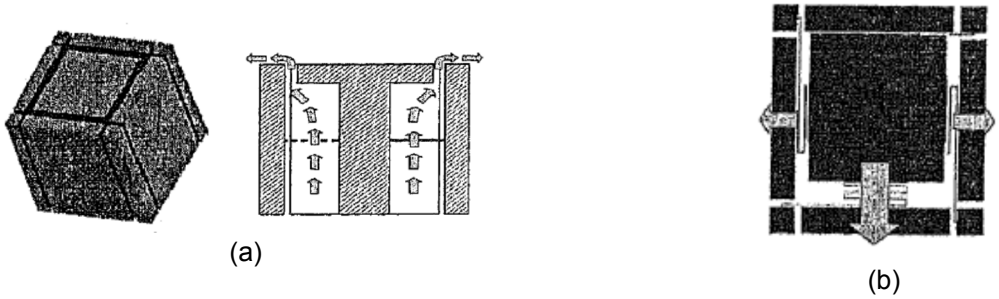

(a) (b)

Figure 2.11: (a) Air nozzles with the sectional view (b) asymmetric air distribution due to eccentric central pin [18]

The approaches discussed consist of discrete actuators controlled by a central unit for coordinated operation to complete a task. The discreteness of actuation puts a lower limit on the size of the part to be handled; parts with size smaller than the spacing between the actuators will get stuck between the actuators and could not be handled. The discreteness in actuation may impair the accuracy of part placement through direct actuation; for smaller sized parts, the relative position of actuators and parts can alter the placement accuracy across the workcell. A technique which can relax the constraint on the lower bound on the size of workpiece and associated with a mathematical model to predict the micropart motion is still missing in the field of MEMS handling.

In addition, the existing methods for micropart manipulation and location only describe the mechanism for part movement, but they do not discuss the interaction of the micropart with the surface nor the role of surface forces on system dynamics. With the micropart size getting smaller, the weight and inertia force start becoming negligible compared to the surface forces of attraction of Van der Waal's, Casimir, capillary, and electrostatic [19, 20]. Thus, to accurately model the system dynamics, this shift of dominance from the body forces to surface forces must be considered in dynamic models and workcell design. The surface forces depend upon the materials in contact and roughness of the surfaces in

contact. Surface roughness is one of the most important parameters in precise MEMS manipulation and has been repeatedly asserted in the open literature [21, 22]. The effects of these parameters on the system dynamics should be quantified and accommodated in the model of any proposed micropart translocation approach.

2.3 Summary

A comprehensive survey of the existing micromanipulation methodologies has been presented. These approaches incorporate discrete actuators to manipulate the micropart. The spacing of the actuators defines a lower bound on the size of micropart to be handled. Also, discretely located actuators could have limitations on the accurate positioning of the micropart through direct manipulation. Considering the limitations of the existing manipulation approaches, there is still room for more promising techniques which could address some of the constraints of existing micromanipulation systems.

CHAPTER 3

PROPOSED APPROACH, MATHEMATICAL MODEL DEVELOPMENT, FEASIBILITY ANALYSIS AND PROCESS SENSITIVITY

3.1 Introduction

The literature review in chapter 2.0 concludes that the available approaches for micromanipulation are mainly suitable for parts with millimeter and sub-millimeter size order. However, these approaches due to their discrete actuation principles cannot be used for parts in the range of microns. In addition to size, part weight at the micro scale becomes a negligible quantity. The surface area to volume ratio increases as the part size gets smaller and smaller resulting into small weight compared to the surface forces which become dominant at micron scale [19, 20]. Accurate modeling of motion dynamics of microparts requires one to consider the surface forces and include them in the model. Most of the micromanipulation approaches in the literature lack this interaction of the micropart with the workcell surface though some of them model the functionality of the workcell itself.

Keeping in view the requirements for MEMS assembly and in addressing the deficiency in the current micromanipulation approaches, this chapter introduces a new method for micron size part translocation manipulation based upon the concept of active surface. The proposed approach comprises of a continuous flexible surface carrying microparts resting on it. The controlled deformation of the flexible surface results in the controlled motion of the micropart.

This chapter begins with the explanation of the new proposed approach for micropart manipulation. The dynamic motion model and the techniques employed to solve the problem are discussed. A brief literature review of the dominant forces at microscale is presented. Contact mechanics along with surface roughness models will be explained to lay the basis of the mathematical model of the system. The equations of motion would be introduced with the estimation of dominant surface forces and inertia input from a single actuator. Subsequently, the feasibility of the proposed approach for controlled

micropart motion is established. The results indicating that controlled motion through the controlled deformation (compression) of a flexible substrate is feasible will be presented with the discussion on the characteristics of micropart motion on the flexible surface. Subsequently, the solution methodology will be introduced along with the effects of the dynamics on the micro-forces and more specifically the deformation of the surface asperities that in turn influences the attraction and friction forces. The development of a numerical approach and the logical sequence of events in developing a simulation environment to predict the micropart motion will be explained. The simulation results and the trends in the output are presented with detailed discussion of micropart motion pattern due to single actuator input.

Once the feasibility is established, the system output is analyzed to understand the effects of input variables. Some of these variables are system control parameters while others are function of workcell material and surface finish. The relative influence of these parameters on the displacement of the micropart is analyzed in a sensitivity analysis. This chapter ends with the conclusions based on the results from the numerical simulations and comments about the sensitivity of system output relative to the input parameters.

3.2 Proposed Approach for Micromanipulation

The proposed approach comprises of a micropart resting on a flexible surface as shown in Figure 3.1(a). The surface is deformed in a controlled fashion using an attached actuator such as a piezo-actuator beneath the surface as shown in Figure 3.1(b). The high acceleration imposed by the piezo-actuator results in a high inertia force imparted to the micropart. The components of inertia force tangential and orthogonal to the deformed surface cause the motion of the micropart as it will be explained later.

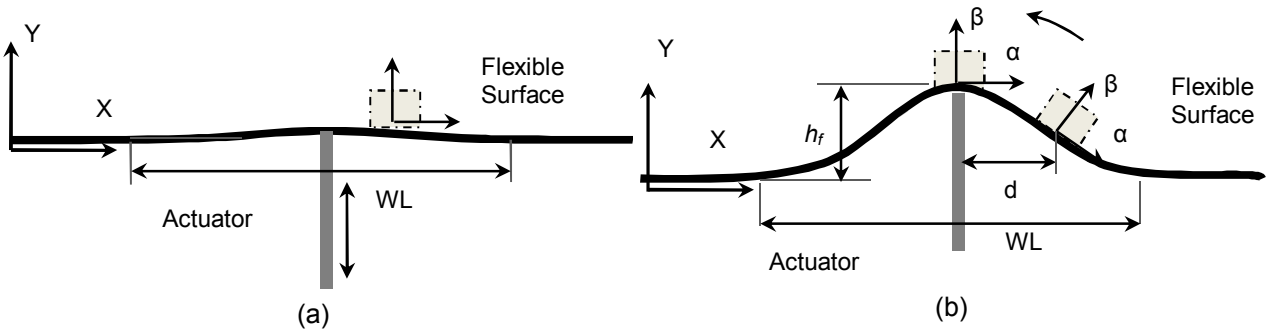

Figure 3.1: Actuator deformation parameters (a) micropart resting on a flat surface (b) surface with controlled deformation

The surface deformation and actuator parameters as shown in Figure 3.1(b) are the wavelength of deformation *WL* and the actuator stroke length h_f. The micropart location relative to the actuator location is shown as *d*. A microconveyor could be realized by a longer surface with an increased number of attached actuators placed in an array as shown in Figure 3.2. The controlled actuation of actuators would cause the micropart to translocate along the surface beyond the capability of a single actuator.

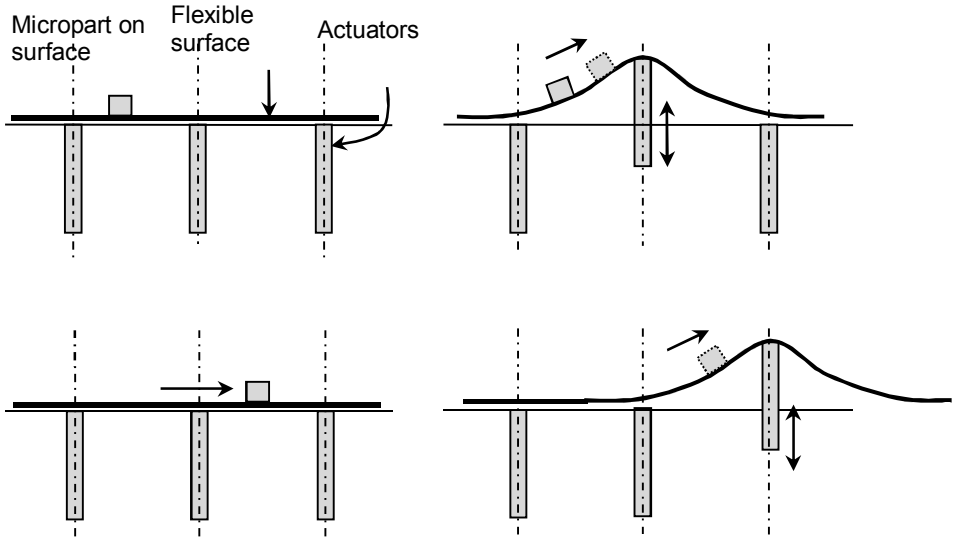

Figure 3.2: Microconveyor realization, the sequential actuator firing and the resultant micropart motion (a) all three actuator in retracted position (b) 2nd actuator moves forward imparting huge inertial force to the micropart. (c) 2nd actuator finishes its reverse stroke and the part starts moving (d) 3rd actuator is fired up to keep the forward push on the part

The frequency and velocity profile of actuator motion are the parameters for each individual actuator while the wavelength of deformation is governed by the actuator . These parameters in addition to material and surface properties are used to develop the system dynamic model explained in the next section

3.3 Dynamic System Model

In this section, the details of the mathematical model of the system are discussed. The system of equations governing the motion of the micropart is developed considering the dominant forces at the microscale. Important parameters of the system are discussed, estimated and included in the system mathematical model.

At the microscale, the coefficient of friction (COF) is not constant, but similar to meso and macro scale the friction force is a function of the normal applied force. Thus, in an accurate dynamic model valid at the microscale, the coefficient of friction must be dynamically evaluated during the motion of the micropart considering the dynamic effects of the micro-forces. In the open literature, various friction models exist; these models as they apply to the present research will be revisited and discussed. In this research, the Kogut-Etsion (KE) friction model, which allows for the evaluation of the static COF, is used and extended through a numerical simulation approach to continuously identify the dynamically changing COF while considering the effects of the micro-forces. In addition to the evaluation of the COF, an accurate evaluation of system dynamics at micro-scale requires the evaluation of surface forces.

3.4 Forces at Microscale

The motion analysis of macro- and meso-scale components requires one to consider body forces and applied loads; however, the analysis for microscale parts requires additional considerations. Surface forces become prominent once the part size becomes small and its weight becomes negligible [19, 20]. Modeling the motion dynamics of microparts requires one to consider this shift of dominance from body to surface forces, thus a brief discussion of the various surface forces is presented.

3.4.1 *Casimir Force*

The Casimir force is a special kind of temporary dipole-dipole attraction force. When two atoms are apart at an appreciable distance, the time taken for the electric field of the first atom to reach the second and return can become comparable with the period of fluctuation of the dipole itself [23]. When this happens, the field returns to find that the direction of the instantaneous dipole of the first atom is now different from the original one and less favorably disposed to an attractive interaction. So, with increasing the interaction distance *r* between the two atoms, the dispersion interaction energy begins to decay faster than $-1/r^6$ and approaches $-1/r^7$. This dispersion force due to this retardation effect is known as Casimir force or Retarded Van der Waal's force. Mathematically, the Casimir force per unit area between two uncharged metallic plates in vacuum separated by a distance *l* is given by [20]

$$F_{(l)} = \frac{-\pi^2 \eta c}{240 l^4} \tag{3.1}$$

where *c* is the speed of light, η is the reduced Planck's constant, $c = 3 \times 10^8$ m/sec and $\eta = 6.5211 \times 10^{-16}$ eVs. This force is between the two surfaces when the distance between them is appreciably larger. The formulation of Casimir force can be extended for a rough surface as will be done for Van der Waal's force but for the current analysis, being a force which is significant at a distance, it is neglected.

3.4.2 *Capillary force*

This is the force between two surfaces in contact due to the capillary action which is the result of surface tension generated by the fact that a molecule on the surface of a liquid has higher energy compared to a molecule inside the liquid. The capillary force is present if there is at least condensation in humid environment. The capillary force is a function of the material, medium of contact and surface roughness [24]. Using surface tension of the fluid at the contact point and the resultant angle of contact, for simple smooth surfaces, at a given distance *l*, this force can be calculated by [20]

$$F_{(l)} = \frac{-2\gamma\left(\cos(\theta_1)+\cos(\theta_2)\right)}{l} \qquad 3.2$$

where the angles θ_1 and θ_2 are shown in Figure 3.3 and γ is the surface tension of the liquid. The capillary force depends on the angle of mediating liquid between the two solids which is a function of the surface energy of the liquid and the solids in contact. This formulation for smooth surfaces can be extended to rough surfaces. Among all micro-scale forces, the capillary force plays a dominant role if the relative humidity is high. In most of the practical situations, capillary condensation of water may begin in MEMS structures at a relative humidity of about 65% [20]. For situations where the relative humidity is low, as is the case of MEMS assembly which is mostly performed in controlled environment, this force can be neglected. Therefore, this force is neglected in this research.

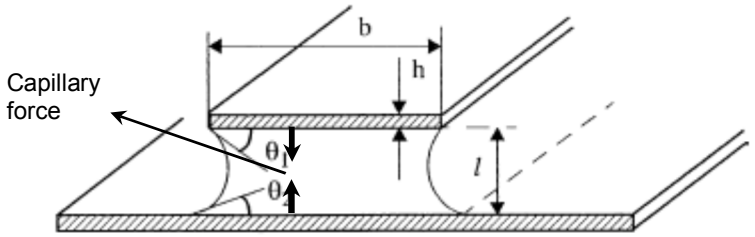

Figure 3.3: Two solid plates with liquid in between. The magnitude of capillary force depends upon the angles of meniscus [20]

3.4.3 *Electrostatic force*

The electrostatic force is caused by the attraction between isolated bodies having electric charge on one of them or carrying opposite charge. The magnitude of this force depends on the magnitude of charge and the distance between the bodies. This force exists between the bodies even if the materials are initially at a neutral state before contacting each other, In addition to the particles carrying permanent electrostatic charges, this force is observed between materials being initially neutral before contact. Contact electrification charges the two dissimilar materials in contact and results in the electrostatic force between the surfaces. The magnitude of the charges depends upon the materials in contact and real contact area and is a weak function of duration of contact [25]. For rough surfaces, the real area in

contact is different from the apparent contact area and depends upon the surface roughness profile and materials in contact[26].

An electrostatic force can be used to actuate MEMS structures in applications such as switches, tunable capacitors, electrostatic motors etc. This force of attraction can be neglected if one of the surfaces is grounded which is usually the case in controlled environments for MEMS assembly. Therefore, the electrostatic force, though can be easily accommodated (except its time dependencies) in the proposed mathematical model, will be neglected in this research.

3.4.4 *Van der Waal's force*

The Van der Waal's force, a force between the molecules of a material, is a subcategory of the forces due to dipole-dipole interaction. For Van der Waal's forces, these dipoles are not permanent in nature but are induced and transitory in nature. The electrons in an atom or molecule are always in motion even when in their ground state. Though on the average the dipole moment of a spherically symmetric atom or molecule is zero, at any instant, a temporary dipole moment can occur [20, 23]. For example, for a non-polar atom such as helium, the time average of its dipole moment is zero, yet at any instant there exists a finite dipole moment given by the instantaneous positions of the electrons about the nuclear protons. This dipole generates an electric field that polarizes nearby neutral atoms and creates a dipole moment in them. The interaction produces an instantaneous attraction force and the time average of this force is finite. The magnitude of these forces given by London is [20]

$$F_{(r)} = \frac{9\alpha_{o1}\alpha_{o2}h\nu_1\nu_2}{(\nu_1+\nu_2)(4\pi\varepsilon_o)^2 r^6} \qquad 3.3$$

where ν_i represent the orbiting frequencies of electrons in atom i, α_{oi} is electron polarizability of atom *i*, *h* is Planck's constant, *r* is the distance between the atoms and ε_o is the permittivity of vacuum. This force of attraction between the neutral atoms gives rise to a force of attraction between two surfaces which are a small distance apart, *l*. The force between a sphere (radius *R*) with half space and the force between a flat surface (area *A*) and half space flat surface are respectively given by [20]

$$F = \frac{-AR}{3l^4} \qquad (\text{sphere}) \tag{3.4}$$

$$F = \frac{-A}{6\pi l^3} \qquad (flat) \tag{3.5}$$

This formulation is applicable for perfectly flat surfaces whereas, in reality, any real surface comprises of various levels of unevenness. The Van der Waals force, being a strong function of the distance between the surfaces, depends heavily on the surface roughness of both the surfaces in contact.

3.5 Microscale forces for rough surfaces

The above mentioned forces could be estimated if the surfaces are perfectly smooth without any unevenness. For simple planar surfaces, these forces are functions of distance between the surfaces, material properties of the surfaces in contact, and the medium of contact. Estimating these forces becomes cumbersome for rough surface when these formulae cannot be simply used. In addition, the effective distance between the surfaces is a function of the surface roughness, thus making surface roughness one of the important parameters that contribute to the magnitude of the surface forces. The challenge is not only to represent the surface with a quantitative measure but to define it in such a way that this measure can be used to calculate the amount of attraction and repulsion forces between the two surfaces.

Contrary to planar surfaces, rough surfaces consist of asperities. When rough surfaces are in contact, these asperities are compressed generating a repulsion force between the surfaces. There had been attempts to measure the exact profile of the surfaces in contact, and use these profiles to estimate the repulsion force due to compression of asperities and attraction force between these surfaces, while the second approach is to mathematically model the surface roughness and relate it to the surface forces [26]. There are many measures to represent the surface roughness such as standard deviation, mean surface roughness, range, frequency spectrum and kurtosis, but most of these measures to estimate

surface roughness cannot be easily extended to develop an analytical model of microforces between rough surfaces in contact [27].

3.6 Contact models

One way to address surface roughness is a statistical representation of the rough surface that the basic theories of contact mechanics could be used, and the formulation of attraction and repulsion forces by a single asperity can be extended to calculate the surface forces by the whole rough surfaces. A brief review of the contact \models used in this statistical process are discussed.

3.6.1 *Hertzian contacts*

The first single point contact model was presented by Hertz in 1886. It used the elastic modulus of the material and shapes in contact with each other. The Hertz formulation assumes pure elastic contacts without any adhesion force between the two surfaces in contact. The results were the analytical solution for pre-defined shapes such as sphere-flat, sphere-sphere, cylinder-cylinder, etc., in contact with each other. The results of these solutions estimate the deformed shape of contact point and stress pattern at and in the vicinity of the contact point [28, 29]. Some of the results of the Hertz analytical solution for some predefined shapes in contact are [29]

$$F = \frac{4E_e R^{\frac{1}{2}} d^{\frac{3}{2}}}{3} \qquad (sphere - flat) \tag{3.6}$$

$$F = \frac{2}{3}\pi a^2 p_o \qquad (sphere - sphere) \tag{3.7}$$

$$\frac{1}{E_e} = \frac{1-\nu_1^{\,2}}{E_1} + \frac{1-\nu_2^{\,2}}{E_2} \tag{3.8}$$

where d is the depth of deformation, R is the radius of sphere (for sphere-sphere contact both sphere have same radius) E_e is the equivalent elastic modulus, and ν_i is the material Poisson's ratio. F is

the contact load, a is the radius of the contact spot and p_o is the maximum contact pressure for sphere-sphere contact.

3.6.2 *Johnson-Kendall-Roberts (JKR) contacts*

This model was primarily proposed for a sphere in contact with a flat surface [30]. The surface attraction force was modeled as the distance derivative of the net energy between the two surfaces in contact. The system energy decreases when the two surfaces come in contact and the surface energy of the two independent surfaces is replaced by the energy of the two surfaces in contact. On the other hand, the energy of the system increases by the storage of energy due to elastic deformation. The net system energy is the difference between the decrease due to surfaces in contact and increase due to elastic storage. The equilibrium point is the point when these two balance each other [30]. The attraction force is the resultant of the derivative of this net energy with respect to distance. This model accommodates the adhesive force of attraction between the two surfaces. The maximum pull force required to separate the two surfaces, *F*, is given by

$$F = -\frac{3}{2}\Delta\Upsilon\pi R \tag{3.9}$$

$$\Delta\Upsilon = \Upsilon_1 + \Upsilon_2 - \Upsilon_{12} \tag{3.10}$$

where $\Delta\Upsilon$ is the difference of surface energy of the two surfaces and the energy while the two surfaces are in contact. Υ_i is the surface energy of surface *i* and *R* is the radius of sphere. The JKR model assumes the effect of adhesion between the two surfaces only inside the area of contact. This model is good mathematical representation of hard-soft contacts.

3.6.3 *Derjaguin-Muller-Toporov (DMT) model*

This is an adhesive contact model estimating the contact area and adhesion and repulsion forces between a sphere in contact with a flat surface. While the JKR model assumes that the asperity shape is deformed, the DMT model is based on the assumption that the cross section of asperity remains the

same as the Hertz contacts while the attraction force is outside the contact region [31]. The pull-off force between a sphere in contact with a flat surface, F, is given by

$$F = -2\Delta\Upsilon\pi R \tag{3.11}$$

where $\Delta\Upsilon$ is the energy released during contact as explained in 3.2.2 and R is the radius of the sphere. The DMT model is good for analyzing hard-hard surfaces in contact. Papers including discussions on the validity of JKR or DMT models emphasize the above proposition and verify the validity of both models in the regimes of hard to soft and hard to hard and the transition in between [32, 33].

3.7 Surface roughness models

The contact models introduced are single point contact models. A rough surface usually consists of multiple asperities of random shape. This randomly uneven surface can be represented by an equivalent surface which is covered with asperities of predefined shape. These asperities have a defined value of asperity density and tip radius and are arranged with a probability distribution function (PDF) along the normal to the surface. This PDF for the spread of the asperities along the normal to the surface is a variable which depends upon the manufacturing process the surface has been produced by [26]. A schematic of the equivalent surface is shown in Figure 3.4 where h_s represents the difference between mean of asperities height and mean of surface height. The *z*-axis represents the direction normal to surface along which the asperities are arranged with a defined PDF. The normal distribution of asperities is shown on the left of Figure 3.4.

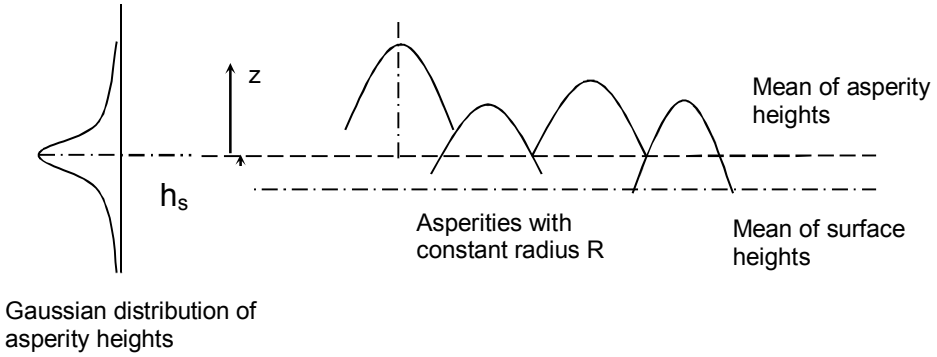

Figure 3.4: The surface equivalent to the flat surface. Equivalent surface is covered with asperities

With the assumption of an equivalent surface, the single point contact theories along with additional formulations to estimate the force of attraction at the non-contacting areas are exploited to estimate microforces between the two surfaces. Using these single point contact theories, and the concept of equivalent surface, contact models for rough surfaces were developed and are reviewed in the following subsections.

3.7.1 *Greenwood Williamson Model (GW model)*

Greenwood and Williamson, for the first time, proposed a model for rough surface based upon the concept of equivalent surface. They proposed that a rough surface with random surface roughness profile can be assumed to be a planar surface covered with spherical asperities of uniform radius. The heights of these asperities have a statistical distribution and while in contact, will deform elastically [26].

In addition, it was proved that a pair of two surfaces covered with a predefined shape of asperities can be expressed or converted into an equivalent pair of a surface covered with asperities in contact with a flat non-deformable surface [34]. The shape of asperities on the single equivalent surface of “equivalent rough-flat” surface pair depends on the shape of asperities on both the individual “rough-rough” surface pair [34]. A simplified approach to estimate the statistics of a rough-flat pair from a given rough-rough pair in contact, is to estimate the radii of asperities of a single equivalent surface equal to the sum of the individual rough surface asperities radii and spread of the asperities on the single equivalent surface as

the sum of the distribution on the individual surfaces. With this simple process, the results of true contact area and repulsion force vary from their original values by less than 5 percent [34].

The total number of asperities in contact, real contact area and the resultant repulsion force, *P*, generated by the compression of asperities is given by equations (3.12-3.14) [26]

$$n = N\int_d^\infty \phi_z dz \tag{3.12}$$

$$A = \pi N\beta\int_d^\infty (z-d)\phi_z dz \tag{3.13}$$

$$P = \frac{4}{3}NE'\beta^{0.5}\int_d^\infty (z-d)^{\frac{3}{2}}\phi_z dz \tag{3.14}$$

where $\beta = \eta R\sigma$, *E'* is the equivalent material modulus, n represents asperities in contact, A is the nominal area of contacting surfaces, *N* are the total number of in contact asperities, η is the asperity density ϕ_z is the probability distribution function of asperity spread. The σ is the standard deviation of the asperity spread and the mean distance between the two surfaces is represented by *d*.

The GW contact model is based on Hertz contact theory. Hertz's model is a pure elastic model and does not accommodate any force of attraction between the surfaces. Therefore, it only calculates the real contact area and repulsion force between the rough surfaces to be balanced by the external applied load. In addition, the limit of elasticity as defined by the work of Tabor [35] is given by

$$\omega_p = \beta\left(\frac{H}{E'}\right)^2 \tag{3.15}$$

where *H* is the material hardness and ω_p is the start of plastic deformation. The GW model, represented by equations (3.12-3.14), uses material and surface properties and mean distance between the mean of rough surface and flat surface and estimates the real contact area and repulsion force.

3.7.2 *Rough surface using JKR model (Fuller and Tabor work)*

Fuller and Tabor conducted the experiments to estimate the force of attraction between rubber ball and perspex surface roughened at various degrees [36]. They compared the results of the experiments with the theoretical value estimated using the JKR contact model along with the equivalent surface assumption by GW. The comparison of the results showed that the JKR theory predicts the experimental results reasonably well.

3.7.3 *Chang-Etsion-Bogy Model (CEB model)*

Chang, Etsion and Bogy modified the GW model to estimate the real contact area and force of attraction, and extended it to calculate the friction force between two rough surfaces in contact [37-39]. The GW contact model for rough surfaces was modified on the basis of JKR and DMT contact theories to estimate the attraction force. The transition between the hard-soft contacts to hard-hard contacts was used to produce a universal model for any kind of surfaces in contact. For contacting asperities the JKR-DMT transition was used where for the non-contacting areas the Lennard-Jones potential was used as the estimation of the force of attraction. The shape of asperities under plastic deformation was calculated using the principle of conservation of volume [37].

Similar to the GW model, the input to the CEB model is the mean distance between two rough surfaces and the output is the real area of contact, force of repulsion due to asperities compression and the force of attraction between the two surfaces which are given by the equations (3.19) and (3.20). The total contact area, asperity load and force of attraction estimated by the CEB model are presented in equations (3.16) through (3.21) [37, 38]

$$A_{t(d)} = A_{e(d)} + A_{p(d)} \tag{3.16}$$

$$A_{e(d)} = \eta A_n \pi R \int_d^{d+\omega_c} (z-d)\phi_z dz \tag{3.17}$$

$$A_{p(d)} = \eta A_n \pi R \int_{d+\omega_c}^{\infty} \left[2(z-d)-\omega_c\right]\phi_z dz \tag{3.18}$$

$$P_{(d)} = \eta A_n E \left\{ \frac{4}{3} R^{\frac{1}{2}} \int_d^{d+\omega_c} (z-d)^{\frac{3}{2}} \phi_z dz + \pi RK \frac{H}{E} \int_{d+\omega_c}^{\infty} \left[2(z-d) - \omega_c \right] \phi_z dz \right\} \quad 3.19$$

$$F_{s(d)} = \frac{8\pi}{3} \eta A_n R \Delta\gamma \left\{ \begin{array}{l} \int_{-\infty}^{d} \left[\left(\frac{\varepsilon}{\varepsilon - \omega} \right)^2 - 0.25 \left(\frac{\varepsilon}{\varepsilon - \omega} \right)^8 \right] \phi_u du + \\ \int_d^{\infty} \int_0^{\infty} \frac{2}{R\varepsilon} \left[\left(\frac{\varepsilon}{Z(\omega, s)} \right)^3 - \left(\frac{\varepsilon}{Z(\omega, s)} \right)^9 \right] \phi_u s ds du \end{array} \right\} \quad 3.20$$

where

$$Z_{(r,a)} = \frac{1}{\pi R} \left[a \left(r^2 - a^2 \right)^{\frac{1}{2}} - \left(2a^2 - r^2 \right) \tan^{-1} \left(\frac{r^2}{a^2} - 1 \right)^{\frac{1}{2}} \right] + \varepsilon \quad 3.21$$

The CEB adhesion and contact model was further extended by the same authors to calculate the force of static friction between the rough surfaces. The force of friction was estimated on the assumption that only asperities in elastic contact can support the shear load. Using the contact area of those asperities and using Hamilton stress field for combined normal and tangential loading along with Von Mises failure criterion the tangential load supported by the asperities is estimated. This tangential load supported by the asperities is the force of friction between rough surface and is given by equation (3.22) [39]

$$Q_d = \eta A_n \int_d^{d+\omega c} \frac{4}{3} E R^{\frac{1}{2}} (u-d) \frac{3}{2} f \left(\frac{u-d}{w_c}, \nu \right) \phi_u du \quad 3.22$$

where *f* is a function that depends on the failure inception location.

3.7.4 *Zhao Modification*

Though the CEB model was proposed with the intention to have a generalized model for the entire range of loading, it was criticized due to many shortcomings. In the CEB model, the average

contact pressure was allowed to jump from *2/3KH* in the elastic region to *KH* in the plastic zone where H is the hardness of the material and K is the factor for maximum contact pressure [40]. Though the CEB model was based upon the elastic, pure plastic deformation and a long range of elastic-plastic deformation as suggested by Johnson [41] was totally neglected. In addition, the CEB model (elastic-plastic model) estimates the real area of contact to be smaller and the mean separation distance larger than those obtained for pure elastic contact at the same contact load and plasticity index which are contradictory to the experimental results presented by Powierza [42]. Zhao proposed modifications to the CEB model with the main focus to model the long transitional regime from elastic to fully plastic flow [40]. The contact area, and asperity load given by the Zhao model are [40]

$$A_{t(d)} = A_{et(d)} + A_{pt(d)} + A_{ept(d)} = N\int_{d}^{d+\omega 1} A_{et}\phi_z dz + N\int_{d+\omega 1}^{d+\omega 2} A_{ept}\phi_z dz + N\int_{d+\omega 2}^{\infty} A_{pt}\phi_z dz$$
$$= \eta A_n \pi R\int_{d}^{d+\omega 1} \omega\phi_z dz + \eta A_n \pi R\int_{d+\omega 1}^{d+\omega 2} \omega\left[1-2\left(\frac{\omega-\omega 1}{\omega 2-\omega 1}\right)^3+3\left(\frac{\omega-\omega 1}{\omega 2-\omega 1}\right)^2\right]\phi_z dz +$$
$$2\eta A_n \pi R\int_{d+\omega 2}^{\infty} \omega\phi_z dz \qquad 3.23$$

$$W_{t(d)} = \frac{4}{3}\eta A_n E R^{0.5}\int_{d}^{d+\omega 1} \omega^{\frac{2}{3}}\phi_z dz + 2\pi\eta A_n HR\int_{d}^{d+\omega 1} \omega^{\frac{2}{3}}\phi_z dz +$$
$$\eta A_n \pi R\int_{d+\omega 1}^{d+\omega 2}\left[H - H(1-K)\left(\frac{\ln(\omega_2)-\ln(\omega)}{\ln(\omega_2)-\ln(\omega_1)}\right)\right]\times\left[1-2\left(\frac{\omega-\omega 1}{\omega 2-\omega 1}\right)^3+3\left(\frac{\omega-\omega 1}{\omega 2-\omega 1}\right)^2\right]\omega\phi_z dz \qquad 3.24$$

where ω_1 and ω_2 are the limits for end of elastic range and the elastic-plastic range respectively. E is the equivalent modulus of the material and R represents the radius of the asperities.

3.7.5 *Kogut-Etsion Model (KE Model)*

The discontinuity of the average pressure between the elastic and plastic regions in the CEB model was mathematically smoothened in the Zhao model [40]. Kucharski tried to solve the contact problem of a deformed sphere by the finite element method and developed empirical expressions for the

contact load and contact area [43]. The mean pressure in CEB model was in some cases higher than the indentation hardness and therefore unreasonable.

In an effort to produce an accurate general solution for the elastic-plastic contact of a deformable sphere against a rigid flat, Kogut and Etsion modified the CEB model equations on the basis of finite element analysis results. Given the mean distance between the two surfaces, the KE model estimates the attraction force between the surfaces, the repulsion force due to compression of asperities and the value of static force of friction between them. The detailed equations of KE model are [44-47]

$$P = \eta A_n \int_d^{\infty} \bar{P}(z-d)\varphi_{(z)} dz \tag{3.25}$$

$$F_s = \eta A_n \int_{-\infty}^{\infty} \bar{F}_s(z-d)\varphi_{(z)} dz \tag{3.26}$$

$$Q_{\max} = \eta A_n \int_{-\infty}^{d+6\omega_c} \bar{Q}_{\max}(z-d)\varphi_{(z)} dz \tag{3.27}$$

$$\psi = \frac{2E}{\pi K H}\left(\frac{\sigma_s}{R}\right)^{0.5} \tag{3.28}$$

with

$$P = \frac{2}{3} H A_n \pi B \omega_c \left(\int_d^{d+\omega_c} I^{1.5} + 1.03 \int_{d+\omega_c}^{d+6\omega_c} I^{1.425} + 1.4 \int_{d+6\omega_c}^{d+100\omega_c} I^{1.263} + \frac{3}{K} \int_{d+100\omega_c}^{\infty} I \right) \tag{3.29}$$

$$F_s = 2 H A_n \pi B \theta \left(\int_{-\infty}^{d} J_{nc} + 0.98 \int_d^{d+\omega_c} J_{-0.29}^{0.298} + 0.79 \int_{d+\omega_c}^{d+6\omega_c} J_{-0.321}^{0.356} + 1.19 \int_{d+6\omega_c}^{d+100\omega_c} J_{-0.332}^{0.093} \right) \tag{3.30}$$

$$Q_{\max} = \frac{2}{3\sigma} H A_n \pi B \omega_c \left(0.52 \int_d^{d+\omega_c} I^{0.982} + 1.03 \int_{d+\omega_c}^{d+6\omega_c} \begin{pmatrix} -0.011 \times I^{4.425} + 0.091 \times I^{3.425} - \\ 0.41 \times I^{2.425} + 0.851 \times I^{1.425} \end{pmatrix} \right) \tag{3.31}$$

where J_{nc}, J_c^b and I^b are given by

$$J_{nc} = 1.33\left[\left(\frac{\varepsilon}{d-z}\right)^2 - 0.25\left(\frac{\varepsilon}{d-z}\right)^8\right]\varphi_{(z)}dz \qquad 3.32$$

$$J_c^b = \left(\frac{z-d}{\omega_c}\right)^b \left(\frac{\varepsilon}{\omega_c}\right)^c \varphi_{(z)}dz \qquad 3.33$$

$$I^b = \left(\frac{z-d}{\omega_c}\right)^b \varphi_{(z)}dz \qquad 3.34$$

where Q_{max} is the maximum shear force (friction force) between the two surfaces in contact and F_s is the force of attraction. ε is the minimum possible distance between the center of two adjacent atoms and in the range of 0.4 $\overset{o}{\text{A}}$. In these equations, the $-\infty \sim d$ represents non-contacting asperities while $d \sim d + \omega_c$ represents the asperities in contact with compression within elastic limits. $d + \omega_c \sim d + 100\omega_c$ is the elastic-plastic range and the $d + 100\omega_c \sim \infty$ is the pure plastic range

A schematic of an equivalent model of a rough surface in contact with a flat surface is shown in Figure 3.5. The profile of the asperities on the rough surface changes because of the compression caused by the interaction with the flat surface. The force of attraction between the surfaces and inertial load provides the net force available for asperity compression. The distribution of the asperities heights is assumed to have a Gaussian profile with the asperities having a constant radius, R. The distance between the mean of asperities heights and the flat surface is denoted by *d* and the difference between the mean of surface heights and mean of asperity heights is denoted by h_s. The distance between a point on the asperities and the flat surface is indicated by *z*. Once the flat surface comes in contact with the asperities, it causes the contacting asperities to deform and change their profile as shown in Figure 3.5(b). In Figure 3.5 the non-contacting asperities contribute in the attraction force between the two surfaces represented by the first integral in equation (3.30) while the contacting asperities contribute to the forces of attraction, repulsion due to asperity compression and friction.

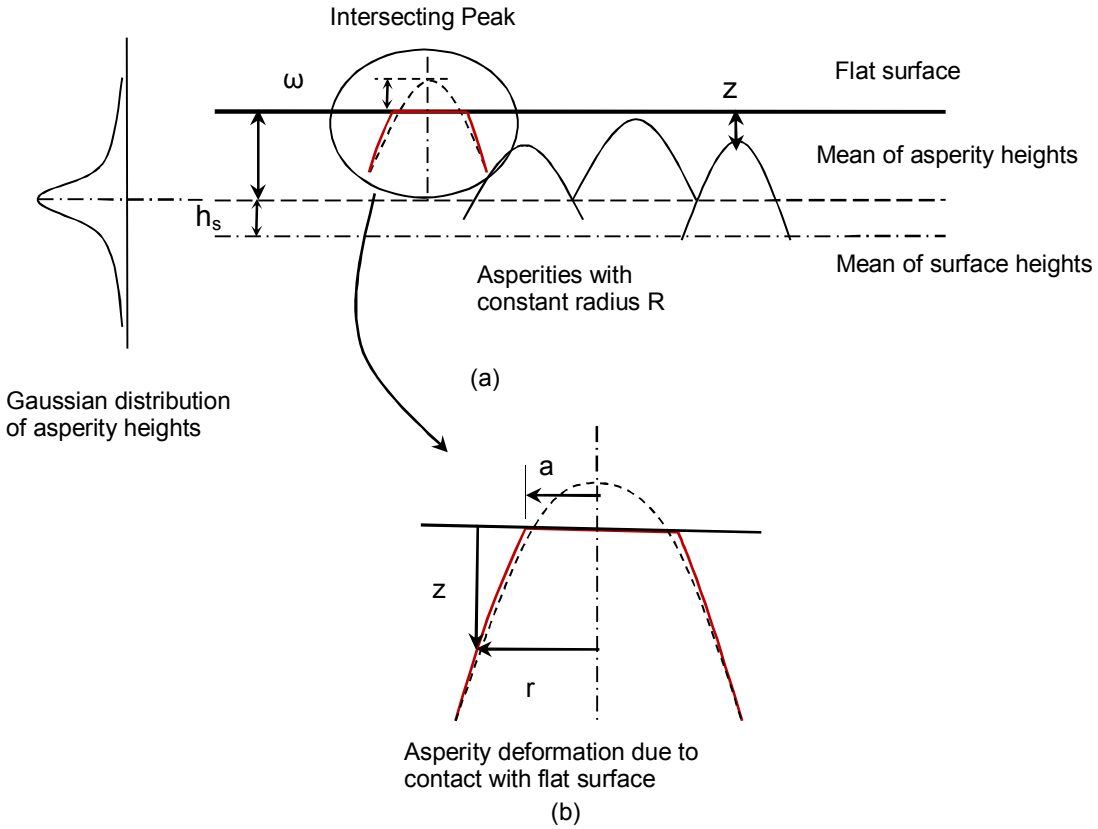

Figure 3.5: (a) Rough surface in contact with flat surface. (b) single asperity in contact with a flat surface, dotted line shows the original asperity profile where a solid line is the profile after compression. The compressed asperity has profile Z = f(r)

3.8 Development of Mathematical Model for Micropart Motion

The estimated surface forces are used to develop the dynamic model for micropart motion while in contact with or close to a deformable rough surface. The inertial force calculation is performed under the following assumptions:

- The acceleration of the micropart perpendicular to the surface is the same as the acceleration of the surface itself in the same direction as long as the micropart stays on the surface.
- The acceleration of the micropart in the direction parallel (tangential) to the surface is determined by the relative velocity of micropart with respect to the surface and the magnitude of the friction force (see friction logic section 3.9.2).

Once the surface force and inertial force are calculated, a force balance on the micropart generates the required system model. The motion of the micropart needs to be estimated parallel (tangential) and perpendicular to the deformed surface. A global stationary coordinate system (X, Y) is introduced as shown in Figure 3.6. The attraction due to surface forces, repulsion due to asperity compression and friction force on the micropart as estimated by the KE model are always parallel and perpendicular to the surface at the current location of micropart. Note that the surface is not always horizontal, as it undergoes controlled deformation by the actuator. Therefore, the motion equations need to be formulated along and perpendicular to the surface at the location the micropart is in contact with the surface. A movable or local coordinate system (α, β) is introduced that is always attached to the micropart. The local coordinate system moves and orients itself as a function of the motion of micropart and the deformable surface. The abscissa of the local coordinate is always along (tangential) the surface and the ordinate is always perpendicular to the surface. The force balance on the micropart in the local coordinate system (α, β) is evaluated using Newton's second law.

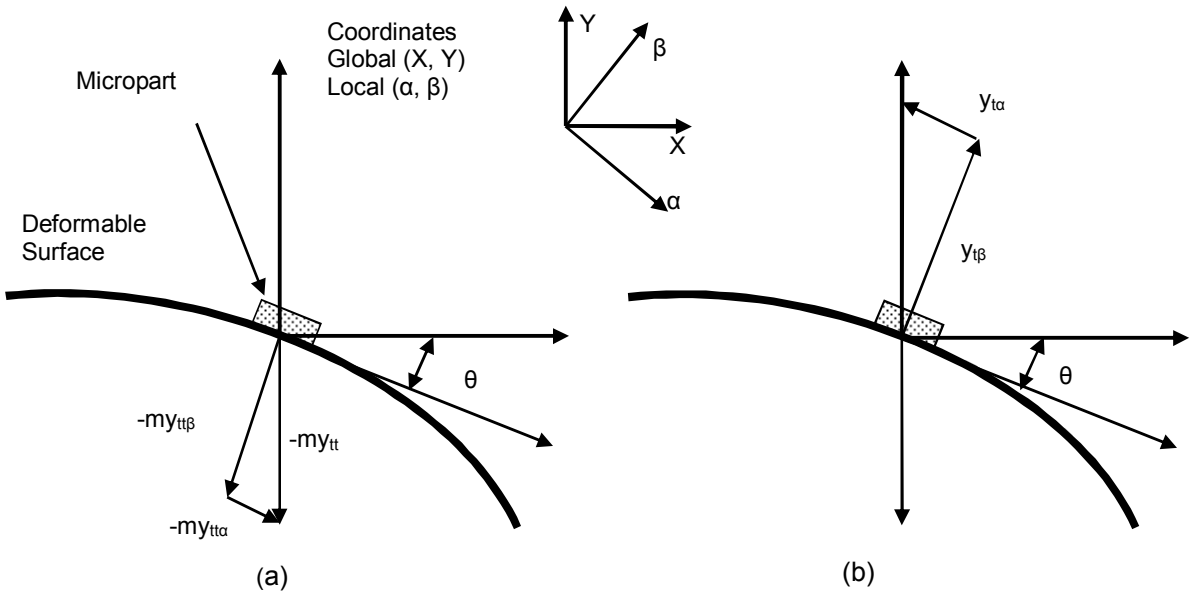

Figure 3.6: Acceleration (y_{tt}) and velocity (y_t) of the micropart while on the flexible surface; subscripts α and β represent the corresponding components along and perpendicular to the surface respectively. (a) acceleration and resultant force on the micropart (b) velocity decomposed along and perpendicular to the surface.

3.8.1 *Force balance perpendicular to surface*

The sum of the forces in the perpendicular direction is equal to the inertia of the micropart in the same direction as long as the particle stays on the flexible deformable surface. The forces along the normal to the surface are the surface force of attraction, repulsion force due to compression of asperities and the component of inertia force along the normal to the surface as shown in Figure 3.7 and represented by equation (3.35)

$$\vec{a}_{p_\beta} = \frac{\sum \vec{F}_\beta}{m} = \frac{\vec{F}_{surf\_attr,\beta} + \vec{F}_{asp\_comp,\beta} + \vec{F}_{inertia,\beta}}{m} = \vec{a}_{s\beta} \qquad 3.35$$

where β indicates the direction in the local system, F_β represents the vector sum of all forces in the direction normal to the surface, m is the mass of the micropart and $a_{p\beta}$ is the acceleration along the normal to the surface. In a numerical simulation, the solution of equation (3.35) requires one to calculate all three forces at every time instant and integrate to estimate the micropart motion along the normal to the surface. But this process is the same as imposing a condition that the micropart stays on the surface at all times. Therefore, in the simulation, to reduce the computation burden, this approach is used to estimate the micropart motion in the direction perpendicular to the surface. The surface state at the point of contact is estimated at each time instant and the position of the micropart is updated accordingly.

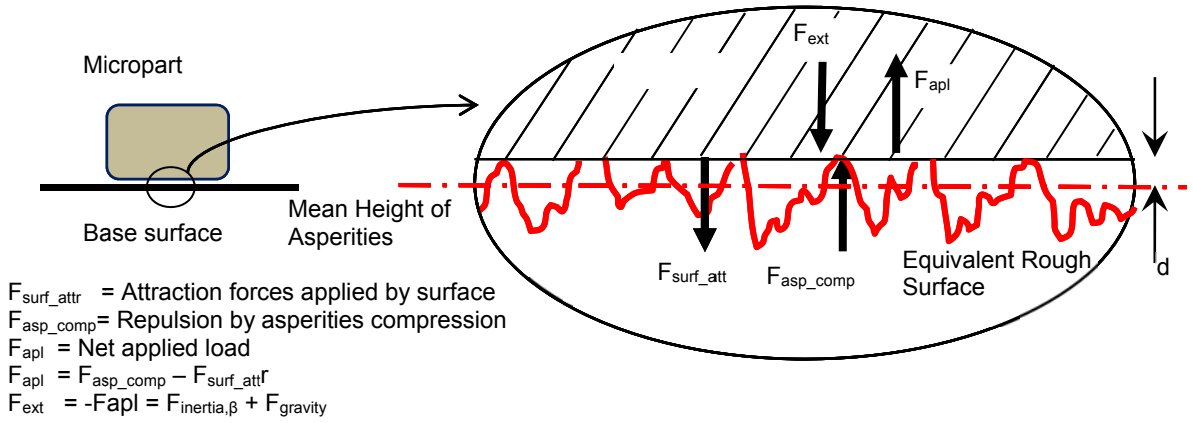

Figure 3.7: Forces acting on micropart and surface

3.8.2 *Force balance parallel to surface*

The acceleration in the direction parallel to the surface is determined by the forces in the same direction. The forces in the tangential direction (α) are the component of inertial force along the surface and the instantaneous value of friction force. The micropart motion equation parallel to the surface is given by

$$\begin{aligned} \vec{a}_{p\alpha} &= \frac{\sum \vec{F}_{\alpha}}{m} = \frac{\vec{F}_{inertia,\alpha} - \vec{F}_{friction,\alpha}}{m} && \left(\text{if micropart slips on the surface}\right) \\ &= \vec{a}_{s\alpha} && \left(\text{if micropart sticks with the surface}\right) \end{aligned} \qquad 3.36$$

where F_{α} represents the vector sum of both forces along the surface, m is the mass of micropart, and $a_{p\alpha}$ is the acceleration of micropart along the surface and $a_{s\alpha}$ is the resolved acceleration of the surface along the surface. The friction force estimated by the KE model is not the force used in the simulation directly. The direction and magnitude of the friction force is evaluated using a friction logic sequence as discussed in section 3.9.2.

Equations (3.35) and (3.36) describe the motion of the micropart in the local coordinate system, but motion in local coordinates has no physical meaning as it is always attached to the micropart and adjusts its orientation at each time instant based on the local surface profile. Therefore, these motion equations cannot be integrated directly. A numerical scheme needs to be developed to estimate the changes in micropart state and convert the state differential changes to changes in global coordinates. Using the differential changes in the micropart state in global coordinates and the knowledge of the previous micropart state, the new micropart state is evaluated. The conversion from local to global coordinates and vice versa is performed using standard rotation coordinate transform. More explanation of the numerical process is available in section 3.10.

3.9 Implementation

The numerical implementation of the system dynamic model expressed by equations (3.35) and (3.36) requires the sequential evaluation of the system parameters in a step-by-step manner. In addition to parameter evaluation, certain assumptions are made. The details of these necessary assumptions are discussed in subsections 3.9.1 through 3.9.8.

3.9.1 *Static and Dynamic Friction*

The coefficient of friction, being a function of normal applied load, is evaluated at each time step in the integration scheme. The KE model estimates the static friction coefficient and friction force between the mating surfaces where the motion of the micropart on a flexible surface requires evaluation of the dynamic friction coefficient. The KE model was extended to calculate the dynamic friction for lubricated surfaces by Feng and Kenjo [48]. However, the focus of this research is micropart motion in a dry-friction environment and their work cannot be utilized. In the open literature, models have been developed to simulate sliding contacts and to estimate the dynamic friction coefficient between rough surfaces [49-51], however these models neglect the surface force of attraction and as such cannot be employed for analysis at the microscale.

The static friction force is often considered as an upper bound of the friction force because the strength of junction of the contacting points increases as the time of stationary contact increases [49]. If the static friction coefficient is used in the analysis, the obtained results will be conservative. Also, as noted by Martins et al. “Contrary to general opinion, no distinction can be made between static and dynamic coefficient of friction and experimental observation of the difference between static and dynamic friction coefficient are not necessarily intrinsic properties of dry contact. Dynamic properties of experimental apparatus and external perturbations may lead to this difference” [49, 51].

An exhaustive literature survey did not yield a mathematical model to calculate the dynamic friction coefficient between non-lubricated rough surfaces at the microscale considering the dynamic interaction and effect of attraction force, surface roughness, asperity deformation and distance of the micropart from the surface. The dynamic friction coefficient is a function of roughness and material

properties of contacting surfaces. Experimental data in the published literature provide clear evidence that the dynamic friction coefficient value is close to the static one according to time dependent data as shown in Figure 3.8(a, b, c) [52, 53]. Therefore, the proposed analysis considers the value of static friction coefficient as an acceptable conservative upper bound value of the dynamic coefficient of friction.

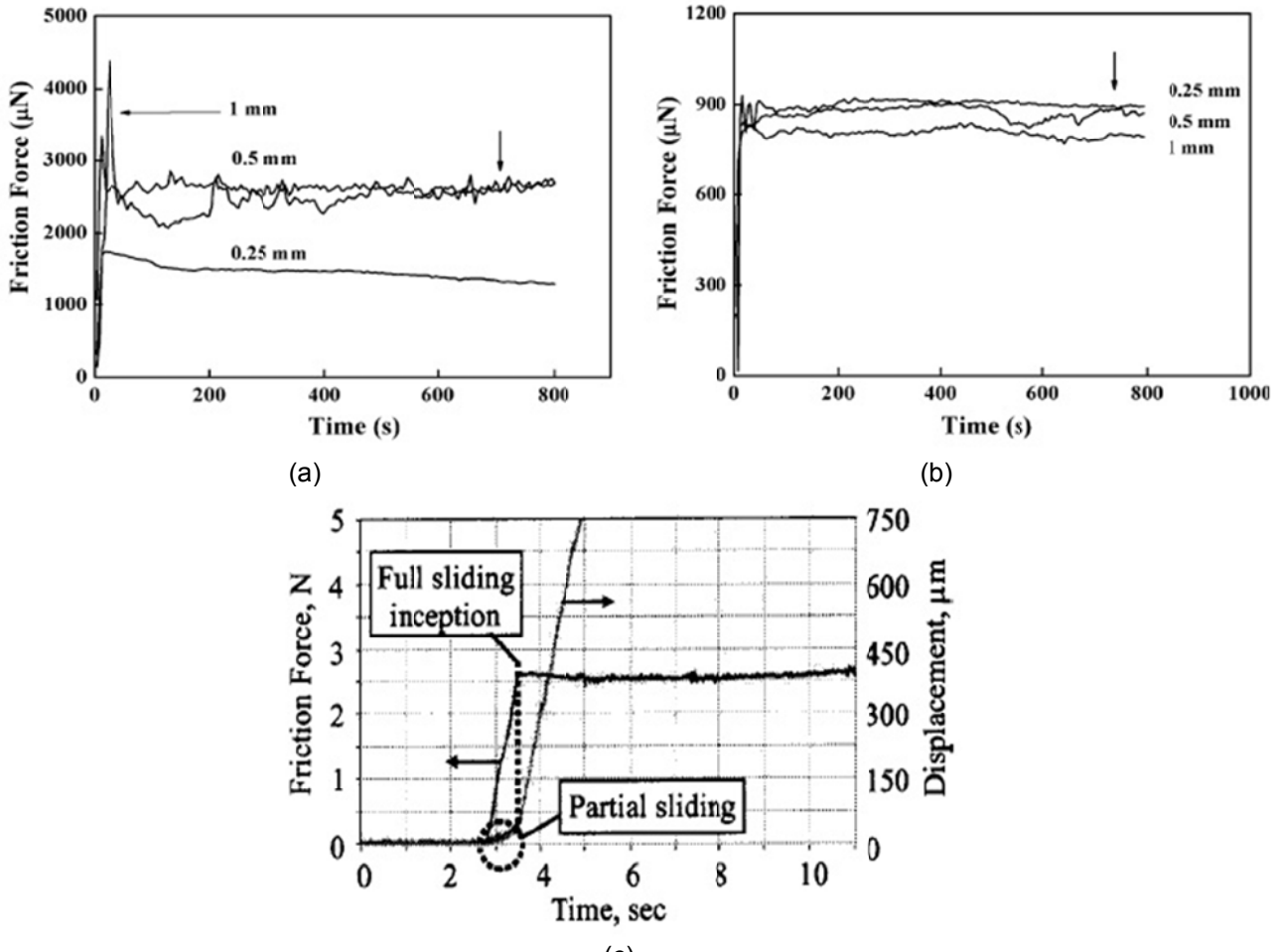

Figure 3.8: Variation of friction in a sliding test (a) Si wafer (b) DLC (c) copper ball against steel.[52, 53]

In this research, an equivalent quasi-dynamic coefficient of friction (COF) is evaluated by employing the KE model to calculate an instantaneous static COF based on the current system state at the beginning of every integration time and is assumed to remain constant during the integration time step. For the next integration time step, a new COF is evaluated based on the changed system state

especially due to effects such as attraction and repulsion microforces. In essence, a new COF is estimated at each time step, thus making it a quasi-dynamic COF.

3.9.2 *Friction Force Evaluation Logic*

The system dynamics are a function of the nonlinear behavior of the friction force or COF which is a function of surface roughness, asperity contact and deformation, surface attraction force and distance of the micropart from the surface. The motion equation parallel to the surface is examined and analyzed under the conditions that 1) the micropart slips on the surface or 2) the micropart sticks with the surface

In addition, note that the direction of the friction force is always opposite to the motion of the micropart. Moreover while the micropart sticks on the surface, the friction force on the micropart is not equal to the maximum possible value supported by the asperity contacts. The friction force is equal to its maximum possible value (considering the current value of normal inertia force) when the micropart is at the verge of slipping or is already moving relative to the surface. This dynamic evaluation of friction force is implemented using a friction logic sequence.

The friction logic sequence for defining the friction force/coefficient as implemented in the proposed dynamic model uses the relative velocity between the micropart and deformable surface to estimate hysteresis and stick-slip behavior [54]. The governing equations are functions of the relative velocity (v_{rel}) between the surface velocity (v_{surf}) and micropart velocity (v_{part}) evaluated along the abscissa of the local coordinate system (tangential to the surface) according to

$$\vec{v}_{rel} = \vec{v}_{surf} - \vec{v}_{part} \tag{3.37}$$

If the relative velocity of the micropart with respect to the surface is zero, then the friction force is set equal to the tangential component of the inertia force on the micropart and the acceleration of the micropart is equal to the acceleration of surface (equation 3.38). If the relative velocity has a non-zero value, the magnitude of the friction force is equal to its maximum possible value (the value from KE model using the current value of component of inertia force along the ordinate of local coordinate system) and the friction force direction is set opposite to the direction of the relative velocity (equation 3.39).

$$\vec{a}_p = \vec{a}_s \tag{3.38}$$

$$\vec{a}_p = \frac{\vec{F}_{fric} + F_{tot}}{m} \tag{3.39}$$

where F_{fric} is the friction force, F_{tot} is the summation of inertia and gravity forces along the surface, and a_p is the acceleration of micropart. In order to implement this event based logic in a numerical simulation with hysteresis and stick-slip behavior, a threshold value of the relative velocity must be defined. In the proposed model, the threshold value of the relative velocity depends on the friction force, integration step size and micropart mass.

The velocity threshold, v_{th}, is defined as the maximum velocity of the micropart that upon an externally applied force, F_{tot}, opposing the micropart motion, the micropart could be decelerated to complete stop (zero velocity) ($v_f = 0$) within one integration time step, Δt, [54].

$$\vec{a} = \left(\vec{v}_{th} - \vec{v}_f\right) \Big/ \Delta t \tag{3.40}$$

$$\vec{a} = \vec{F}_{tot} \Big/ m = \vec{F}_{friction} \Big/ m \tag{3.41}$$

$$\vec{v}_{th} = \left(\vec{F}_{friction} \times \Delta t\right) \Big/ m \tag{3.42}$$

The flow diagram for the friction logic is shown in Figure 3.9. If the relative velocity, v_{rel}, is less than the threshold velocity, v_{th}, and the magnitude of the threshold velocity is reducing, the micropart will come to a complete stop with respect to the surface and the acceleration and velocity of the micropart will become the same as those of the surface. If the value of the relative velocity is less than the threshold velocity and the absolute value of relative velocity is increasing, then the acceleration of the micropart is determined by the net applied force. In the analysis, note the sign of the friction force is always opposite to the direction of relative velocity. The value of the threshold velocity is continuously varying and must be estimated at each integration time step since it is a function of the dynamically changing friction force.

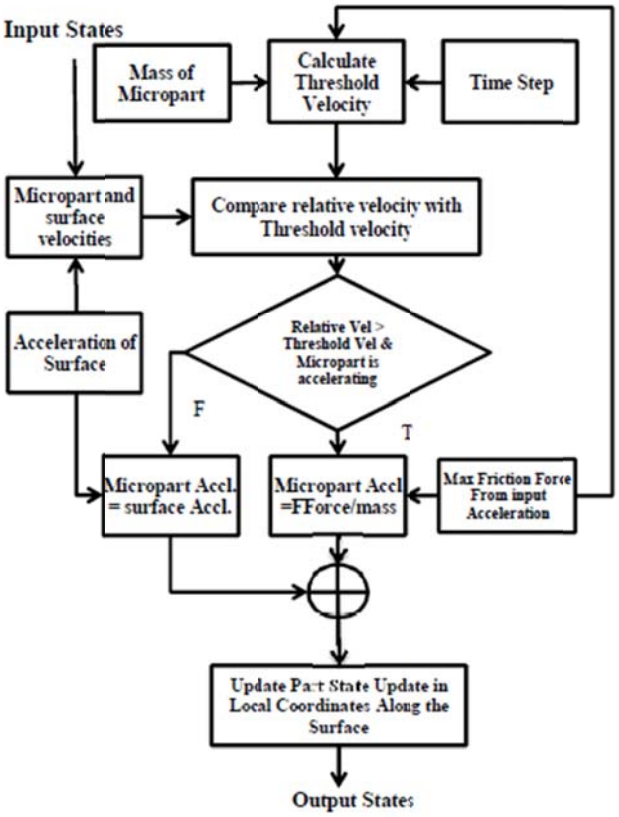

Figure 3.9: Friction logic flow chart

3.9.3 *Friction Model Inversion*

In the proposed system dynamics model , the applied normal force is an input while the friction force and the surface force of attraction are to be evaluated. The normal force on the micropart, friction force and contact area due to asperity compression are evaluated by the friction model that requires as inputs the material properties of contacting surfaces, their surface roughness and the separation distance between them. Thus, in order to estimate the friction and attraction forces as function of applied external load, the friction model must be inverted.

The friction model is not represented in the form of explicit equations (equations 3.29~3.31) which could easily be analyzed and inverted. In order to accomplish the friction model inversion, a data set for the applied load is generated for a range of separation distance values for the defined surface roughness and material properties. The estimated data of the applied load as a function of separation distance is

used to identify an explicit equation through curve fitting. This explicit curve fit equation is used during the simulation to estimate the nominal distance between the two surfaces which is then used to evaluate the dynamically changing attraction and friction forces at each time step as function of the nominal separation distance between the two surfaces. Note that, if any of the surface roughness, surface material or micropart material change, then the applied load as function of separation distance must be re-evaluated and a new curve fit equation derived.

This procedure is applied using data generated for two steel surfaces with standard deviation of surface roughness, σ_n = 20 nm, and plasticity index, ψ = 2.5, a graph of applied load as a function of separation distance is generated and shown in Figure 3.10(a). The identified curve fit is presented in equation 3.43 and shown in Figure 3.10(b).

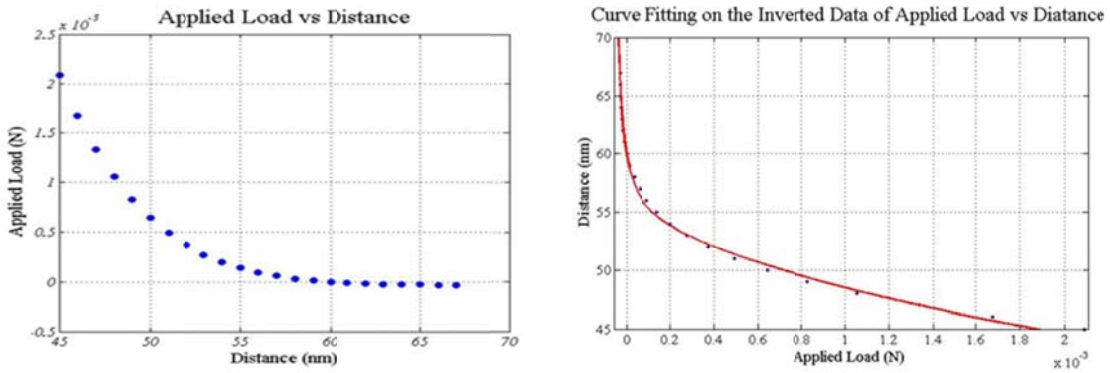

(a) (b)

Figure 3.10: (a) Estimated applied load as function of separation distance (nm) and (b) curve fit corresponding to steel surfaces with σ_n = 20 nm and ψ = 2.5

The curve fit equation for the assumed conditions and parameter values was evaluated as a rational curve using the Curve Fit Toolbox of MATLAB. The resultant equation for separation distance, *d*, in nanometers as function of applied force, F_{app}, in Newton with goodness of fit SSE = 0.02223 and R^2 = 0.999 is given by

$$d = \frac{69.86F_{app}^4 + 0.0494F_{app}^3 + 2.885\times10^{-6}F_{app}^2 + 4.249\times10^{-11}F_{app} + 1.839\times10^{-16}}{F_{app}^5 + 1.37F_{app}^4 + 7.569\times10^{-4}F_{app}^3 + 4.0314\times10^{-8}F_{app}^2 + 5.7\times10^{-13}F_{app} + 2.436\times10^{-18}} \quad 3.43$$

3.9.4 *Surface Compliance*

In this research, actuation is achieved by the controlled deformation of a flexible surface. In the proposed surface model, the surface is assumed to have infinite localized stiffness through its thickness, i.e. the deformation profile at the top and bottom of the surface are assumed to be the same. Thus, surface compliance is not considered. The acceleration and velocity generated by an actuator attached at the bottom of the surface are assumed to be the same on the top of the surface due to no compliance assumption.

3.9.5 *Separation Distance between Micropart and Surface*

When the two surfaces are in contact, the surface attraction force pulls the two surfaces together causing the asperities to compress which in turn generates a repulsive reaction force between the two surfaces. The net applied load on the micropart is the difference between these two forces as shown in Figure 3.11. If the distance between the two surfaces becomes “very small” as determined from the mean of asperity heights line, indicates high asperity compression and the reaction force due to the compression of asperities could be larger than the force of attraction. In order for the micropart to be in equilibrium, the net force must be balanced by an externally applied load. Increasing the separation distance will decrease the contact load at a faster rate than the rate of decrease of the force of attraction as shown in Figure 3.11(a). Thus, by increasing the surface separation distance, a state is reached where the force of attraction is equal to the applied load. This state represents the compression of asperities due to the attraction force between the surfaces. This balance point is represented by point B in Figure 3.11(b) corresponding to a separation distance of 76 nm between the two rough surfaces.

Further increasing the separation distance up to a threshold value, the surface attraction force becomes larger in magnitude than the reaction force due to asperities compression and consequently the applied load becomes negative. This indicates that in order to increase the separation distance beyond this point, one must exert a pull force. The minimum force point in Figure 3.11(b) represents the maximum pull force required to separate the two surfaces. In the proposed dynamic model, the micropart would detach from the surface once the acceleration component perpendicular to the surface generates an

inertial force larger than the maximum pull force represented by point A in Figure 3.11(b) and the corresponding separation distance between the surfaces is found to be 85 nm. Note that Figure 3.11 is generated using the KE modeling equations 3.29~3.31 with parameter values σ_n = 20nm, $\Delta\gamma$=1 J/m^2, H=1 GPa, ε = 0.4, and A_n = 10-8 m^2.

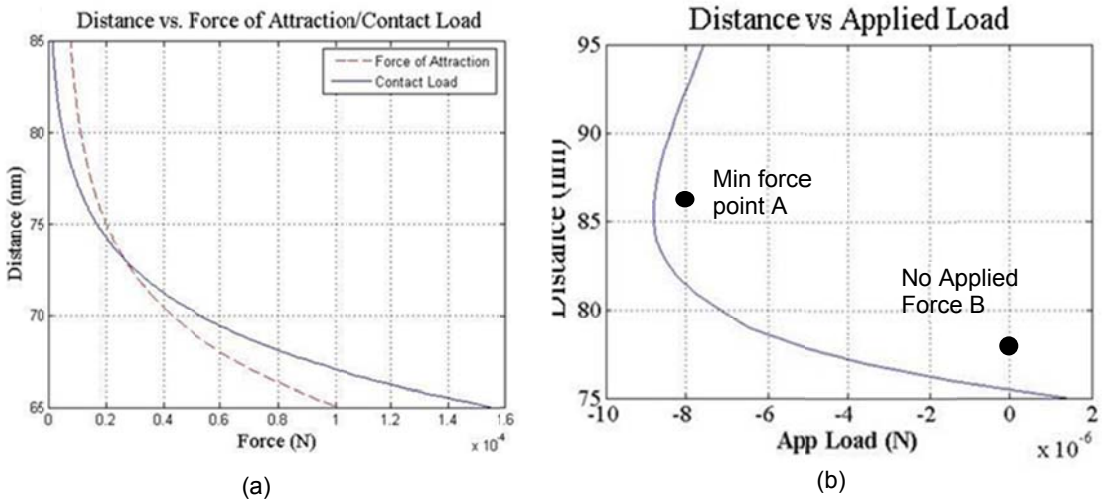

(a) (b)

Figure 3.11: Separation distance vs. Forces acting on the micropart. σ = 20nm, Δγ=1 J/m2, H=1 GPa, ε = 0.4, An = 10-8 m2 (a) separation distance as function of contact and attraction force, the graphs intersect at 73nm (b) Separation distance vs. Applied load. Minimum point marked on the applied force graph represents the maximum pull off force required to separate two surfaces.

3.9.6 *Asperity Density*

The surface roughness has an a priori defined asperity density. The surface roughness characteristics would change when the surface is stretched or deformed. However, in order to establish the feasibility of the proposed process, the initial numerical scheme is developed with the assumption of constant asperity density and thus the effect of stretching of the flexible surface on the asperity density is neglected. The analysis in chapter 5 accommodates time dependent surface deformation and its effects on surface roughness and asperity density in an augmented model.

3.9.7 *Area of contact*

The nominal area of contact between the micropart and the surface is assumed to remain constant even when the surface is deformed.

3.9.8 *Condition for the Micropart to Detach from the Surface*

The forces acting on the micropart while in contact with the surface are the attraction force generated between the two surfaces and the repulsive force due the compression of the asperities as shown in Figure 3.7. A net applied force is defined as the difference between the compression and attraction forces. This net applied force must equal to an externally applied force (same magnitude but opposite direction) if the micropart is to be in equilibrium. If the input acceleration is such that the micropart overcomes the attraction and gravity forces, the micropart will detach from the surface causing the system or micropart motion dynamics to change. The motion of the micropart once it detaches from the surface, even though it could be of interest, is beyond the scope of the present research and will not be further discussed.

3.10 Solution Methodology

The set of the derived dynamic equations representing a non-linear, discontinuous system, are numerically integrated using a custom written 4^{th} order Runge-Kutta integration scheme. The state of the micropart is monitored at each integration time step as the micropart interacts with the surface for conditions of sliding (translocation), stick-slip (stopping) or detachment and updated accordingly. The flowchart of the solution sequence or simulation logic followed is presented in Figure 3.12. Inputs to the system are the surface deformation due to actuator motion, actuator acceleration and deceleration, surface roughness, material properties and previous states of the micropart while the output is the updated state of the micropart.

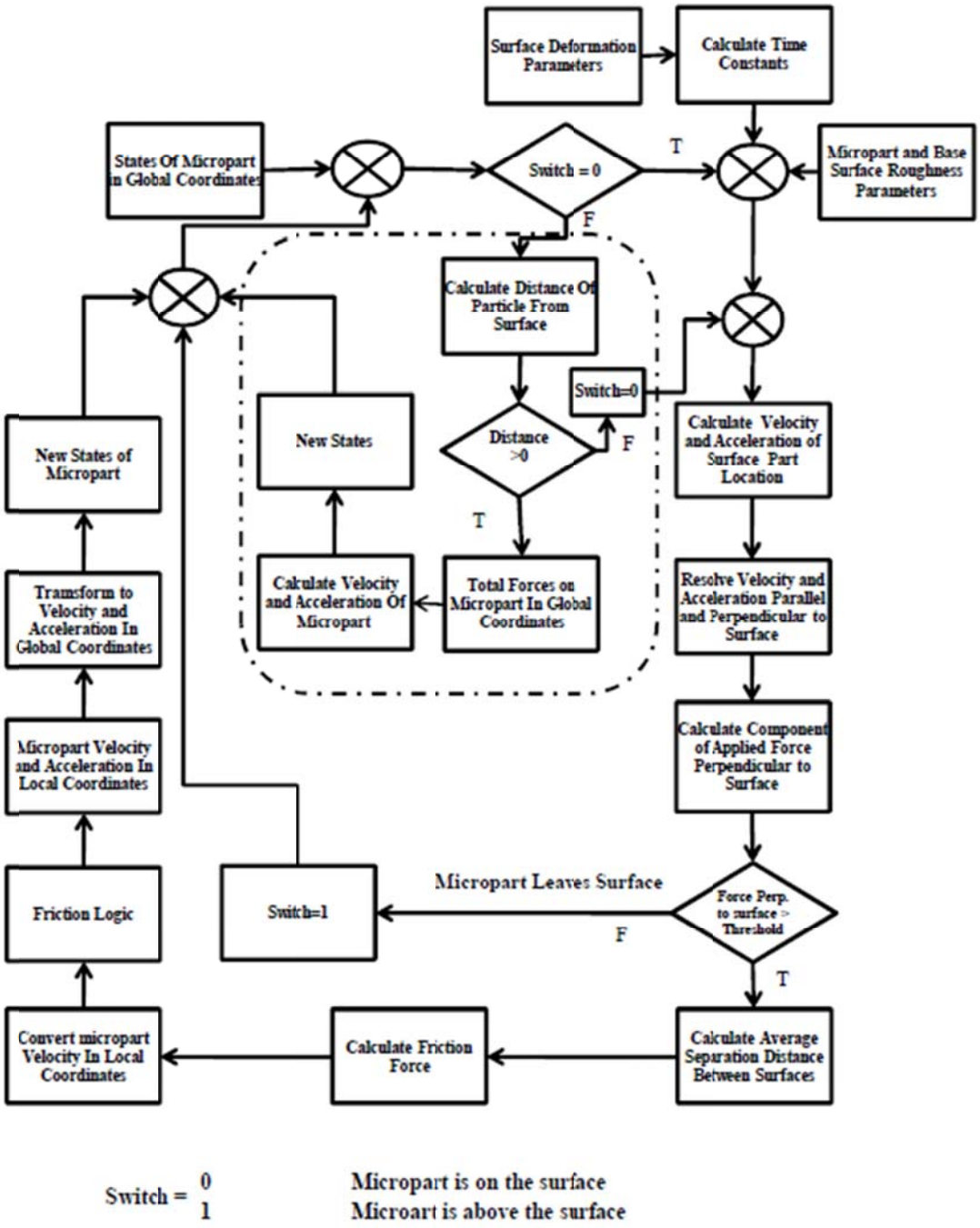

Figure 3.12: Flowchart of simulation logic flow for assessing micropart motion on a deformable surface

In the solution approach, two coordinate systems are employed; a fixed global coordinate system and a local coordinate system always attached on the micropart and orienting itself with the local surface deformation profile. The system equations are derived in the local coordinate system while the movement

of the micropart needs to be estimated in the global coordinate. The analysis goes back and forth from local to global coordinates during the course of the solution. The two coordinate systems and the micropart at different instances of undeformed, purely tilted and deformed surface are shown in Figure 3.13 a, b, c respectively.

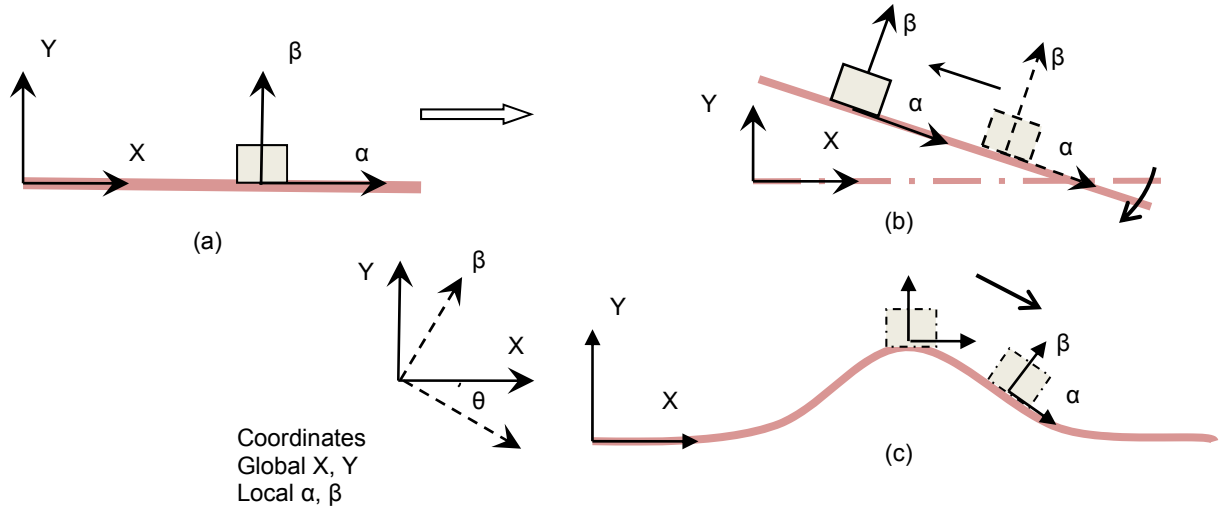

Figure 3.13. Global and local coordinate systems. (a) original surface with part resting on it; (b) tilting surface and (c) surface under controlled deformation

At each time step during the simulation process, the input surface velocity and acceleration at the location of the micropart are known in global coordinates and are expressed in local coordinates. The input acceleration along the ordinate (perpendicular to the surface) (abscissa and ordinate will be used only for local coordinates) is used to calculate the inertia forces normal to the surface and the condition of detachment. Using the inverted KE model, the external acceleration value is used to evaluate the mean separation distance between the surface and the micropart which is ultimately utilized to determine the instantaneous value of coefficient of friction. The acceleration along the abscissa (tangential to the surface) is used to calculate the force on the micropart. The velocities along abscissa and ordinate are used to estimate the updated position in local coordinates. The derivatives of the states are transformed to global coordinates and all four states in global coordinates are updated for the next solution time step.

The friction force, being a function of the normal force, varies as the acceleration of surface along the ordinate changes. The state of the micropart in the global coordinate system is transformed into the

local coordinate system. Using the velocity of the surface and the transformed velocity of the micropart, the relative velocity between the surface and micropart are calculated at the micropart location in the tangential direction. This value is compared with the threshold velocity (again estimated at each time step) to determine the relative motion of the micropart with respect to surface during the next integration time step. If the relative velocity is larger than the threshold value, the micropart will not be attached or stick to the surface during the next time step. If the relative velocity is smaller than the threshold value, the micropart could stick to the surface or continue sliding (slipping), depending on the stick-slip condition. The stick-slip condition is evaluated based on the derivative of the absolute value of the relative velocity; if this derivative is negative, the micropart will stick on the surface. Once it sticks to the surface, its velocity and acceleration for the next time step in the analysis are assigned the same values as those of the surface (whether the surface is undergoing deformation or not). If the value of this derivative is positive, the micropart will continue sliding during the next time step. Using the equations of motion (3.35 and 3.36) the differentials of the micropart state are estimated in the local coordinates and are transformed to the global coordinates. The new micropart state is estimated from the values in previous time instant and the differentials at current time instant.

The numerical solution scheme is developed according to the flowchart (Figure 3.12) to track the motion of the micropart on the flexible surface. The state of the part and the parameters of the surfaces in contact are the input to the system and the output is the state of the micropart at the end of the integration time step. The discontinuity of the acceleration because of the switching between the stick and slip between the micropart and the surface shown in equation 3.38 and 3.39 and because of the nonlinear and discontinuous friction force, results into the non-differentiable path of the micropart

3.11 Motion Feasibility

The first step in assessing viability of the proposed approach is to establish the feasibility of controlled motion of a micropart due to controlled surface deformation with possible application to positioning and orientation for microassembly processes.

Table 3.1: Input parameters for feasibility study

Description	Variable	Values and Units
Standard deviation of surface roughness	σ_n	20 nm
Surface area (contact area)	A_n	100μm x 100μm
Thickness of micropart	T	10 μm ~100 μm
Poisson's ratio	υ	0.33
Plasticity index [37]	ψ	2.5
Difference in surface energy [37, 38]	Δγ	1 J/m^2
Hardness of material [37]	H	200 HB
Micropart mass	M	2 x 10^{-9} kg

The lower bound of the acceleration input required for the initiation of motion is determined by analyzing the motion of a micropart on a flat surface with input acceleration along the surface as schematically represented in Figure 3.14.

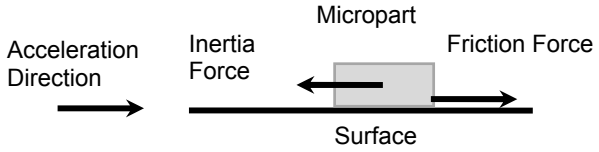

Figure 3.14: Schematic of micropart on flat surface with acceleration input along the surface

This represents the case where the input acceleration to the system is used to overcome only the friction force between the micropart and the surface. If the inertia force generated by the input acceleration is larger than the friction force, the micropart will slide relative to the surface. The friction force is calculated according to the KE model while the input acceleration required to initiate motion must be provided by an available actuation mechanism. Data for the force of attraction, friction force and friction coefficient are generated using the values of the parameters for surface and micropart presented in Table 3.1. The graphs of the friction force, the coefficient of friction and the applied load are shown in Figure 3.15. The applied load decreases with the increase of the separation distance and becomes

negative. The negative represents that a pull force is required to separate the two surfaces apart. The friction force also decreases with the increase of the separation distance while COF has discontinuous behavior. The negative value of the coefficient of friction is due the change of sign of applied force which becomes negative after a certain separation distance as discussed in section 3.9.5. The friction force is calculated according to the KE model which requires as input the separation distance between the two surfaces. This separation distance is estimated using the "Distance vs. Applied Load" curve in Figure 3.11(b) for the corresponding parameters of surface roughness and material constants. In this particular example, since the surface is not deforming, there is no acceleration in the normal direction and the only normal applied load is the micropart weight. Using this applied load, the separation distance is found either from the graph or the curve fit equation. Once the separation distance is known, the friction force is calculated using the "Friction Force vs. Distance" curve in Figure 3.15(b) or using the friction force equation, (equation (3.31)) in the set of KE equations. The friction force for this particular example is found to be 8×10^{-8}N (or 0.08 μN). The coefficient of friction as function of the separation distance is shown in Figure 3.15(c). This plot is generated by evaluating the instantaneous COF based on the KE model at the beginning of each integration time step as discussed in section 3.9.3.

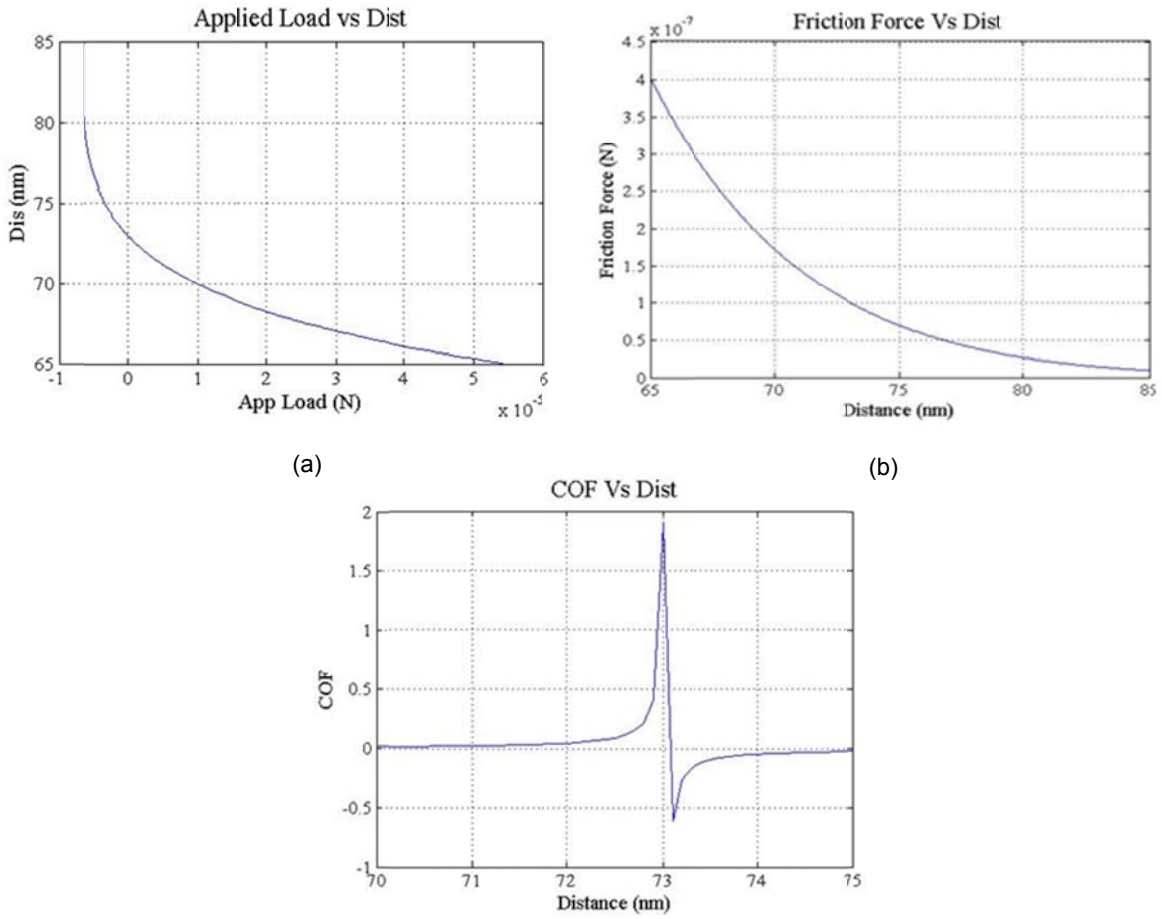

Figure 3.15: (a) Separation distance vs. Applied Load (b) Friction force vs. Separation distance (c) COF vs. Separation distance

Motion could be initiated if the component of input inertial force parallel to the friction force is greater than the friction force. At the threshold of motion initiation, these two forces will be equal and the instantaneous micropart acceleration could be evaluated according to

$$\vec{F}_{friction} = \vec{F}_{inertia} = m\vec{a}$$
$$\vec{a} = \vec{F}_{friction} / m = \frac{8\times10^{-8}}{2\times10^{-9}} = 40\ m/\sec^2 \qquad 3.44$$

Thus, if the applied acceleration along the direction of motion satisfies $\vec{a} \geq 40\ m/\sec^2$ (using the values in Table 3.1), the micropart will start moving on the base surface.

The second criterion to be considered for motion feasibility is to assess whether a desired travelled distance for a specific actuation configuration could be achieved. The distance travelled by the micropart cannot be evaluated in closed form or through simple symbolic variable substitutions considering the nature of the highly nonlinear and integral modeling equations, thus one must resort to numerical simulation. The numerical simulation algorithm and event logic presented in Figure 3.12 is used to calculate the distance travelled by the micropart.

A case where the surface is deformed by an actuator attached beneath the flexible surface is considered as this configuration is more realistic for the practical implementation of the proposed approach for micropart translocation as shown in the schematics in Figure 3.1(b) and Figure 3.13(c). A micropart placed on the top of a flat surface will experience an inertia force during surface deformation (it is assumed that the surface has no compliance through the thickness and that the asperity distribution remains constant). The component of the inertia force along or tangential to the surface will cause the micropart to either move along the surface or remain stationary. The instance presented in Figure 3.1(b) shows the micropart sliding along the surface. In addition, Figure 3.1(b) shows the parameters that define the actuator stroke, h_f, and surface deformation wavelength *WL*. Note that the actuator motion during the upward and downward strokes is controlled.

In addition to the parameters tabulated in Table 3.1, the surface deformation profile, without loss of generality, could be any deformation attainable by the actuator and surface material characteristics. In the initial feasibility study, the surface deformation profile, $\chi(x,t)$, is assumed to be Gaussian and given by

$$\chi(x,t) = f(t)e^{-\frac{(x-\mu_{su})^2}{2\sigma_{su}^2}} \qquad 3.45$$

This deformation is a non-normalized time dependent Gaussian profile where *f(t)* is a time dependent function whose value depends on the actuator position and velocity profile. The non-normalized form is used to keep the deformation wavelength (WL) constant while changing the deformation amplitude (actuator stroke, h_f).

The deformation wavelength is set to be 0.6 mm and the maximum actuator stroke is defined to be 200 μm. The position profile of the actuator for the initial feasibility analysis is defined to be quintic i.e. ($d = a_0 + a_1 t + a_2 t^2 + a_3 t^3 + a_4 t^4 + a_5 t^5$) since it allows for the definition of the initial and final position, velocity and acceleration, and provides more control on jerk; note that, the developed analysis could be easily modified to accommodate any desired actuator position profile and surface deformation wavelength. The constants of the quintic polynomial are estimated by enforcing a set of boundary conditions on the actuator motion for each of the upward and downward strokes; the initial and final velocities are set to zero, the initial and final accelerations are set to zero, the initial position of the actuator is zero and it reaches its maximum upward stroke (h_f) at half of the defined time period.

The upward and downward strokes are assumed to have the same velocity profile indicating that the actuator is retracted in the same manner that it was extended and in the same amount of time. For the initial analysis it is assumed that there is no dwell time between the up and down strokes of the actuator. The analysis is performed to simulate a single actuator up and down stroke at a frequency of 950 Hz. Note that the actuator frequency is solely an indication of how fast the actuator operates and by no means does it imply that the actuator continuously vibrates the surface at that frequency. In the presented analysis, the results are obtained for a single actuator upward and downward stroke. The estimated friction force from the analysis as function of time is shown in Figure 3.16(a) and the horizontal component of the micropart velocity (in global coordinate system) as function of time is shown in Figure 3.16(b).

In the acceleration phase of the up (upward) stroke, the component of inertia force perpendicular to the surface (along ordinate of local coordinate system) is negative generating a high friction force where during the deceleration phase of the upward stroke the inertia force reverses direction resulting into decreasing the friction force as shown in Figure 3.16(a).

During the acceleration phase of the actuator up stroke, the micropart gains positive velocity as shown in the “Velocity vs. Time curve” in Figure 3.16(b). However, the gain is small because of the high friction force, the small value of the slope of the deformed surface and the resultant small value of inertia

force along the surface. On the contrary, during the deceleration of the upward stroke, the slope of the deformed surface is larger thus generating a larger component of the inertia force along the abscissa of the local coordinate. High inertia with comparatively lower friction force along the surface would result into a higher velocity gain. Similar behavior is also observed in the downward stroke.

The negative velocity of the micropart motion shown in Figure 3.16(b) shows the direction of micropart travel. While initial location of the micropart is positive with respect to actuator location, single up and down stroke will force it to move uphill as shown in Figure 3.1(b) and continue travel in the negative direction till it expends its kinetic energy due to friction on the carrier surface.

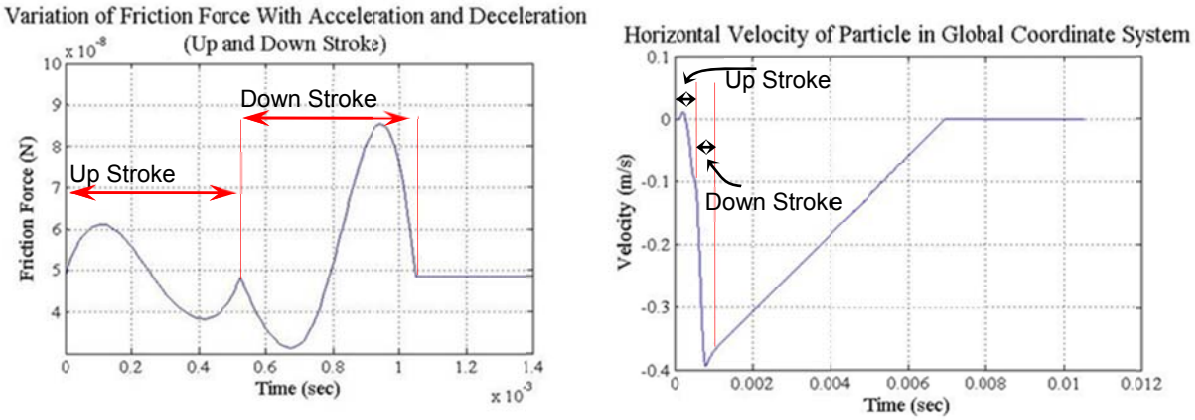

(a) (b)

Figure 3.16: (a) Friction force during actuator movement and (b) micropart velocity during complete stroke

The distance travelled by the micropart for a range of input frequencies is estimated and presented in Figure 3.17. According to Figure 3.17, the net unidirectional distance travelled by the micropart is 1250 μm for an actuator frequency of 950 Hz and stroke amplitude of 200 μm.

Note that Figure 3.17, not only represents the distance travelled as a function of the actuator input frequency but more importantly it indicates that for a given set of input parameters there is a range of feasible frequencies that could cause the micropart to translate. For the given set of input parameters, input frequencies higher that 1300 Hz will cause the micropart to detach from the surface and the lower frequency of ~300 Hz does not cause any significant micropart travelled distance of more than 10^{-5} m.

Displacements smaller than 10^{-5} m were considered as insignificant and are not reported or utilized. The lower and upper bound frequencies define a usable range for the input frequencies to cause micropart motion and to prevent it from detaching from the surface.

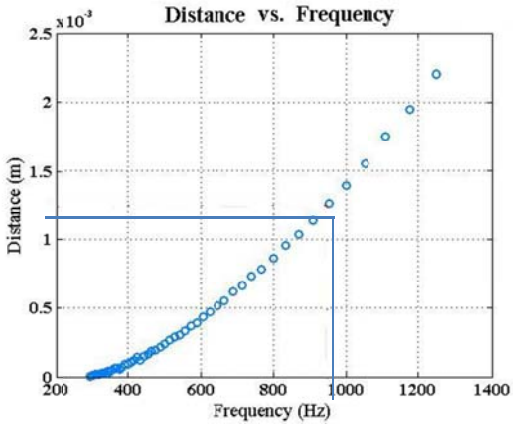

Figure 3.17: Distance travelled by micropart as function of actuator input frequency for h_f=200 μm

The developed model was also used to evaluate the effect of the actuator stroke and input frequency on the motion of the micropart. The input frequency was varied up to 1110 Hz while changing the actuator stroke from 200 to 250 μm. The simulation results with the new actuator stroke value are presented in Figure 3.18 and indicate a usable input frequency range from approximately 250 Hz to almost 1110 Hz. A comparison of the two distance travelled figures (Figure 3.17 and Figure 3.18) shows that the range of input usable frequencies depends on the input parameters.

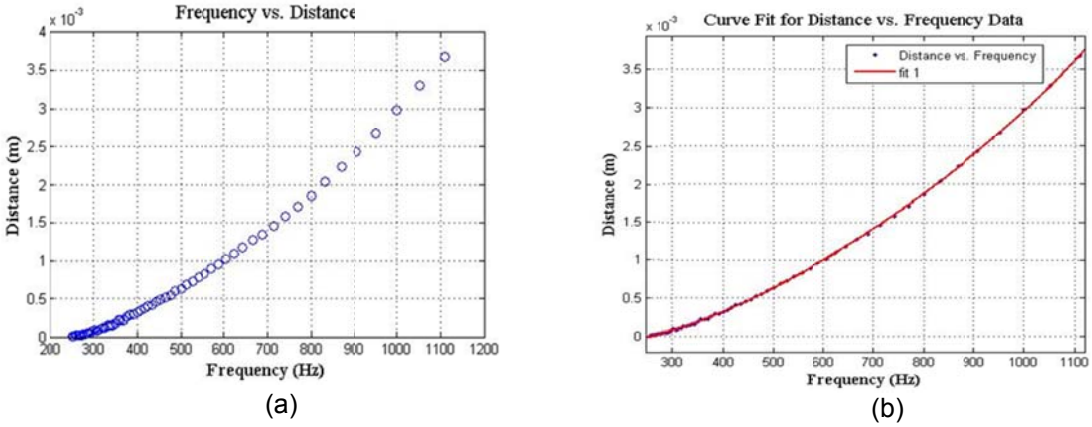

Figure 3.18: Distance travelled by micropart as function of actuator input frequency for actuator stroke 250 μm and surface energy 1 J/m^2

The "Frequency vs. Distance" data in Figure 3.17 and Figure 3.18 were also curve-fitted for the two actuator strokes of 200μm and 250 μm as shown in equations 3.46 and 3.47 respectively where Disp is the displacement in meter and *f* is the input frequency in Hz. The curve fits show 3rd order polynomial approximations with R^2 = 0.9998 for 200 μm and R^2 = 0.9997 for 250 μm. The curve fit polynomial for the 250 μm stroke is plotted in Figure 3.18(b).

$$Disp = \left(-5.21\times10^{-13} f^3 + 2.523\times10^{-9} f^2 - 5.447\times10^{-7} f - 5.23\times10^{-5}\right) meter \qquad 3.46$$

$$Disp = \left(1.81\times10^{-13} f^3 + 3.1\times10^{-9} f^2 + 3.524\times10^{-7} f + 31.9\times10^{-5}\right) meter \qquad 3.47$$

The distance travelled estimation equations (3.46) and (3.47) for the two stroke lengths could be employed to estimate the required actuator frequency that would cause the micropart to translate a desired distance for micropositioning purposes, or given a frequency of operation of the actuator to estimate the distance travelled by the micropart as function of the actuator stroke. Off-course these equations are specific to the parameters used in the developed simulation. However, if a different set of parameters is provided, then the proposed algorithm could be employed to develop another set of travelled distances and new displacement equations.

3.12 Output Sensitivity for System parameters

The proposed approach for micropart manipulation due to controlled deformation of a continuous flexible surface has been introduced. The motion dynamics of a micropart in a dry-friction environment have been developed and the feasibility study to demonstrate the viability of the proposed approach was successfully demonstrated. In this section, the developed dynamic model is used to study the sensitivity of the micropart motion and micropositioning as function of micropart and surface material properties and actuator dynamics. The developed system dynamics consider van der Waal's forces, effects of surface deformation profile, relative surface roughness, the dynamic compression of asperities and their effect on the quasi-dynamic friction coefficient based on extending the Kogut-Etsion friction model. The motion of

the micropart is affected by these parameters, and it is found that for some combinations of parameters a range exists that could cause motion while outside this range either there is no or insignificant motion or the micropart detaches from the surface. The understanding of the effects of these parameters on the micropart motion could pave the way towards controlled micropart translocation and manipulation employing a continuous flexible surface for microassembly processes requiring controlled micropart handling for homogeneous or heterogeneous microdevice mass production.

3.12.1 *Sensitivity Analysis*

The proposed approach for micropart manipulation comprises of a continuous flexible surface with microactuators rigidly attached at the bottom of the flexible surface. The output of the system is not only dependent on the input parameters but on the system variables as well. The displacement of the micropart is obviously a function of the attraction forces between the two surfaces and the input frequency which generates the inertia on the micropart to move it along the surface. For a real surface, the attraction force between the two surfaces and repulsion forces due to asperity compression are function of surface energy and surface roughness. The variation of surface energy along with the change in surface roughness will change the magnitude of the net applied force between the micropart and surface, thus affecting the output travelled displacement. The hardness of the rough surface will affect the shear force required to move one surface relative to the other. Increasing the input frequency will not only increase the inertia component parallel to the surface but will also increase the normal component of inertia as well. The net change in the output travelled displacement will be a combination of the variations for each individual system parameter.

The understanding of the effects of the various parameters on the micropart motion is essential for the design of a microconveyor for controlled micropart translocation by placing actuators at discrete locations and operating them sequentially as shown in Figure 3.2. The system dynamics is represented by equations 3.29~3.34 and 3.35~3.43. As discussed, the developed dynamics indicate a highly nonlinear, non-differentiable, discontinuous system which cannot be analytically solved with a closed form solution for the displacement of the micropart. Therefore, analytical expressions for estimating the

sensitivity due to each individual parameter cannot be derived. Thus, in order to study and understand the sensitivity of the displacement as function of input parameters, one must analyze and simulate the developed system of equations for various sets of input parameters. The data obtained from the simulation will be used for qualitative and quantitative analyses. This understanding is important during design purposes for sizing of components, for development of control algorithms or for maximizing the capability or throughput of the proposed approach. The variable and constant parameters, their corresponding ranges and values considered for the sensitivity analysis are presented in Table 3.2 and Table 3.3 with some of the parameters graphically presented in Figure 3.1(b).

The evaluated displacement of the micropart is plotted as function of the input frequency for various sets of the input parameters. A qualitative analysis is presented along with a quantitative statistical analysis. The simulation results presented in Figure 3.19 through Figure 3.26 not only represent the distance travelled by the micropart at a defined input frequency but also represent the feasible frequency range as a function of operating parameters. On each graph, the minimum frequency represents the minimum actuator frequency able to initiate micropart motion with the micropart translating at least 10 μm. This cutoff value was selected based on the size of the micropart. The maximum frequency represents the input actuator frequency which could cause the micropart to travel without detaching from the surface. At frequencies higher than this upper bound, the actuator will generate an inertia force perpendicular to the surface large enough to cause the micropart to detach from the surface.

Table 3.2: Parameters symbols and ranges of values used in this work

Parameter	Symbol (Unit)	Range
Mass of micropart	m (kg)	2 x 10-9 ~ 2 x 10-11
Actuator input frequency (an indication of how fast the actuator moves)	ω (Hz)	All feasible frequencies
Deformation Wavelength	WL (m)	600 μm ~ 1200 μm
Input Stroke Length	h_f (m)	75 μm ~ 200μm
Surface bonding energy [37]	Δγ (J/m2)	0.5 J/m2 ~ 2 J/m2
Initial position of particle	d (m)	1/6 WL ~ 2/6 WL
Roughness (relative) between micropart and substrate surfaces - standard deviation of peaks	σ_n (nm)	20 nm ~ 40 nm
Contour of surface deformation		Sinusoidal or Gaussian

Table 3.3: Constant parameters and their values

Parameter	Value
PDF of surface asperities [37]	Gaussian
Poisson ratio of surface and micropart material	0.3
Contacting cross sectional area	100 μm x 100 μm

3.12.2 *Effect of Initial Micropart Location – d*

The variation in the distance travelled as function of the initial micropart location from the actuator for both Gaussian and sinusoidal surface deformations for two different values of surface bonding roughness, σ_n, 20 nm and 30 nm, is shown in Figure 3.19 (a~d).

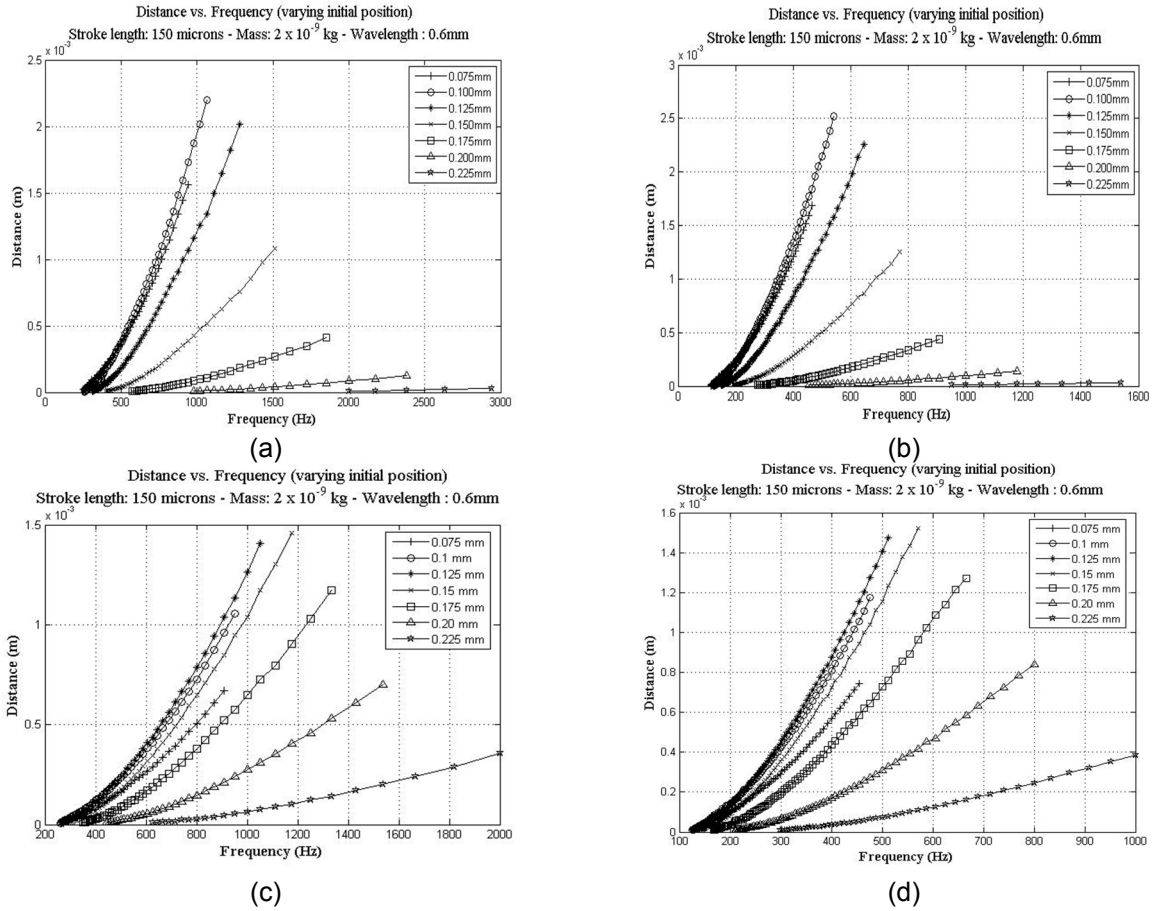

Figure 3.19: Distance travelled by the micropart as function of initial location from center of deformation with $\Delta\gamma$= 1 J/m2 and H= 1000 MPa, (a) σ_n= 20 nm, deformation gaussian (b) σ_n= 30 nm, deformation gaussian (c) σ_n= 20 nm, deformation sinusoidal (d) σ_n= 30 nm, deformation sinusoidal

The initial position of the micropart not only affects the net displacement but the range of feasible frequencies as well. The larger the initial distance of the micropart from the center of the actuator, the larger the range of feasible frequencies. At a fixed input frequency, the micropart displacement first increases, and then starts decreasing as the initial distance from the center of deformation increases. The upper most line in Figure 3.19 (a~d) represents the location corresponding to maximum displacement for the same frequency input.

It is observed that for both deformation profiles, the highest displacement corresponds to the distance of initial location of the micropart relative to the center of deformation or actuator location slightly less than a quarter of the deformation wavelength (WL); for example for a wavelength of 0.6 mm the

location with the largest displacement for the same frequency input is 0.125 mm which is slightly less than ¼ of the deformation wavelength. The effects of changes in the displacement and feasible frequency range are more prominent for the Gaussian surface deformation profile (Figure 3.19(a, b)) compared to the sinusoidal profile (Figure 3.19(c, d)).

3.12.3 *Effect of Input Deformation Wavelength - WL*

The change of distance travelled as function of surface deformation wavelength is presented in Figure 3.20 when the relative location of the micropart is kept constant at 0.25 of the wavelength from the center of the deformation (variable *d* in Figure 3.1(b)), and when the micropart is at an absolute initial distance independent of the wavelength deformation in Figure 3.21. For a constant value of relative initial distance, increasing the input wavelength for the same stroke length and deformation profile decreases the distance travelled while having negligible effect on the range of feasible frequencies according to Figure 3.20(a, b). For the same input parameters, the sinusoidal deformation profile produces larger distance travelled, has a smaller frequency feasible range and smaller values for the minimum and maximum frequencies as observed in Figure 3.20(a) and Figure 3.20(b).

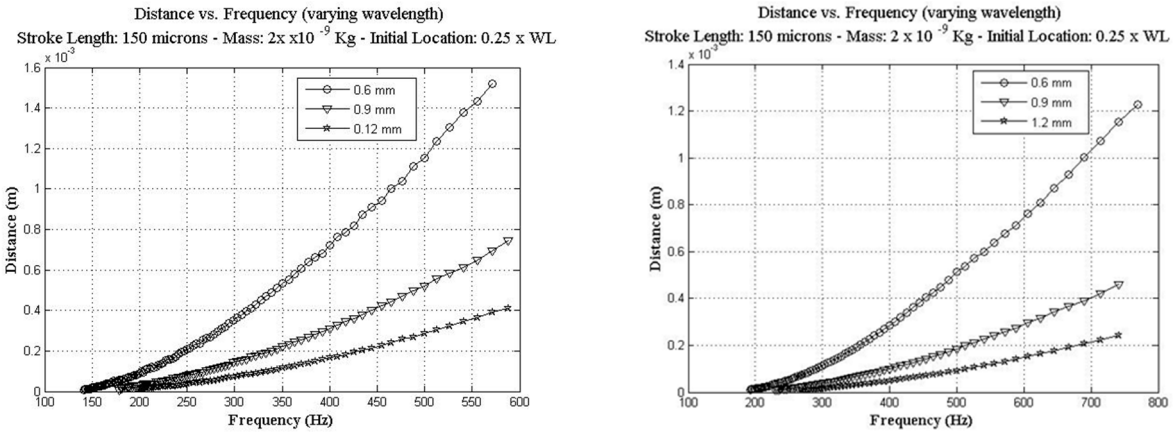

(a) (b)

Figure 3.20: Distance travelled as function of wavelength of input deformation profile. Relative initial position is constant with $\Delta\gamma$= 1 J/m2 H= 1000 MPa, σ_n= 30 nm, (a) deformation sinusoidal (b) deformation gaussian

If the absolute value of the initial location of the micropart is fixed relative to the actuator and not a function of deformation wavelength, the change of the wavelength affects the distance travelled as

shown in Figure 3.21. For a fixed stroke length, the range of feasible frequency increases by decreasing the wavelength. This is due to the larger deformed surface slope attained for smaller wavelengths. The larger the slope, the smaller the component of the inertial force perpendicular to the surface which causes the micropart detachment to be delayed as the frequency increases. The net displacement of the micropart at a fixed value of frequency is largest if the initial location is closer to ¼ of the length of deformation as represented by the upper most line in each graph of Figure 3.21.

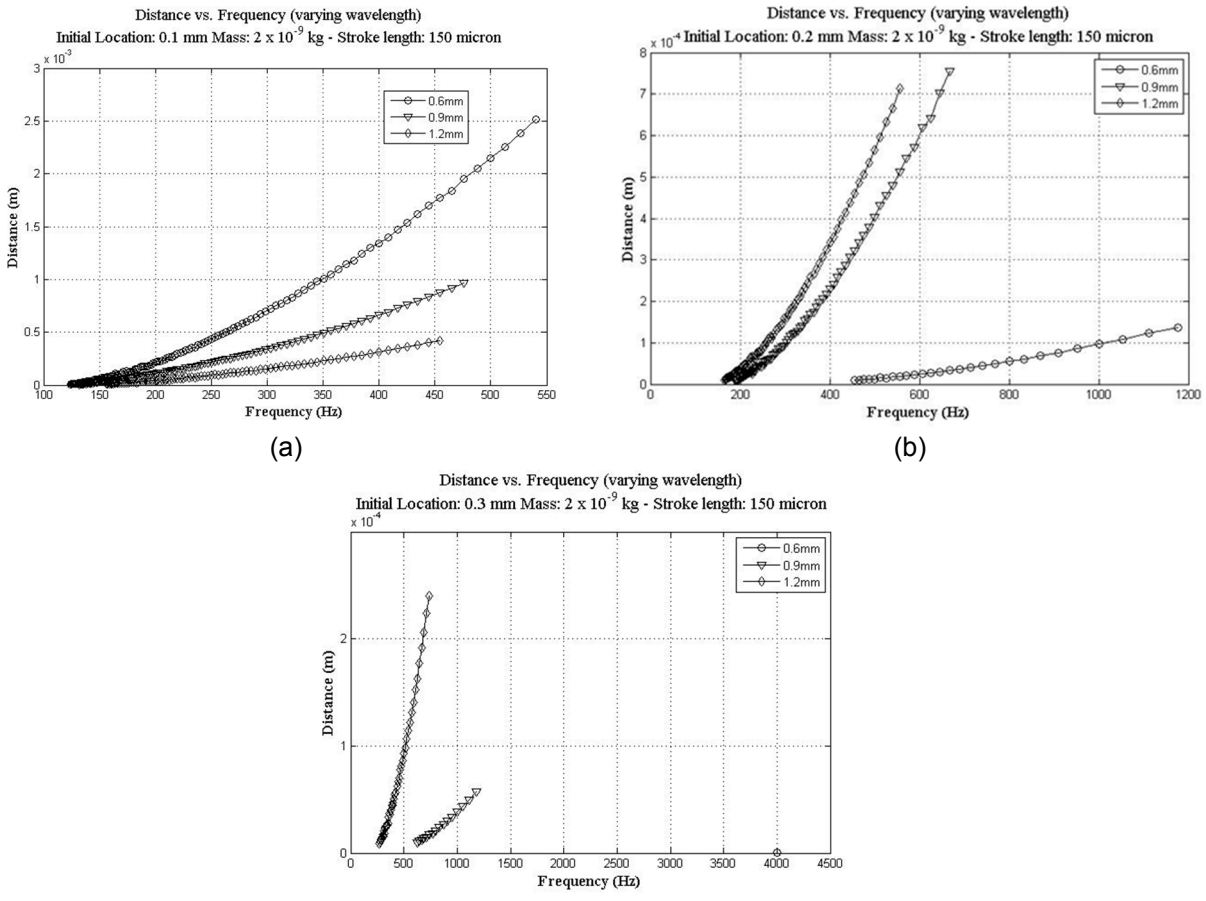

Figure 3.21: Distance travelled as function of wavelength of input deformation profile.
Absolute initial location is fixed with Gaussian deformation and $\Delta\gamma$ = 1 J/m2, H= 1000 MPa, σ_n= 30 nm.
Initial location (a) 0.1 mm (b) 0.2 mm (c) 0.3 mm

3.12.4 *Effect of Micropart Mass - m*

The mass of the micropart is a measure of the generated inertia force due to the acceleration and deceleration of the actuator and is the only driving force for micropart translocation along the deformed

surface with the friction force as the only opposing force. The acceleration and deceleration are functions of the stroke length, frequency and actuator displacement profile. The effect of the micropart mass on the distance travelled is studied considering that the contact area of the micropart remains constant such that the mass is a function of the thickness of the micropart. The effect of the mass is analyzed for two initial locations for both deformation profiles for a single wavelength. The mass analysis indicates that for both deformation profiles, as the mass decreases the range of feasible frequencies increases substantially while the distance travelled is substantially reduced for the same actuator frequency as presented in Figure 3.22(a~d). A larger micropart mass means that a larger equivalent inertia force will be generated and once decomposed will yield larger forces along and perpendicular to the surface. For the fixed value of system parameters, a larger inertia force perpendicular (with a constant force of attraction) to the surface decreases the range of operating frequency while a higher inertia along the surface (with the same friction force) increases the resultant distance travelled.

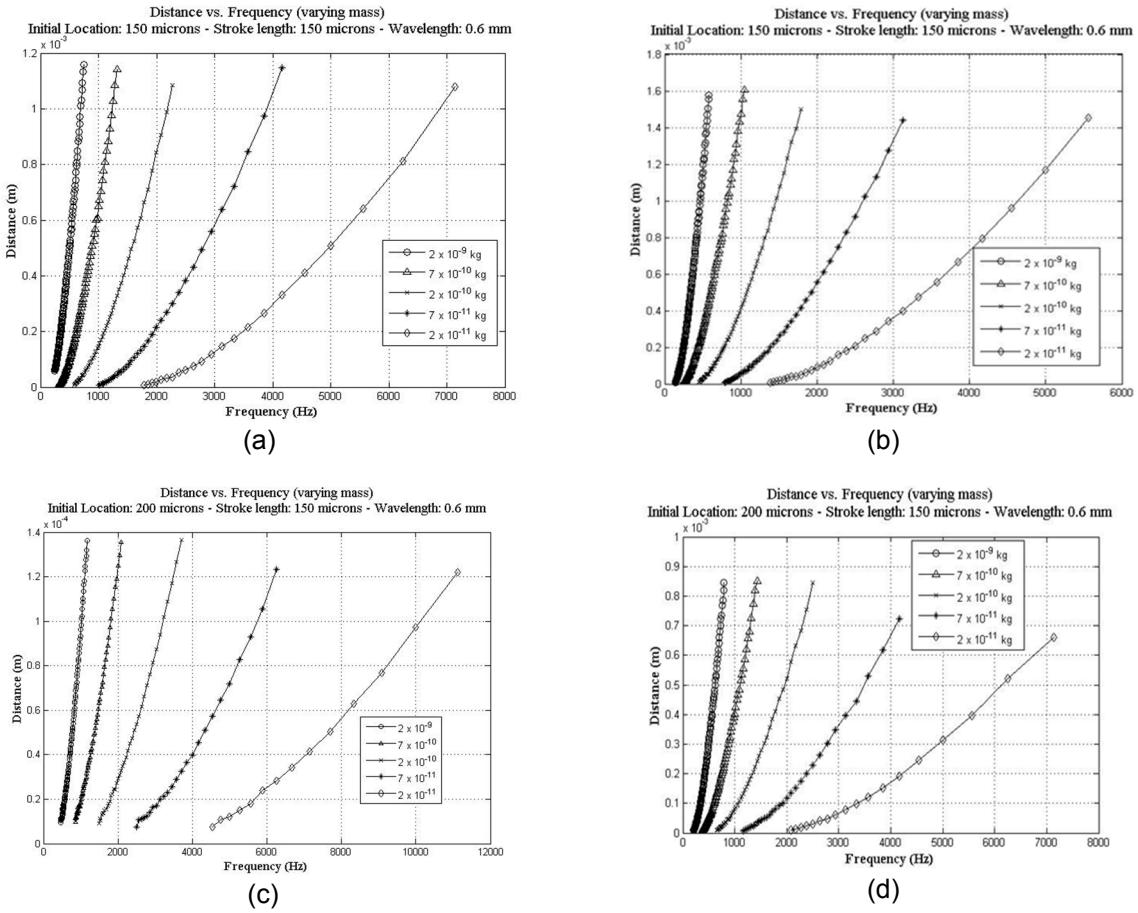

Figure 3.22: Variation in distance travelled as function of micropart mass and initial location $\Delta\gamma$= 1 J/m2, H= 1000 MPa, σ_n = 30nm, (a, c) deformation gaussian, (b, d) deformation sinusoidal

The effect of micropart mass on distance travelled and feasible frequency range is very similar between the sinusoidal and Gaussian surface deformation profiles. The value of maximum distance travelled remains almost the same with the variation of mass while the range of feasible frequencies significantly reduces and shifts towards lower-frequencies with an increase of micropart mass.

3.12.5 *Effect of Surface Deformation Profile – Gaussian - Sinusoidal*

The effect of the deformation profile, Gaussian and sinusoidal, for the same initial micropart location and actuator stroke length characteristics is presented in Figure 3.23. It is observed that for both

stroke values the sinusoidal profile generates larger displacements for the same frequency and also causes micropart translocation at lower frequencies as compared to the Gaussian profile. The feasible frequency range for the sinusoidal profile is small and shifted towards the lower frequency compared with the Gaussian profile.

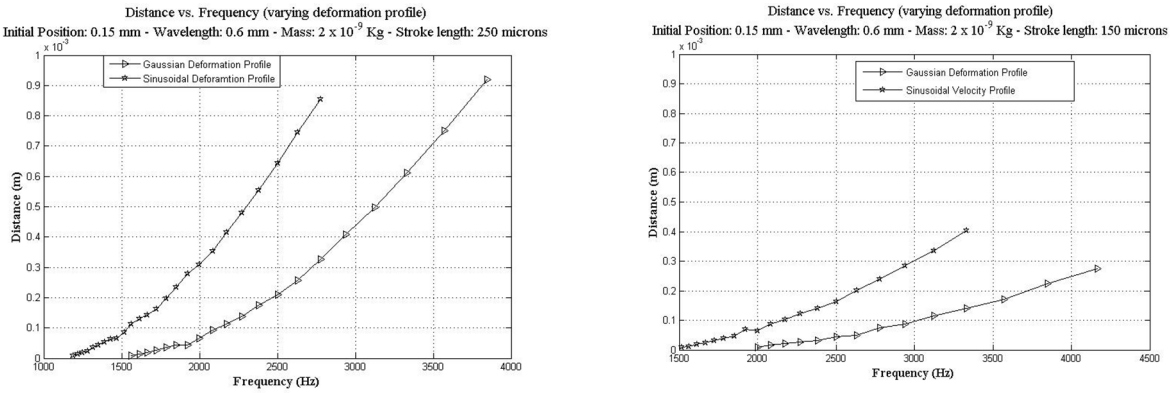

(a) (b)

Figure 3.23: Variation in distance travelled by change in surface deformation (gaussian and sinusoidal) with Δγ= 2 J/m2, H= 1000 MPa, σn= 20 nm, stroke length (a) 250 μm and (b) 150 μm

3.12.6 *Effect of Surface Roughness - σ_n*

The effect of surface roughness on the distance travelled is analyzed by considering both deformation profiles and three surface roughness values as shown in Figure 3.24. Note that, it is assumed that the surface deformation does not change the surface roughness and the values presented in the figures represent the standard deviation of the surface profile.

An increase in the roughness increases the mean distance between the two surfaces which results into a decrease in the force of attraction between the surfaces and reduced percentage of asperities in contact resulting in a reduced friction force. A smaller force of attraction is an indication that a smaller number of asperities would be compressed. The shear load will then be only supported by the elastic and partial plastically deformed asperities, therefore, without any other externally applied load, the friction force is reduced with an increase in surface roughness which results into early (at lower frequency) motion initiation. However, a larger attraction force is desirable to keep the micropart in contact with the surface and prevent it from detaching.

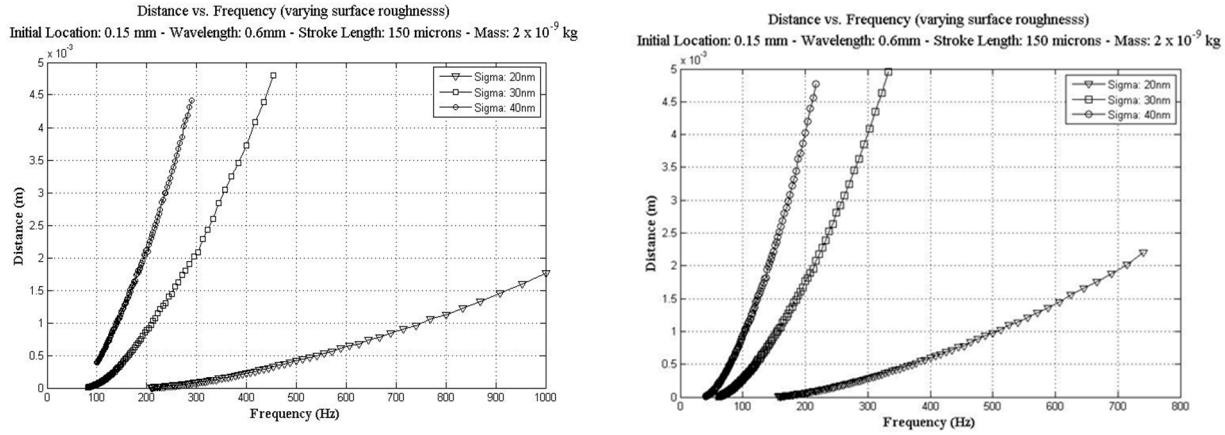

(a) (b)

Figure 3.24: Distance travelled with the change in surface roughness with Δγ= 0.5 J/m2, H= 1000 MPa and stroke length 150 μm (a) gaussian deformation (b) sinusoidal deformation

As a result of the compromise of these contradicting parameters, an increased roughness resulting into a decrease in the attraction force not only shifts the range of feasible frequencies towards the lower frequency values but also reduces the range of feasible operational frequencies. Therefore, at the microscale where the weight of the micropart is negligible compared with the surface attraction force, for a given input frequency a reduced friction force will yield a higher micropart displacement for a rougher as compared to a smoother surface as shown in Figure 3.24. The larger surface roughness causes the feasible frequency range to shift towards smaller frequency values.

3.12.7 *Effect of Surface Bonding Energy – Δγ*

The distance travelled due to surface bonding energy changes is analyzed and is presented as function of input frequencies for both Gaussian and sinusoidal profiles in Figure 3.25. The surface bonding energy is defined as the difference of the energy of the two independent surfaces and the energy when these surfaces are in contact. The distance travelled by the micropart varies sharply as function of the surface bonding energy.

At the microscale (where the weight of the micropart is negligible) a higher bonding energy value generates a larger attraction force resulting into a reduced equilibrium mean separation distance between the surfaces when compared with the same roughness but smaller bonding energy. The smaller mean

separation distance results into higher friction force. A higher attraction force results in an increase in the range of feasible frequencies but contrary to the surface roughness effect, even at the highest value of feasible frequency, the distance travelled by the micropart with a higher surface energy is less than the maximum displacement estimated by lower bonding energy. If the bonding energy decreases, even though it reduces the feasible frequency range because of smaller attraction forces, it causes an increase in the distance travelled.

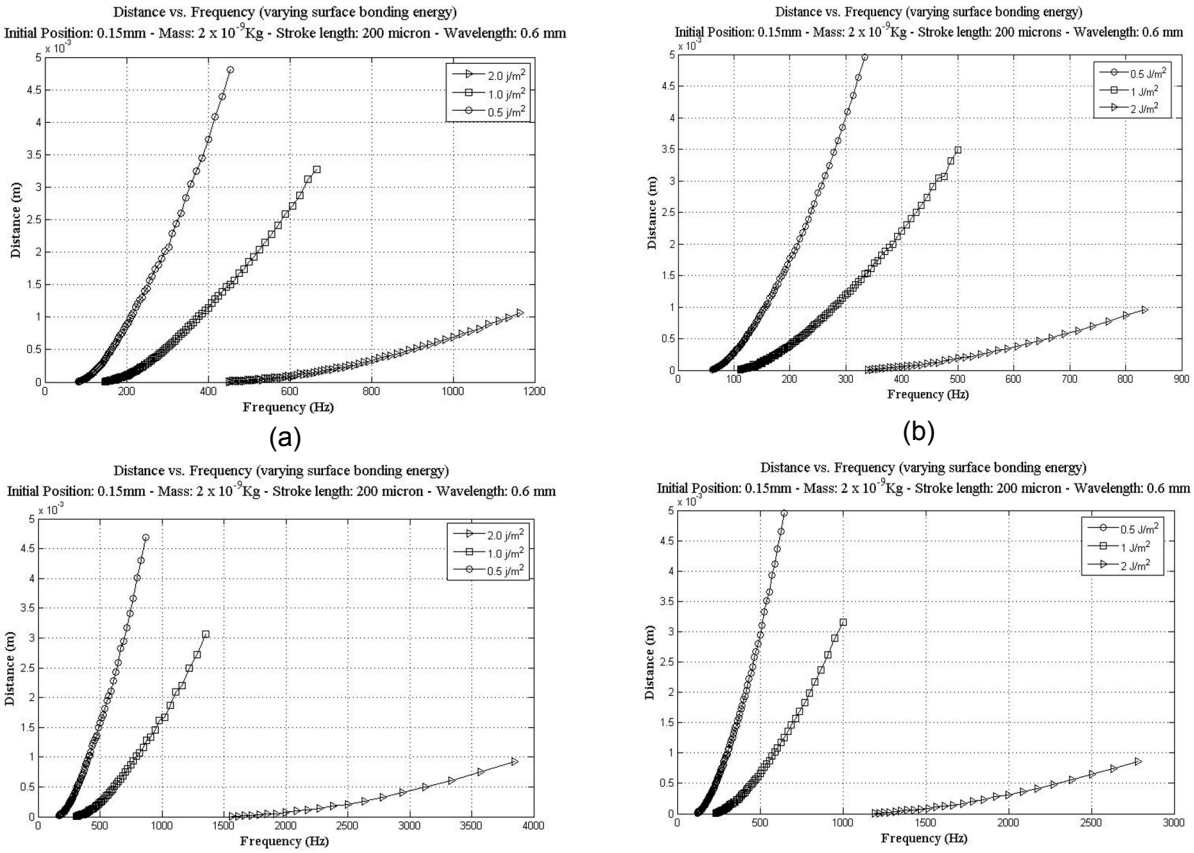

Figure 3.25: Variation of distance travelled with the change of bonding energy between two surfaces. H= 1000 MPa; σ_n= 30nm (a) deformation gaussian, (b) deformation sinusoidal; σ_n = 20nm (c) deformation gaussian (d) deformation sinusoidal

3.12.8 *Effect of Actuator Stroke Length - h_f*

The effect of actuator stroke length on the distance travelled is examined as function of the input frequency and for two surface bonding energy values for both the Gaussian and sinusoidal deformation profiles with the results shown in Figure 3.26. For a constant value of actuator frequency, a larger

actuator stroke length increases the acceleration and deceleration rates thus generating higher inertia forces. In addition, for a fixed wavelength a larger stroke length will result in an increase in the deformation slope of the surface thus increasing the imparted acceleration and inertia force along the surface. A larger inertia along the surface will result in a larger travelled distance since inertia is the only driving force in the system. It is observed that, for both deformation profiles, the distance travelled by the micropart increases as the stroke length increases. However, the distance travelled for the sinusoidal profile is larger than the Gaussian one when all other parameters remain the same and especially for the same frequency values. Comparing the effect of the actuator stroke on the feasible frequency range, the larger the stroke the smaller will be the effective frequency range before the micropart detaches from the surface. In addition, for the sinusoidal profile, the effective frequency range is reduced and shifted towards lower frequencies (Figure 3.26(c/d)) as compared to the Gaussian profile (Figure 3.26(a/b) frequency shift for the same stroke. Also, it is observed that the smaller stroke yields much smaller displacements indicating that a smaller stroke could be advantageously employed for finer positioning requirements.

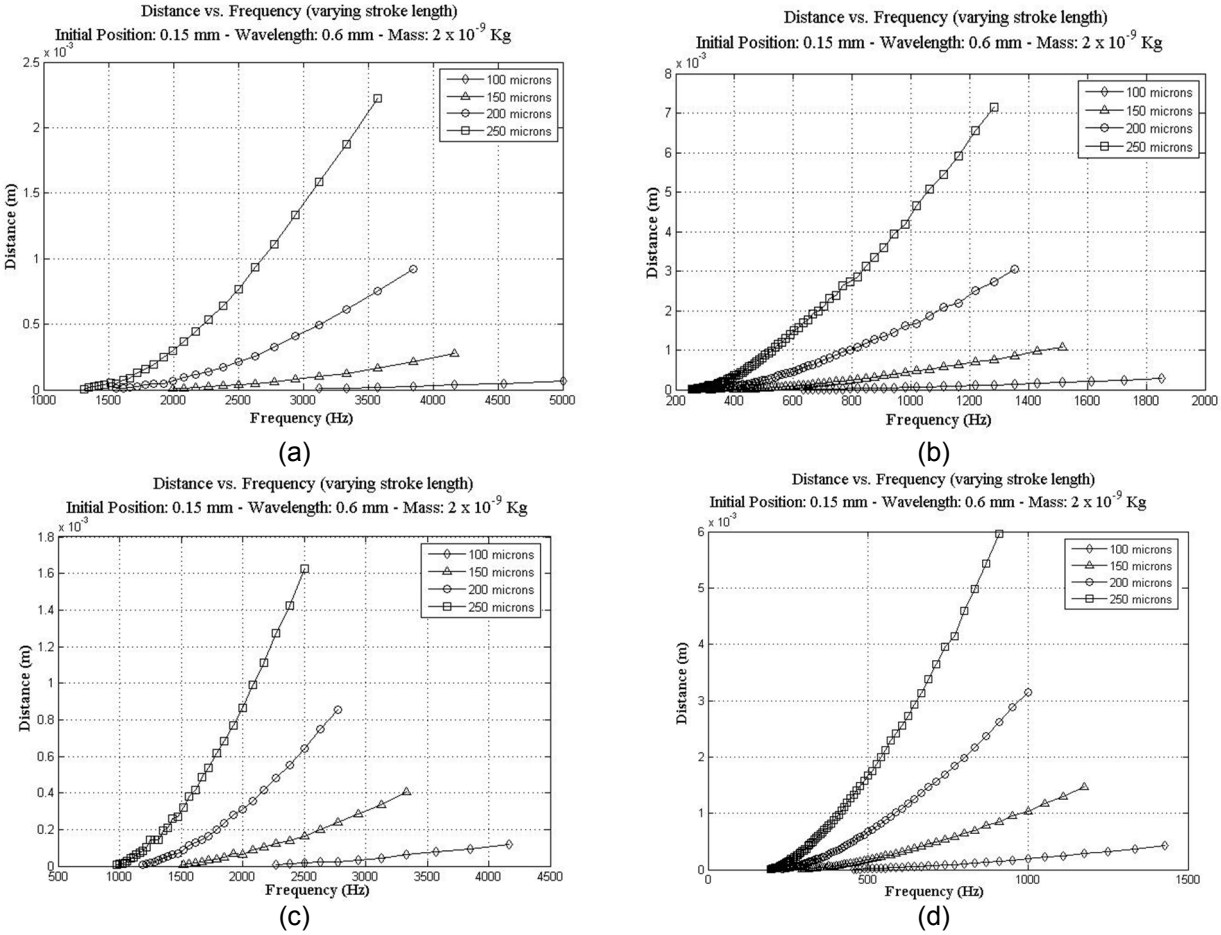

Figure 3.26: Variation of distance travelled with change of stroke length, H=1000 MPa, σn=20nm, deformation Gaussian (a) Δγ=2 J/m^2 (b) Δγ=1 J/m^2; deformation sinusoidal (c) Δγ=2 J/m^2 (d) Δγ=1 J/m^2

3.13 Statistical Analysis

The simulation results presented in Figure 3.19 through Figure 3.26 show the distance travelled by the micropart as function of the controlled and physical parameters and could be employed in defining process parameters for controlled micromanipulation. In addition to the presented discussion, the results of the Gaussian deformation profile were also statistically analyzed in an effort to assess the relative effect of each input parameter on the system output in the domain examined. Linear regression analysis is conducted to fulfill this purpose. The Box-Cox transformation is applied to the dependent variable to make the residuals of the regression more homoscedastic and closer to normal distribution as assumed. The data is fitted to the following model

$$
\begin{aligned}
&BoxCox(Distance) \\
&= \alpha + \beta_{e1} I(E = 1) + \beta_{e2} I(E = 2) + \beta_{r1} I(RGH = 3 \times 10^{-8}) \\
&+ \beta_{r2} I(RGH = 4 \times 10^{-8}) + \beta_{s1} I(ST = 1.5 \times 10^{-4}) + \beta_{s2} I(ST = 2 \times 10^{-4}) \\
&+ \beta_{s3} I(ST = 2.5 \times 10^{-4}) + \beta_m I(MS = 2 \times 10^{-9}) + \beta_{wl} I(WL = 1.2 \times 10^{-3}) \\
&+ \beta_{p1} I(PL = .25) + \beta_{p2} I(PL = .33) + \beta_f log\ + \varepsilon
\end{aligned}
\tag{3-48}
$$

where $BoxCox(Distance) = \begin{cases} \frac{y^{\lambda}-1}{\lambda} & if\ \lambda > 0 \\ log(y) & if\ \lambda = 0 \end{cases}$ and λ is a transformation parameter to be estimated.

The residual ε follows the normal distribution with mean *0* and constant variance σ^2. The I(.) is an indicator variable (=1 if the condition within the parenthesis holds, =0 otherwise). The independent variables considered in the model include Surface Bonding Energy (E), Roughness (RGH), Stroke (ST), Mass (MS), Wavelength (WL), Initial Particle Location (PL), and log-transformed frequency (logω). The corresponding reference levels are E = 0.5 J/m^2, RGH = $2 \times 10^{-8}\ nm$, ST = $1 \times 10^{-4}\ m$, MS = $2 \times 10^{-10}\ Kg$, WL = $6 \times 10^{-4}\ m$, and PL = $0.167\ m$ respectively.

The data analysis is performed in two stages. At the first stage, the transformation parameter λ is estimated and $\hat{\lambda} = 0$, which corresponds to the logarithm transformation on the dependent variable. At the second stage, the estimate $\hat{\lambda} = 0$ is treated as known, and the regular linear regression analysis is performed to evaluate the statistical significance of each input variable on the distance travelled.

The linear regression analysis results are shown in Table 3.4. About 91% of variability on the dependent variable is accounted for by the considered input variables (R-square = 0.91). The coefficients in the second column of Table 3.4 represent the relative variation in the system output with the change of that particular parameter. A positive sign represents an increase in the output while a negative sign represents a decrease, for example, the distance travelled decreases as the wavelength increases. It is observed from the table that the stroke length at 250 μm is the most influential parameter with the largest estimated effect (-0.87x10^{-4}) while the surface energy at 2 J/m^2, compared to other levels of the

parameters within the specified domain, is the second most significant parameter estimated at $-0.81x10^{-4}$. For the remaining parameters (stroke length, surface roughness and particle mass) the output of the system increases with an increase in their respective values. The increase in stroke length will increase the distance travelled but at a slower increasing rate even though in the specified range is the most significant from the controlled input parameters for increasing the system output.

Table 3.4: Results from linear regression analysis

	Estimate($\times10^{-4}$)	Std. Error($\times10^{-6}$)	t value	p-value
Surface Bonding Energy(E) (J/m^2)				
.5	0.00			
1	-0.28	1.63	-174.1	<2e-16
2	-0.81	2.71	-300.2	<2e-16
Roughness (RGH) (m)				
2.00×10^{-8}	0.00			
3.00×10^{-8}	0.37	2.19	168.8	<2e-16
4.00×10^{-8}	0.64	2.60	247.2	<2e-16
Stroke (ST) (m)				
1.00×10^{-4}	0.00			
1.50×10^{-4}	0.31	2.31	133.0	<2e-16
2.00×10^{-4}	0.53	2.33	227.0	<2e-16
2.50×10^{-4}	0.70	2.40	291.2	<2e-16
Mass (MS) (kg)				
2×10^{-10}	0.00			
20×10^{-10}	0.59	2.22	265.9	<2e-16
Wavelength (WL) (m)				
6×10^{-4}	0.0			
12×10^{-4}	-0.25	1.35	-183.2	<2e-16
Initial Particle Location (PL) (m)				
0.17	0.00			
0.25	-0.30	1.54	-193.4	<2e-16
0.33	-0.87	2.59	-335.5	<2e-16
log(x.freq) [freq:ω]	0.50	1.63	309.2	<2e-16

3.14 Conclusions

In this chapter, the motion dynamics of a micropart in a dry nonlubricated environment based on the controlled deformation of an active surface have been investigated considering microscale forces (Van der Waal's) and the deformation of the surface asperities. The friction coefficient is dynamically evaluated considering the dynamic nature of the microphenomena and their interaction and effects according to the Kogut-Etsion friction model. The model was then extended and applied in analyzing the feasibility of micropart motion on a surface undergoing a controlled deformation profile and predicting the distance traveled by the micropart. In addition, sensitivity of the system output for various system and input parameters is analyzed to estimate the more influential parameters to be considered in the system design

The parameters considered in the mathematical model and analysis include the micropart mass, size, and material, the relative roughness between the micropart and surface, the surface material properties, the surface deformation profile, and the input actuator frequency and stroke. The simulation results indicate that predictable micropart motion could be achieved only within a range of input actuator frequencies (lower and upper bounds) that depend on the values of the input parameters. At frequencies less than the lower bound no significant motion was observed while at frequencies higher than the upper bound the micropart detaches from the surface.

The effect of variation in input parameters on the system output is estimated in the sensitivity analysis. The results of simulated system output at a range of input parameters are used to carryout qualitative and quantitative analysis. The parameters considered in this study relate to properties associated with the micropart, the substrate surface, and the actuator, mass of micropart, frequency of actuation, wavelength (length of deformation), length of stroke of actuator, contour of surface deformation profile, difference of surface energy of the two separate surfaces and the two surfaces combined (bonding energy), initial position of micropart with respect to actuator and surface roughness. The range of the input parameters was defined based on discussions in the literature or based on results obtained from previous analyses by the authors. The simulation results were analyzed by first examining the

distance travelled as function of the actuator input frequency for various combinations of the input parameters. A range of feasible input frequencies was identified as function of the parameters with the minimum frequency being the frequency at which no significant micropart motion takes place (<10 μm) and the maximum frequency being the frequency at which the micropart detaches from the deformed surface. Subsequently, the simulation results were used in a statistical approach to assess qualitatively the sensitivity of the output to the parameters examined and their domain. The statistical analysis indicated that the most influential parameters are surface bonding energy, surface roughness, and input stroke length.

The understanding of the dynamic microphenomena and their effects due to the interaction of the micropart motion with the substrate caused by the controlled deformation in a dry non-lubricated environment paves the way towards controlled micropart translocation and manipulation employing a flexible surface for microassembly or for processes requiring controlled micropart handling for heterogeneous microdevice mass production.

CHAPTER 4

MICROPART MOTION ON A MICROCONVEYOR DUE TO AN ARRAY OF MICROACTUATORS

4.1 Introduction

The highly nonlinear motion dynamics of a micropart translocating on a surface due to controlled surface deformation through a single actuator considering micro-scale forces have been introduced and motion feasibility demonstrated in Chapter 3. In this chapter, the concept of flexible surface deformation will be extended from a single actuator to an array of actuators in order to realize a one dimensional microconveyor system. The analysis is extended to the motion of the micropart interacting with a multi-actuator system. Compared with a single actuator operation, a microconveyor system requires additional parameters to be identified, included and augmenting the existing motion model in order to control the final location of a micropart. These parameters are introduced, the micropart motion is discussed and final distance travelled is estimated assuming various initial conditions for two actuators.

The previous chapter focused on the mathematical modeling of the motion dynamics of a micropart on a flexible surface under controlled deformation generated by a single actuator and the resulting translocation distance. The results showed that the distance covered by a micropart under the influence of a single actuator is bounded by the fact that the input frequency is bounded. At a frequency higher than the upper limit of the frequency range, the micropart detaches from the surface. In order to translocate the micropart for a distance larger than the capability of a single actuator, multiple actuators cascaded in the form of a linear array must be employed. While the micropart is moving, it will interact with the downstream actuators and will either continue to move or come to rest. With the introduction of multiple actuators in the form of a sequential array, in addition to the parameters defined for single actuator system, the system requires the definition of additional variables. This chapter will introduce the

new translocation system, the additional parameters to be considered and their effects on the system output, and the interaction effects of two consecutive actuators.

4.2 Array of Actuators: Additional parameters and mathematical modeling

A schematic representation of the concept of array of actuators is shown in Figure 4.1. Actuators spaced at appropriate distance can translocate the micropart to a distance larger than the capability of a single actuator. Micropart energized by one actuator will interact with the downstream actuators to acquire or release energy. The nature of interaction of micropart with the downstream actuators depends upon the system variables and control parameters.

When multiple actuators are sequentially arranged the full mathematical representation of the new system requires additional parameters, namely spacing between consecutive actuators, input frequency and motion profile, and time delay between the actuation of consecutive actuators.

The spacing between two consecutive actuators can be different for each set of actuators with the total number of additional parameters equal to n_a-*1* where n_a is the total number of actuators. A variable spacing of actuators increases the complexity of the system substantially. However, in actual implementation, the actuator spacing will depend on the microconveyor application. Therefore, in order to reduce the complexity for the initial analysis and feasibility study, the spacing between consecutive actuators is assumed to be constant.

The single actuator analysis has only one input actuation frequency. In the case of multiple actuators, each actuator could have its own actuation frequency. In order to simplify the analysis, all the actuators are assumed to operate at the same frequency. In addition to the input frequency, all the actuators are assumed to have the same motion profile with the same polynomial characteristics as those for a single actuator analysis.

The time delay is defined as the time span between the firing of two consecutive actuators. The time delay is assumed to be greater than the time period of the actuator motion. Therefore, the second actuator can only be fired only after the first actuator reaches its fully retracted position. This avoids determining the complexity of surface deformation because of multiple actuators firing or actuated at the

same time. The time delay between the actuation of consecutive actuators could be different for each set thus increasing the complexity for the feasibility analysis. However, for initial analysis and feasibility study, the time delay between the actuators is assumed to be constant.

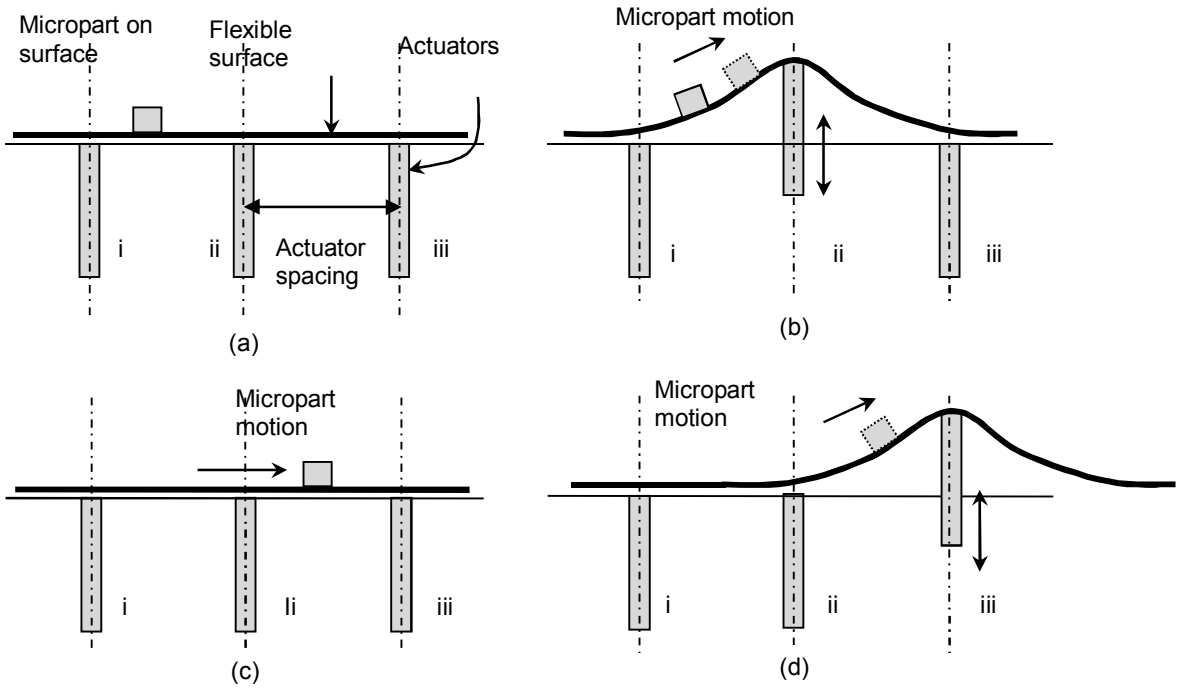

Figure 4.1: Schematic of linearly cascaded actuators (a) three actuators with micropart resting on the flexible surface (b) actuator "ii" deforms the surface causing the micropart to start translating, (c) actuator ii retracts and the micropart either comes to rest or keeps on translating, (d) actuator iii starts deformation after complete retraction of "ii"

The response of the multiactuator system is not a simple combination of the responses from individual actuators. The previous chapter analyzed the micropart motion from a single actuator with zero initial velocity. In the case of multiple actuators, the micropart will be engaged by a subsequent actuator either when it comes to rest or while is translating thus with non-zero but finite initial velocity. The value of the engaging initial velocity for a subsequent actuator is a function of the input frequency, length of stroke, initial location of micropart, and the newly introduced parameters, the spacing between the actuators and the time delay between the firing of two consecutive actuators.

The time delay between the firing of two consecutive actuators and the spacing between them will determine the initial relative location of the micropart with respect to the subsequent actuator and the value of initial velocity. Similar to the analysis for a single actuator, due to the nonlinearity and non-differentiability of the motion modeling equations, the effects of initial velocity on the distance travelled by the micropart (system output) cannot be evaluated in closed form. Therefore numerical simulation is used to estimate the influence of the new parameters on the distance travelled.

It has been presented that for a single actuator, the distance travelled increases with the increase of the input frequency, a longer actuator stroke, an increased surface roughness and smaller wavelength. With the actuators operating in sequence, the system performance and output is not expected to be the extrapolation of a single actuator behavior or the linear sum of the performance of the individual single actuators but rather a combination of the output from the first actuator initiating the micropart motion from rest (zero initial velocity) and the output from the subsequent actuators engaging the micropart with a finite initial velocity. In this chapter, the effects of engaging velocity and position from the subsequent actuator are discussed and subsequently the overall output of the system is presented. An analysis of overall motion of the micropart with two sequential actuators is presented in order to lay the foundation towards an understanding of the functionality and performance of a microconveyor.

4.3 Array of Actuators: Effect of new parameters on micropart movement

An array of actuators is required if the micropart is to be translocated beyond the capability of a single actuator. A single actuator system is analyzed for a range of engaging (initial) velocity and position, and input frequency. These parameters are shown in Figure 4.2 where a micropart is located at an initial distance X_o from the center of the actuator while the micropart is moving with a velocity V_i towards the center as the actuator deforms the surface with a predefined motion profile and frequency f. Note that the time delay between two consecutive actuators in an array will be considered as a function of micropart engaging (initial) velocity or location.

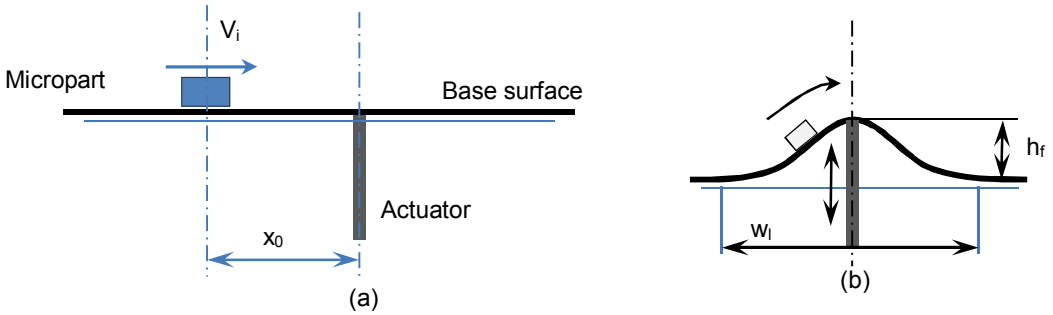

Vi= Initial Velocity of micropart before start of stroke
x0= Initial distance of micropart before start of stroke
wl = length of deformation

Figure 4.2: The conditions of simulation for effect of initial velocity. (a) The micropart has initial velocity before the beginning of stroke (b) Micropart velocity changes during deformation

4.4 Effect of engaging position as function of actuator input frequency

The effects of the engaging or initial position of the micropart relative to the actuator and the actuator input frequency on micropart displacement are analyzed. The results for two engaging positions are plotted as function of input frequency for multiple values of initial velocity as shown in Figure 4.3 and Figure 4.4.

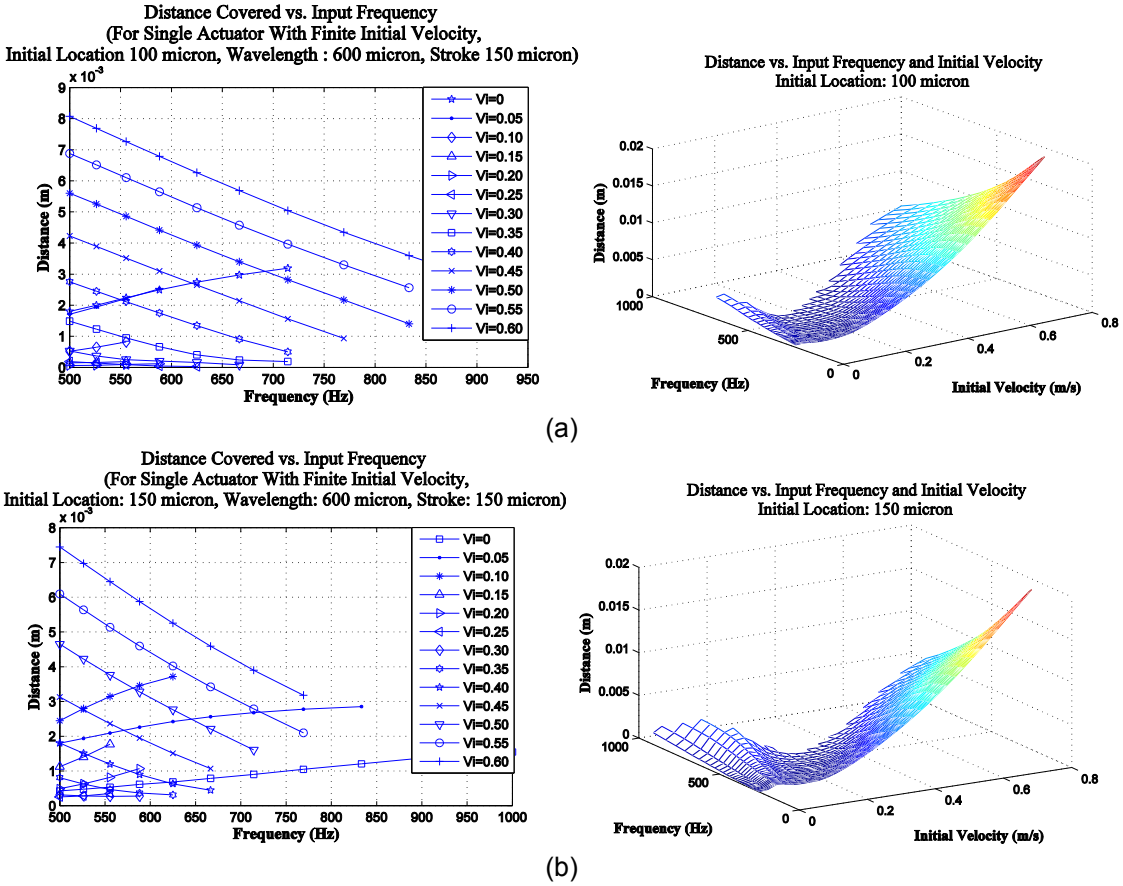

Figure 4.3: Distance travelled with variation of input frequency (a) Initial location of micropart 100 μm (b) Initial location of micropart 150 μm

The distance travelled by the micropart increases and decreases with the change of actuator frequency and the trend depends on the initial location of micropart with respect to the center of deformation by microactuator and the initial velocity. For a given initial location and for low values of initial velocity, the displacement increases with an increase of actuator frequency whereas, for higher values of initial velocity the displacement decreases with increase in input frequency. The variations are more prominently shown in Figure 4.3(b) as compared with Figure 4.3(a).

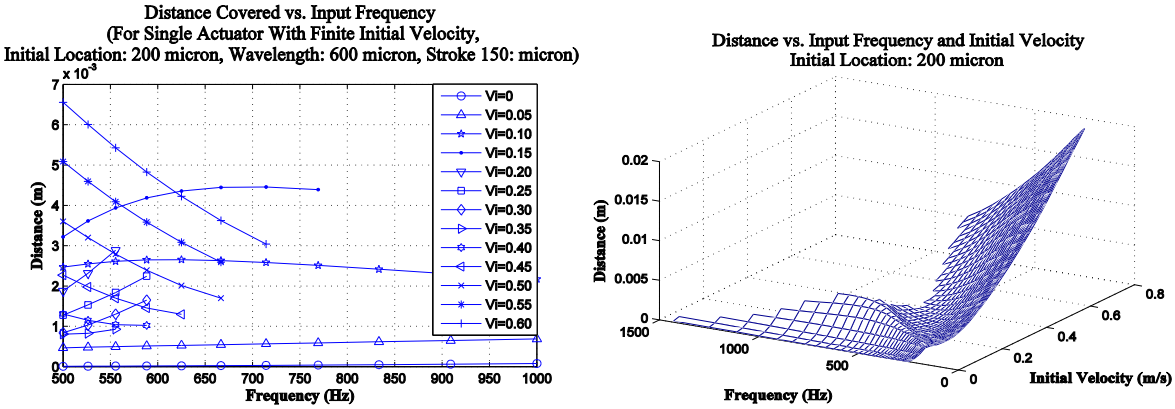

(a)

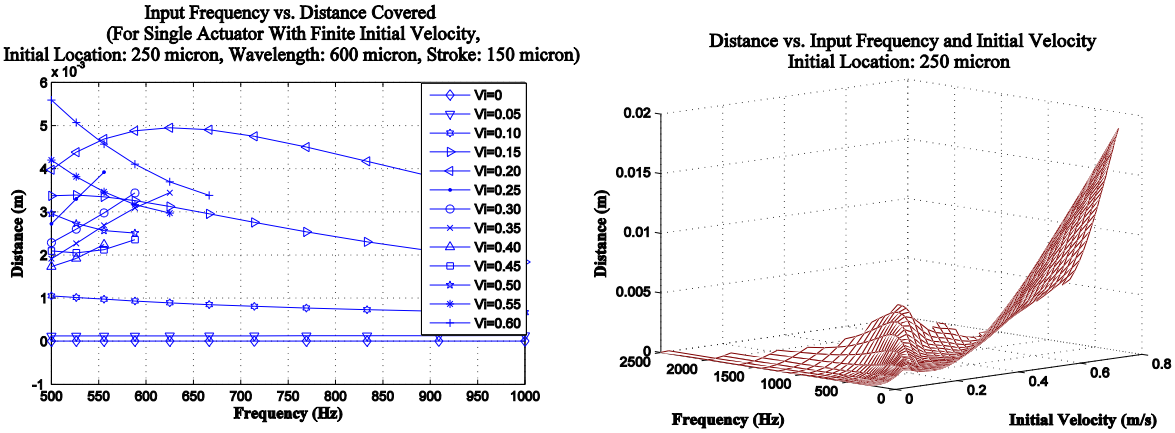

(b)

Figure 4.4: Distance travelled with variation of input frequency. (a) Initial location of micropart at 200 μm (b)Initial location of micropart at 250 μm

The threshold of initial velocity at which the change from increasing to decreasing distance travelled depends on the initial location of the micropart and length of stroke. The initial velocity threshold is 0.25 m/sec and 0.30 m/sec for initial micropart locations of 100 μm and 150 μm respectively as shown in Figure 4.3(a) and (b). If the micropart is located farther from the center of deformation, the threshold value of initial velocity increases as is further evidence from the results in Figure 4.4(a) and (b) where the threshold value of initial velocity is 0.35 m/sec and 0.40 m/sec for initial micropart locations of 100 μm and 150 μm respectively.

4.5 Effect of micropart initial velocity

On a flat surface, the distance travelled by the micropart will increase with the increase in the initial velocity as shown in Figure 4.5(a), but this behavior changes for a micropart moving on a flexible surface deformed by an actuator. At a constant finite actuator frequency, the distance travelled by a micropart may increase or decrease with an increase in micropart initial velocity. This behavior of change in distance travelled by a micropart at a constant actuator frequency is a function of the micropart initial velocity and initial location. The distance travelled by the micropart at a frequency of 500 Hz, σ_n = 20 nm, and h_f = 150 μm is shown in Figure 4.5(b). The new distance travelled increases with an increase of initial velocity up to a threshold limit of 0.15m/sec. Further increasing the initial velocity till 0.32 m/sec, the distance travelled by the micropart decreases with an increase in micropart initial velocity. Beyond 0.32 m/sec the distance again starts increasing with an increase in initial velocity.

Similar behavior is observed from the cross-section plots of Figure 4.3 and Figure 4.4. At a constant actuator frequency, the new distance travelled with the increase of initial velocity is a function of initial micropart location and actuator stroke (h_f). In Figure 4.3(a), at a constant actuator frequency, the distance travelled increases with the increase of velocity up to an initial velocity of 0.05 m/sec while this threshold changes to 0.15m/sec for Figure 4.3(b). At a velocity higher than this threshold, the distance travelled by a micropart decreases with an increase of input frequency. Similar behavior (of increase, decrease, and again increase) is also observed in Figure 4.4 which shows the distance travelled for an actuator displacement of 150 μm at an initial particle location of 200 μm and 250 μm from the center of deformation.

A comparison of Figure 4.5(a) and Figure 4.5(b) shows that the distance travelled by a micropart with low initial velocities, on a deformable surface with a single actuator stroke operating at (frequency) 500 Hz, is higher than the distance travelled by a micropart on a flat surface without any deformation (actuator not moving). Contrary, at high initial velocities, the distance travelled by the micropart is lower for a surface deformed at a frequency of 500 Hz compared to the distance on a flat surface. Therefore, at lower initial velocity the actuator seems to be increasing the system energy while at higher initial velocity

the actuator appears to be reducing the system energy. The micropart displacement at a range of initial velocities as a function of various initial positions is shown in Figure 4.5(c).

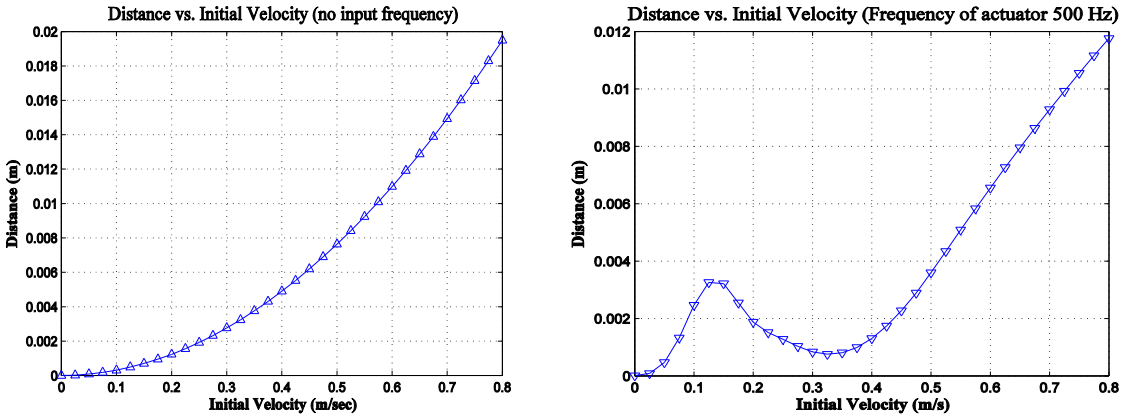

(a) (b)

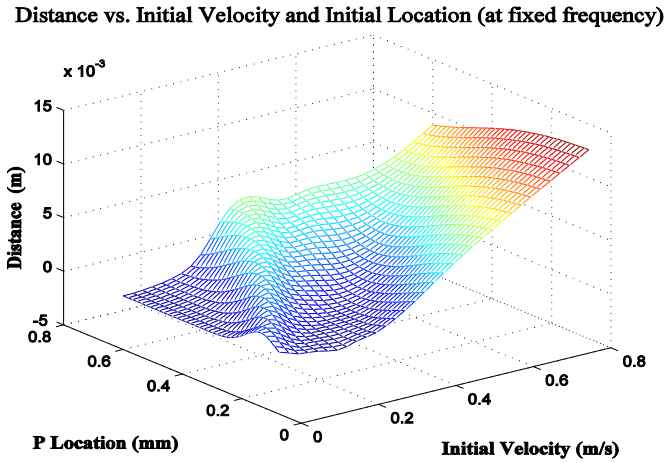

(c)

Figure 4.5: (a) Increase in the distance with the change in the input velocity with zero actuator frequency (b) Distance travelled with change of initial velocity. Stroke length: 150 μm, Input frequency: 500Hz, Wavelength: 0.6 mm (c) Distance travelled with the change of initial velocity and initial location. Frequency = 500Hz, σ_n = 20 nm, h_f = 150 μm

4.6 Feasible frequency limit

In chapter 3 the study for a single actuator indicated that there is a feasible frequency range that could cause a micropart starting from rest to translocate on the deformed surface. In the single actuator motion analysis, the initial velocity was assumed to be zero. The change of initial velocity has a direct effect on the feasible frequency range of actuators. The feasible frequency limits for the parameters considered are shown in Figure 4.3 and Figure 4.4. On the frequency axis, the end of surface shows the

limiting frequency at each value of initial micropart velocity. Any combination of input frequency and initial velocity higher than this upper bound results into separation or detachment of the micropart from the surface. The upper bound of frequency is a function of micropart location, length of stroke and initial velocity. With the increase of initial velocity the range of feasible frequencies reduces while further increasing the initial velocity the range of feasible frequencies increases. This variation in upper-bound of feasible frequency imposes constraints on the operating frequency for the cascading actuators.

4.7 Analysis and Explanation of Micropart Motion with Initial velocity

The variation in the distance travelled with the increase of frequency, feasible range of frequency and change in the distance travelled with the change of initial velocity at fixed input frequency is the result of basic mechanism of micropart movement. Comparing Figure 4.5(a) and Figure 4.5(b), in the initial phase, the distance travelled for a given input velocity is more in 4.5(b) than in 4.5(a) (up to the initial velocity of 0.15 m/sec). Whereas, beyond this limit the distance travelled reduces in 4.5(b) as compared with 4.5(a) because the actuator acts as a decelerator.

Understanding the deceleration importance requires one to explore the basic mechanism of micropart motion and possible scenarios of instantaneous micropart location and phase of actuator movement. The motion of the micropart is the result of the combined acceleration along and perpendicular to the surface. The positive acceleration perpendicular to the surface (positive direction corresponds to the direction away from the surface) generates a higher inertia force F_{β}, which is opposite to the applied acceleration on the micropart towards the surface which increases the force of friction. The acceleration parallel to the surface generates the inertia force F_{α} which causes the micropart to translocate along the surface.

The motion profile of an actuator is defined by initial and final conditions on its displacement, velocity and acceleration. Implementing the initial and final velocity and initial and final acceleration as zero, the upward stroke of the actuator consists of acceleration and deceleration regions and a downward stroke with the second set of acceleration and deceleration

When the micropart is on the surface, an upward acceleration of the surface, which corresponds to situation shown in Figure 4.6(a) and Figure 4.6(d), generates an inertia force F_α pushing the micropart away from the center of the deformation, while an upward deceleration, shown in Figure 4.6(b) and Figure 4.6(c), pulls the micropart towards the center of deformation. The amount of imparted equivalent force depends on the instantaneous value of the input acceleration/deceleration and the deformed surface slope.

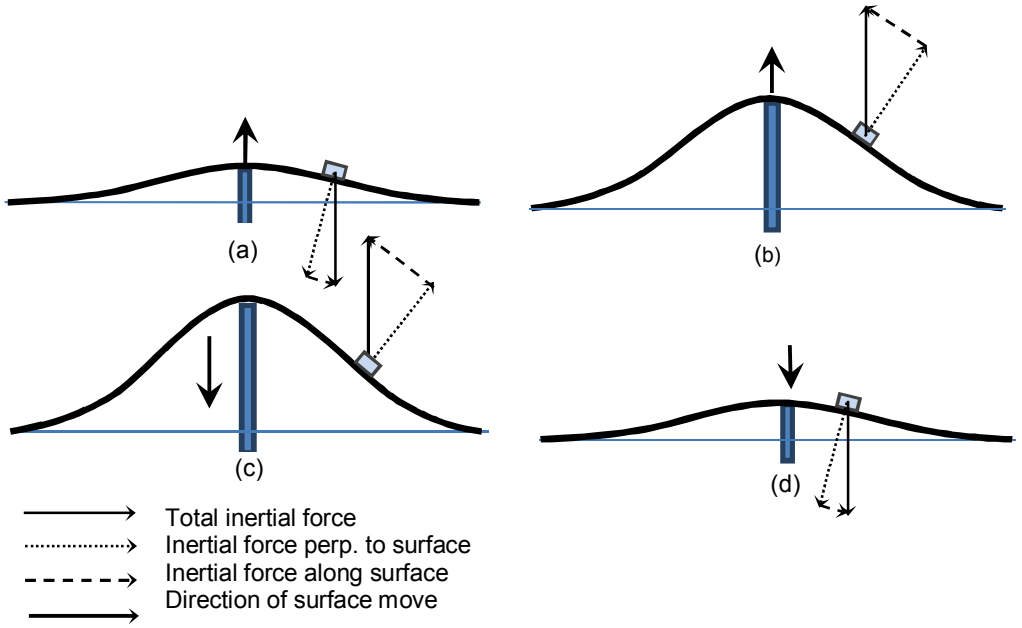

Figure 4.6: The motion of surface and forces on micropart. The arrows are qualitative representation of magnitude of inertial force on the micropart (a) Acceleration phase of upward stroke (b) Deceleration phase of upward motion (c) Acceleration phase of downward stroke (d) Deceleration phase of down stroke

The slope of the surface is small during the acceleration phase of upward stroke (Figure 4.6(a)). A micropart on the surface within the deformation range under the influence of F_α, will move away from the center of deformation as shown in Figure 4.6(a). Because of the small surface slope, the component of inertia force which causes the micropart to move along the surface is small; therefore the micropart will gain negligible velocity. In the deceleration phase of the forward stroke, the slope of the surface is larger compared to that of the acceleration phase, causing a larger inertia force on the micropart along the surface as shown in Figure 4.6(b). Under the effects of inertial force along the surface, the micropart will

move towards the center of deformation (Figure 4.6(b)). This movement will be further augmented by the downward acceleration at the commencement of the downward stroke which takes place at larger surface slopes.

The combination of the micropart engaging velocity and initial location relative to the engaging actuator will have an effect on its motion direction. If the micropart is to the right of an actuator when the upward stroke is initiated, the micropart will remain on the same side during the upward strike due to the small velocity acquired. This is due to the small slope of the deformed surface at the beginning of the upward stroke which influences the acceleration value tangential to the surface since this acceleration is the main input to initiate motion of the micropart.

If a micropart is on one side of the actuator, the micropart will remain on the same side of the actuator due to the small engaging velocity. During the downward stroke the actuator, the micropart will translate towards the actuator location (the center of surface deformation) and will not cross over the center of deformation. At this state the micropart has acquired enough energy and once the actuator is fully retracted, the micropart will continue moving away from the actuator till it expends its energy. This situation is represented by Figure 4.6(a) ~ Figure 4.6(d).

If the micropart engaging velocity is large, then during the upward actuator stroke the micropart will move towards the actuator (climb uphill) and cross over the actuator location and continue translating. However, as the actuator completes the upward and starts its downward stroke, the effect on the micropart motion will be detrimental, since the downward actuator motion will pull the micropart back towards the center of deformation. This combination of motion and downward stroke in effect slows the micropart down. This scenario is shown in Figure 4.7.

The higher the input frequency the higher will be the resultant acceleration or deceleration on the micropart motion. The frequency can be increased up to the limit where the normal component of inertia force is no more than the maximum force of attraction between the micropart and surface. At frequencies higher than this limit, the micropart will detach from the surface.

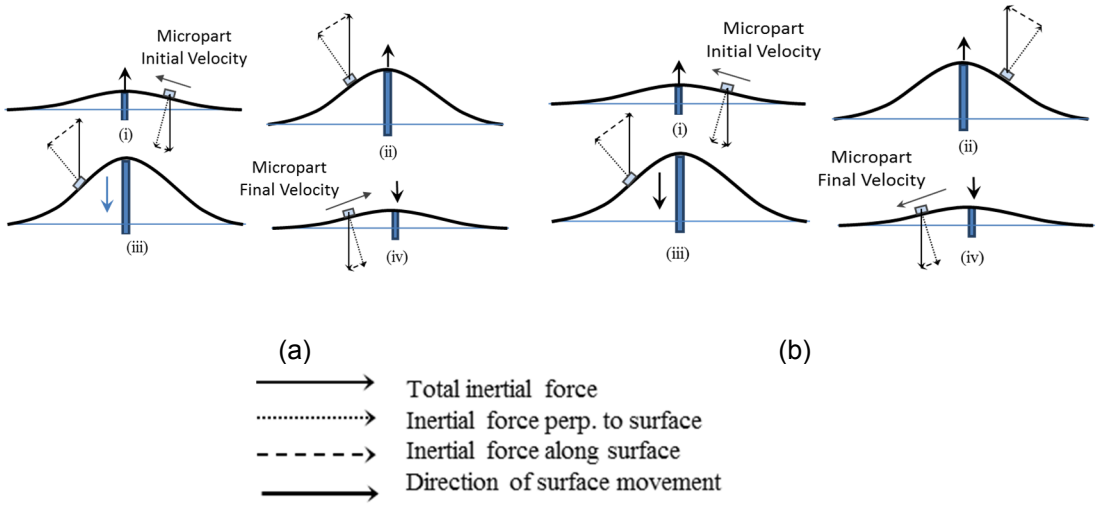

Figure 4.7: (a) Micropart reversing direction due to actuator influence (b) actuator has negligible effect on micropart overall motion

The "Velocity vs. time" plots of all three cases are shown in Figure 4.8 where region “1” is the influence of actuator while “2” represents the reduction in magnitude of velocity due to constant friction force. Figure 4.8(a) represents the acceleration of the micropart with zero initial velocity whereas 4.8(c) and 4.8(d) show the deceleration of the micropart. Figure 4.8(b) shows the null effect of the actuator on the motion of the micropart. The energy imparted to the micropart is again removed during the actuator down stroke. The micropart with zero initial velocity and with initial location on the right side of actuator is accelerated in the negative direction with a single stroke of the actuator as shown in Figure 4.8(a). Starting at the same initial location but with an initial velocity of -0.2 m/sec reduces the contribution of actuator and there is no significant change in the velocity before and after the actuation as shown in Figure 4.8(b). Further increasing the initial velocity of the micropart up to -0.3 m/sec without changing actuator input frequency, the velocity after actuator is reduced close to final value of zero. At an initial velocity of -0.4 m/s the actuator decelerates the micropart but is unable to bring it to complete stop. The particle covers some distance before coming to complete stop.

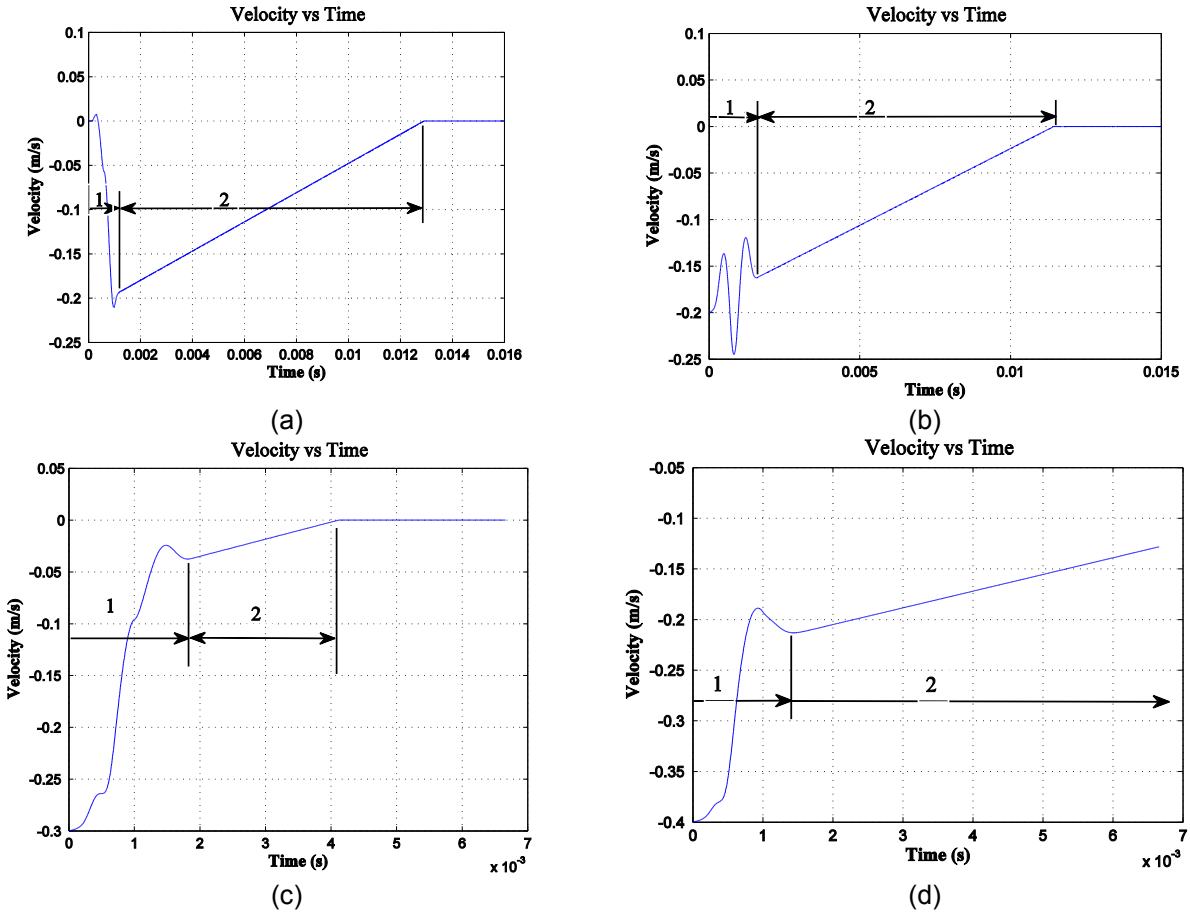

Figure 4.8: Actuator response to initial velocity of micropart. Region "1" represents the actuator contribution, while "2" is the reduction in velocity due to friction (a) Actuator increases the absolute value of micropart velocity, initial velocity is zero. (b) Actuator has negligible effect on the absolute velocity of micropart. (c) Actuator almost eliminates the velocity of micropart (d) Actuator partially reduces the absolute velocity; friction overcomes the remaining velocity of micropart.

The results of the distance travelled (system output) for one actuator and for two sequential actuators as function of input frequency are shown in Figure 4.9. Two actuators increase the distance travelled in the initial frequency range. In the middle of the frequency range the effect of a second actuator is a reduction in system output. The output starts increasing at higher values of the input frequencies. For an array of actuators, the output is not a simple addition of the output from each actuator. The combined effect of the two actuators is a nonlinear function.

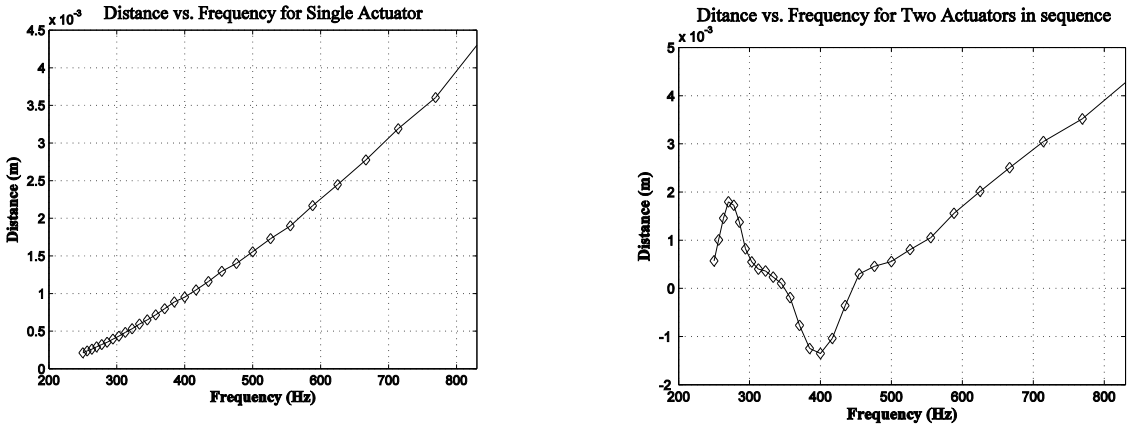

(a) (b)

Figure 4.9: Micropart displacement with a single actuator and two actuators operating at same frequency. (a) Single actuator and (b) Two actuators operating at same frequency.
Distance between actuators :0.0002 m. Delay between firing of two consecutive actuator: 0.001 sec

The capability to accelerate and/or decelerate a micropart as desired through controlled surface deformation provides the opportunity to widen the range of operating frequencies and to translocate the micropart at a higher velocity for faster processing. Due to the nonlinear interaction between the actuators, the distance covered by the micropart needs to be evaluated at each individual combination of time delay between the stroke of two consecutive actuators and the spacing between them. This necessitates the identification of a suitable optimization approach in order to identify the values of the different parameters that affect the micropart motion. However, this problem as already discussed is nonlinear and discontinuous therefore a suitable optimization method must be employed.

4.8 System Optimization

The previous sections in this chapter analyze the effects of the micropart initial velocity and initial position on the range of feasible frequencies and distance travelled by the micropart. The distance travelled by the micropart due to an array of actuators is a nonlinear combination of the contribution of individual actuators. This section discusses the feasibility of a microconveyor concept by augmenting the developed mathematical model from a single to multiple actuators in order to control the micropart translocation to reach a desired location with a predefined tolerance.

The optimum set of control parameters, within defined constraints, required to translocate the micropart to a preset location in the minimum operating time are estimated through an optimization approach. An objective function is defined to reflect time minimization and positioning within a desired tolerance along with constraints on the control and other parameters. The convergence of the objective function and evaluation of system output with the selected optimized set of control parameters indicates that an optimum set of parameters could be identified to locate the micropart at a desired location while satisfying the constraints.

4.8.1 *Optimization Methods*

In general, optimization allows one to find the best combination of values of system parameters to maximize the system desirable outcomes and minimize or eliminate the undesirable characteristics. There are many optimization methods available ranging from very simple methods to lengthy and complex ones each with its advantages and disadvantages. Selection of a particular method depends on the nature of the problem to be analyzed and other requirements. These methods can be categorized into two broad categories; derivative based and derivative free [55].

Derivative based methods are the classical methods to search for minima or maxima using the current value of the objective function and its slope. The values of the first and second derivatives are used to decide whether the desired point is reached. These optimizers include single point and multipoint approaches. These methods can handle multiple input parameters. The basic requirements for this classical technique are [55]:

- The cost function needs to be twice differentiable. For multi parameters, the function needs to be continuous for each parameter of interest.
- For single point approach, the function must have single minimum. If the cost function has multiple local extremes, the optimization is not guaranteed even with multipoint approach.

The derivative free methods are essential when the objective function is non-differentiable with respect to the design variables. Single or multipoint methods are used for this case as well. There are

many types of non-differentiable methods ranging from brute force search to the evolutionary based ones such as genetic algorithms. These methods can be used in the following situations [55]:

- When the objective function is non-differentiable or is not valid in certain region of parameter space.
- When the objective function is not represented by a single equation but it is a set of equations and logic statements.

The dynamics of the micropart motion on a flexible surface are represented by equations (3.29)~(3.31) and equations (3.35)~(3.43). These equations are not only non-differentiable but discontinuous. The behavior of the friction force alone makes the system non-differentiable and discontinuities may be introduced through stick-slip condition and the condition of micropart detachment.

Considering these issues, the derivative-free approach is selected to optimize the system performance within the given range of input parameters and associated constraints. In this research, the differential evolution method is used since it is a multi-point optimization method based on evolutionary principles. Differential evolution has been recently applied to many diverse fields with success [56-58].

4.8.2 *Problem statement and formulation*

The problem posed is to find the most suitable set of system input parameters to translocate a micropart a predefined distance and within a certain tolerance while minimizing the required time. This optimization will not only identify the most suitable set of parameters but will also verify the feasibility and functionality of the proposed microconveyor system. A general optimization problem is formulated as [59]

$$\text{Find } X = \{x_1, x_2, ..., x_n\} = \left[X^{(i)}, X^{(d)}, X^{(c)} \right] \tag{4.1}$$

to minimize $f(X)$

subject to constraints $g_j(X) \le 0 \qquad j = 1, ..., m$

subject to boundary constraints $x_i^{(L)} \le x_i \le x_i^{(U)} \qquad i = 1, ..., D$

where $X^{(i)} \in \mathbb{R}^i, \quad X^{(d)} \in \mathbb{R}^d, \quad X^{(c)} \in \mathbb{R}^c$

where $X^{(i)}, X^{(d)}$ and $X^{(c)}$ indicate feasible values of integer, discrete and continuous design variables respectively. The general optimization statement is applied to the microconveyor system with the set of design variables selected from the control parameters; minimize the error between distance travelled and desired location while minimizing the time of travel. The design variables are the input actuator frequency, actuator stroke, actuator spacing and time delay between the firing of two consecutive actuators.

Each of the four design variables or parameters can be defined for each actuator or consecutive actuator pair that is part of the microconveyor. However, in order to demonstrate the feasibility and functionality of the proposed microconveyor, the optimization problem is simplified and the search space is reduced by assuming that the microactuator control parameters are the same for each actuator. This implies that all the actuators will move with the same frequency, same actuator stroke, and that the actuator spacing and delay time between the actuators is the same. This simplification reduces the number of design variables to be considered from *(4n_a-2)* to *4* with n_a being the number of actuators; for example for a microconveyor with 5 actuators, the number of design variables reduces from 18 to 4 with the simplification assumption.

The physical explanation of the parameters to be optimized is presented schematically in Figure 4.10. The constraints or upper and lower bounds of these parameters are based upon the previous analysis (see Chapter 3) and limits related to hardware for possible implementation. The lowest value of the input frequency is 200 Hz which is the minimum possible frequency to cause part motion with the highest stroke of 200 μm. The 10000 Hz limit of upper frequency is easily achievable with piezoelectric actuators. The actuator spacing is based upon minimum size of piezoelectric actuator and the maximum value of distance travelled by a micropart from the individual analysis in chapter 3. The deformation wavelength in the analysis is assumed to be 600 μm. The minimum value of actuator spacing is assumed to be 500 μm which is smaller than the wavelength while the upper limit of the spacing is defined to be 1500 μm. The maximum stroke is set to 200 μm, a deformation easily attained with a piezo-actuator less than 8~10 mm length considering a 3% deformation. The minimum value of the time delay between the

firing of two consecutive actuators is 0 whereas its maximum value is selected high enough to cover the full spectrum of operation. The constraints on the parameters to be optimized are summarized in Table 4.1. All the design variables were defined to be continuous for optimization purposes. The first population generation is generated using random function generator ensuring that the population array covers the entire region of the parameter space with equal probability according to DE theory [56].

Table 4.1: Constraints on and type of design variables

Parameter	Type	Lower Limit	Upper Limit
Input Frequency	Continuous	200 Hz	10000 Hz
Actuator Spacing	Continuous	500 μm	1500 μm
Delay between the firing of two consecutive actuators	Continuous	0 sec	0.1 sec
Length of Stroke	Continuous	100 μm	200 μm

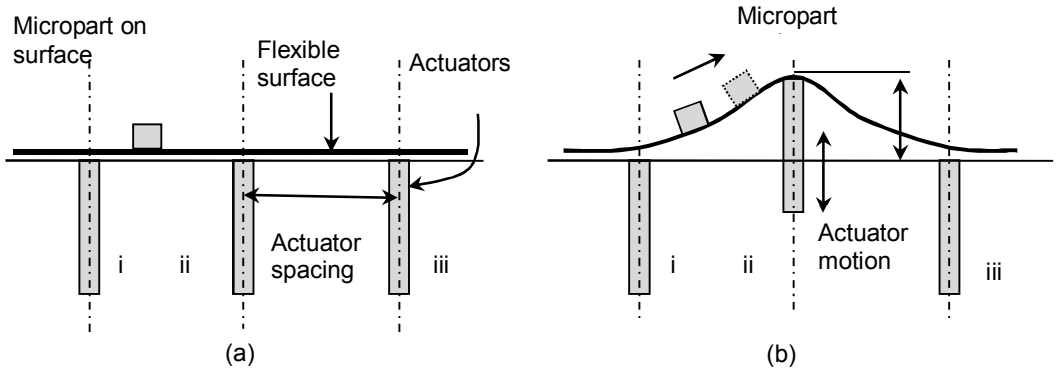

Figure 4.10: Schematic of microconveyor showing actuator spacing and length of stroke

4.8.3 *Cautionary steps*

The solution is evaluated for each population member subjected to the constraints. As the solution progresses, if a constraint is violated, the corresponding set of parameters is penalized accordingly and the population of the new generation is created. There are two types of constraints for this problem; the condition that the micropart must remain on the surface at all times and the nominal design variable constraints.

The micropart must remain attached to surface. The micropart motion is monitored continuously as well as the component of input acceleration perpendicular to the surface. The resultant inertia force

perpendicular to the surface is compared at each solution step with the minimum point at the “separation distance vs. applied load” shown in Figure 3.11. If the normal value of inertia force is higher than the maximum value of pull force required to separate the micropart from the surface, the micropart is considered detached. The population member which results into detachment is penalized with a fixed cost of 10^5.

The design variables should remain within predefined bounds. Considering the physical limitations of the problem, the upper and lower bounds of the design variables are defined. During the creation of a new generation and adding the weighted difference of two vectors in the third vector, according to DE theory, if any design variable outside the boundary of the feasible range is created, it is identified in the solution process and reset at a random point within the available bounds.

4.8.4 *Surface deformation profile*

The contour of the surface deformation profile is assumed to be Gaussian with a fixed wavelength of 0.6mm. This profile has been selected for its ease of differentiation and implementation (single differentiable equation and without discontinuities) even though any possible deformation profile could be used. The actuator firing delay is defined to be the time from the end of the reverse stroke of one (first) actuator to the start of forward stroke of subsequent (second) actuator and is assumed to always be greater than zero. A positive value of time delay between the actuator firing will eliminate "deformation overlap" and the instantaneous value of deformation will be due to a single actuator.

The material properties and the surface roughness characteristics are given in Table 4.2. Similar to the analysis in the previous chapters, the surface contact area is considered constant and the surface stretch is assumed to have no effect on the surface roughness characteristics.

Table 4.2: Parameters description and values

Description	Variable	Value
Surface roughness profile [26]	ϕ_z	Gaussian
Standard deviation of surface roughness	σ_n	20 nm
Surface area (contact area)	A_n	100μm x 100μm
Poisson's ratio	v	0.33
Plasticity index [37]	ψ	2.5
Difference in surface energy	Δγ	0.5 J/m^2
Hardness of material [37]	H	200 HB
Micropart mass	M	2 x 10-9 kg
Young modulus of surface in contact	E	2 x 1011 N/m^2

4.8.5 *Number of actuators*

The number of actuators in the array is assumed to be fixed and for the current optimization an array of five actuators is defined. This number of actuators is large enough that could locate the micropart to a target position of 10 mm as a linear combination of individual performance.

4.8.6 *Objective function and Cost*

DE is used to estimate the optimum values of the design variables to satisfy the objective of translocating a micropart to a predefined distance with minimum time. The initial and final velocities of the micropart are assumed to be zero. The target value is selected to be at 10 mm from the center position of first actuator while the initial position of the micropart is selected to be 0.15 mm with respect to the center of the first actuator.

The motion profile of the input to the actuator is assumed to be quintic (5^{th} order equation). This is the minimum order required to define initial and final values of position, velocity and acceleration. The initial and final values are set to be

$$h_i = 0;\ h_f = L$$
$$v_i = v_f = 0$$
$$a_i = a_f = 0 \qquad 4.2$$

where, *h* is the height of actuator stroke, *L* is the maximum length of actuator stroke, *v* is the velocity of actuator, and a is the acceleration of actuator; subscripts *i* and *f* refer to initial and final values respectively. These values are used to calculate the constants of the quintic actuator motion profile.

DE with slight jitter is used; jitter is added to avoid restricting the solution within possible local minima of the solution space [55]. The requirements of the objective function are met by defining a cost function as a combination of the deviation of the distance travelled by the micropart from the desired final location and the total time taken for the motion. The time is in units of seconds whereas the displacement is in meters. To generate a suitable cost function from these two parameters having different units, the final value of micropart displacement from the target position is normalized with an acceptable tolerance for the deviation of micropart from the target position T_d. To ensure that the final position of the micropart is within the given tolerance from the target, the effect of normalized deviation is amplified by raising it to a large power C. If the deviation of the final position of the micropart is within the predefined tolerance, the normalized deviation will be less than 1 and its effects strengthened with the large power resulting in a very small contribution in the overall cost. Contrary, if the micropart final location is outside the tolerance region, the normalized deviation will be greater than 1 and the large power will amplify the violation of this requirement in the cost function.

Travel time is added in the cost function with a simple multiplier weight *A* that is set according to the overall travel time of the micropart movement. In the current approach, the travel time is of the order of 0.1 sec. In order to add a significant contribution by the time in the cost function, and in fact the only contribution if the micropart is within the positioning tolerance limit, the constant *A* is set in the order of 10^3. The final form of the cost function is shown in equation (4.3).

$$Cost = A \times T_f + \left| \frac{X_f - X_{fd}}{T_d} \right|^C \qquad 4.3$$

where A and C are constants, T_d is the desired tolerance for the micropart placement, T_f is total time for the micropart to reach the final position. X_f is the final location of micropart and X_{fd} is the desired final position.

This cost function is minimized using the following parameters for the differential evolution implementation; Population Members = 50, Total Generations = 50, Crossover Probability = 0.8, and DE step size = 0.9. The crossover probability is kept high in order to generate the new combination of the population members and avoid local minima due to the discontinuity of the solution space.

Table 4.3: Converged values of design parameters

Parameter	Converged Values
Input Actuator Frequency	719 Hz
Actuator Spacing	500 μm
Delay between firing of two consecutive actuators	0.001 sec
Length of Stroke	178 μm

The optimization simulation using the defined parameters, design variable constraints and cost function was run. The cost convergence as function of iterations is shown in Figure 4.11. The generation history and convergence for each design variable is shown in Figure 4.12 while the converged values of the design variables are shown in Table 4.3. These values are within the limits defined for each design variable in Table 4.2. The initial cost is in the order of 10^9 with a major contribution from the deviation of tolerance constraint. The final cost is 18.5. The part reaches the desired location within the defined tolerance limit of ±50 μm of the target with the major contributor in the cost being due to time.

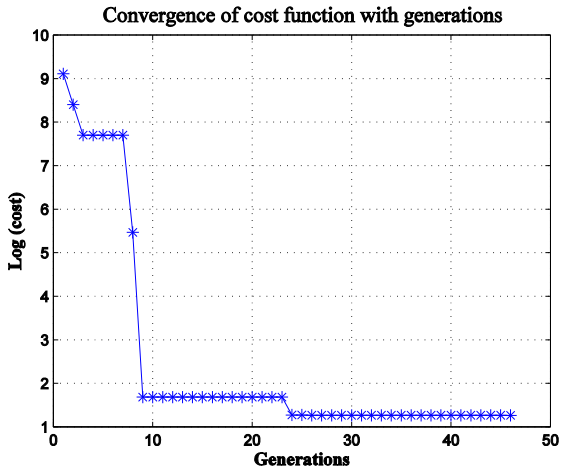

Figure 4.11: History of cost function vs. number of generations.

The estimated optimum values of the design variables were used as inputs to simulate the motion of the micropart. The micropart motion velocity and motion trace profile are plotted in Figure 4.13. The micropart velocity as function of time is shown in Figure 4.13(a) in which one could also observe the engagement of the micropart with the actuators in the microconveyor system.. The second actuator is timed in such a way to engage the moving micropart from the first actuator and accelerates it to further increase the velocity. The micropart interacts with the deformation by the third actuator which slightly reduces the velocity. The remaining downstream actuators do not energize and do not contribute to the motion of the micropart. The constant decrease in velocity is due to the constant value of friction force between the micropart and surface which eventually brings the micropart to standstill within the desired tolerance range. The trace of the micropart motion profile in the X-Y plane is shown in Figure 4.13(b); along the X-axis is the displacement and along the Y-axis is the height on the surface due to surface deformation. The three humps represent the interaction of first three actuators with the micropart. The micropart finally reaches 10.02 mm which is within the tolerance range of ±0.05 mm within the target position requiring only 0.037 second to complete the motion.

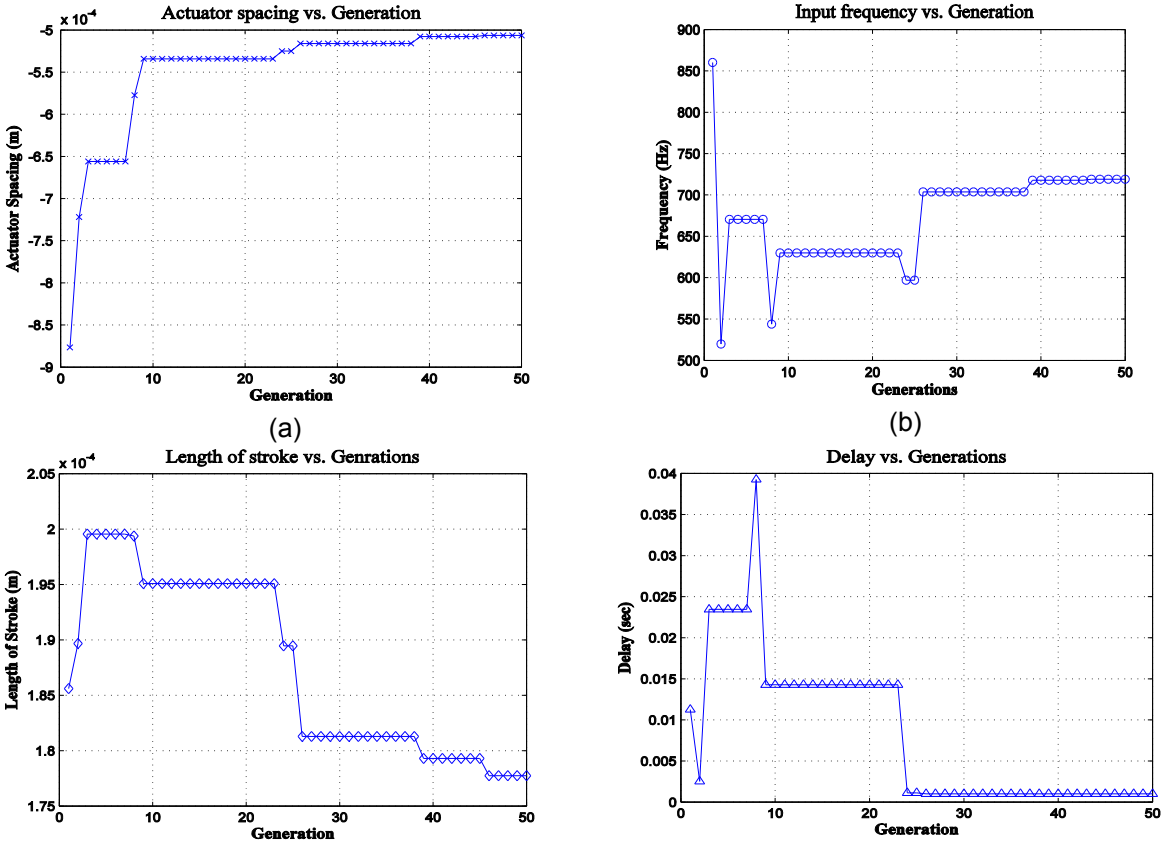

Figure 4.12: Convergence of each parameter as function of generation history. (a) Actuator spacing, (b) Input frequency, (c) Length of Stroke, and (d) Time delay between actuator firing

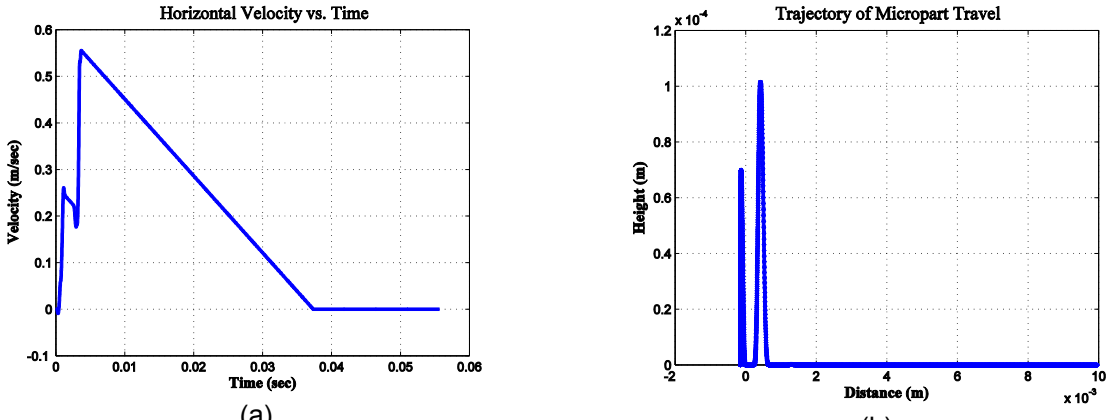

Figure 4.13: Micropart motion (a) Variation of horizontal component of velocity with time and (b) Micropart motion profile in X-Y plane

4.9 Conclusions

The continuous active surface concept for micropart manipulation requires the placement of microactuators in the form of an array to move the micropart from the given position to a required target position. While arranged in the form of an array, the downstream actuators could engage the micropart while is moving with an initial velocity. Depending on the instantaneous location and initial velocity, the actuators could either accelerate and/or decelerate the micropart. An optimization approach was employed to estimate the design variables for micropart manipulation with actuator arrays for any desired goal with a predefined tolerance while minimizing the time for accomplishing the task. The optimum solution for minimum time to reach a desired distance within a predefined tolerance with an array of five equally-spaced-actuators shows the acceleration and deceleration of micropart during its motion to reach the target position (Fig 4(a)). The optimized set of design variables takes full advantage of the acceleration and deceleration capability of actuators where the first two actuators accelerate the micropart while the third actuator decelerates it. Though consecutive actuators in the form of an array is a discontinuous problem which does not have any solution in the forward direction, the inverse of the problem can be solved using an optimization method such as DE and a set of design variables can be calculated to reach a desired target position. Moreover, it has been shown that placing actuators in a sequential array distances beyond the capability of a single actuator could be successfully reached.

CHAPTER 5

EFFECT OF SURFACE DEFORMATION ON SURFACE FRICTION AND MICROCONVEYOR PERFORMANCE

5.1 Introduction

The results and analysis presented in the previous chapters introduced the effects of surface roughness (friction force and friction coefficient) on the dynamics of motion along with the overall microconveyor concept and verified the feasibility of motion based on the assumption that the surface roughness remains constant even if the surface deforms. The proposed method is based on the concept of translocation of micropart due to controlled deformation of a flexible surface. The deformation of surface due to the microactuator motion and constraints imposed by the attached actuators causes a change on the length of the surface in the active zone thus causing a strain in the surface material as shown in Figure 5.1. This \strain affects the surface roughness; however the analysis already presented was based on the assumption that changes in the roughness characteristics can be ignored. However, the stretch of the surface changes the surface roughness and consequently it will affect the normal load and friction force. Thus, the effects of the dynamically changing surface roughness due to surface stretching must be analyzed and quantified as they relate to the micropart motion and positioning. In this chapter the effects of surface stretching on surface roughness and the system output are analyzed. Also, the output of the system as function of the variation of surface roughness due to surface stretching is also compared with the constant surface roughness one.

The beginning of this chapter will present existing work related to the change in surface roughness and data from related experiments. The formulation relating to the change of surface roughness to the surface stretch will be developed for metals. To accommodate the instantaneous value of surface roughness and resultant friction force, the required modifications in the previously developed friction and analysis logic for the numerical simulation will be discussed and the results will be presented. The chapter will end with a brief discussion and conclusions about the comparative results.

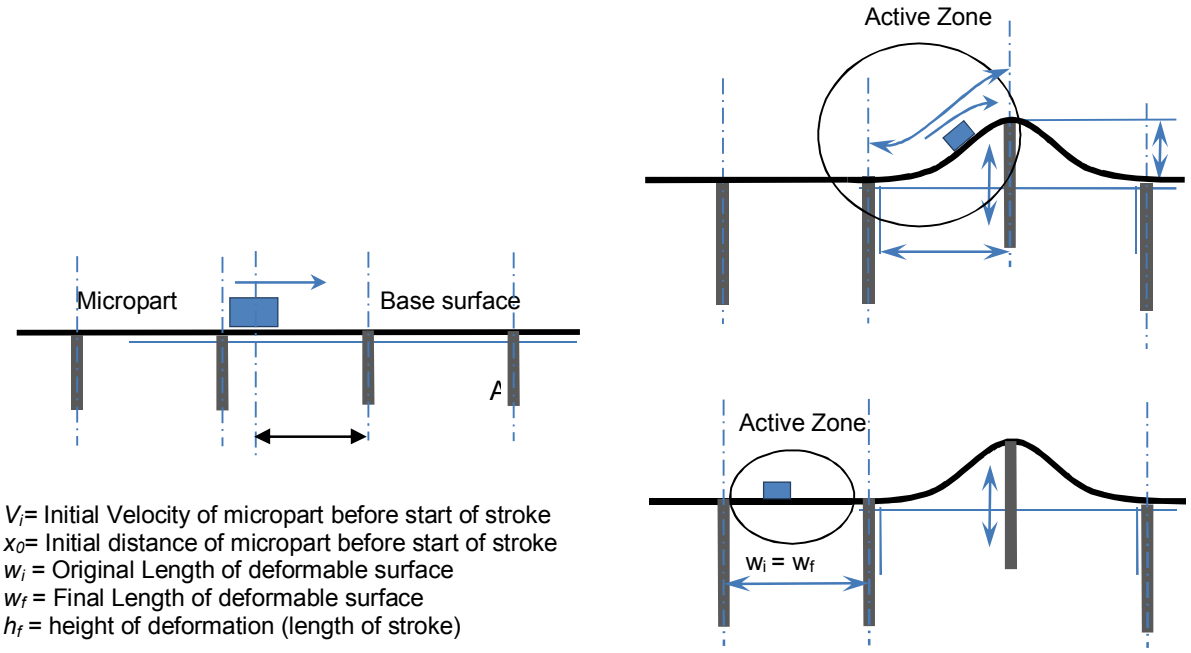

V_i= Initial Velocity of micropart before start of stroke
x_0= Initial distance of micropart before start of stroke
w_i = Original Length of deformable surface
w_f = Final Length of deformable surface
h_f = height of deformation (length of stroke)

Figure 5.1: The original surface and deformed configuration. The active zone is based on the location of micropart relative to the active actuators (a) all actuators are in retracted state, (b) surface stretched (encircled), (c) surface not stretched

5.2 Surface roughness and surface stretch

A rough surface consists of asperities arranged with a defined probability density function (PDF) which depends upon the manufacturing process [26]. Any strain along the surface will result in a strain in the lateral direction (along the thickness) affecting the characteristics of the surface asperities. The effect of surface stretching on the surface roughness has not been extensively investigated in the available literature. Only few experimental studies are available and they relate to the stretch of polymer sheets and its effect on surface roughness. Various types of polymers once strained along the surface exhibit different behavior in the change of surface roughness. Various blends of PVDF/PMMA were investigated in uniaxial and biaxial deformation mode for the change of surface roughness [60]. The surface profile initially gets rougher and then becomes smooth under uniaxial and biaxial stretch. The increase and decrease in roughness is a function of the ratio of the polymeric blend. The tribological behavior of aluminum during deep drawing was investigated by Azushima who found that under back pressure, stretching of the aluminum sheets affects its surface roughness characteristics [61]. No quantitative data

on the surface roughness change are mentioned for these experiments. In addition, the results from these experiments cannot be generalized and used to estimate the effect on the surface roughness by stretching an arbitrary metallic surface.

In addition, to the best of our knowledge no mathematical model was identified that could be employed to predict the quantifiable change in surface roughness as a function of surface strain. In this work, a simple model is proposed to estimate the surface roughness change as function of the surface strain based on the Poisson's ratio of the surface material. The proposed model is introduced, developed and implemented by augmenting the equivalent surface in contact with a flat surface as described in chapter 3. The strain along the surface has two effects on the characteristics of the asperities;

1. The strain along the surface will reduce the height of the asperities along the normal to the surface.
2. The strain along the surface will reduce the asperity density of the equivalent rough surface.

In addition, the surface stretch is assumed to be uniform along the part of the surface that undergoes motion or what is termed as the active zone. Also, the flexible surface is assumed to be thin and variation of stress along the thickness of the surface is neglected.

5.3 Post-stretch mean, standard deviation and asperity density

Consider a surface covered with spherical asperities as described in chapter 3 with a material Poisson ratio v. The original, before stretching, statistical characteristics of the asperities are defined as follows; y_m is the original value of mean of the asperity heights, σ_s is the standard deviation of asperity heights, and η represents the asperity density. A strain along the surface, ε, will affect the asperity statistical characteristics. The new parameters for asperity density, standard deviation and mean of asperity heights are given by η_n, σ_{sn}, and y_{mn} respectively. the new statistical parameters are estimated as functions of the pre-stretched parameters and characteristics as follows. The original mean of asperity heights is given by

$$y_m = \frac{y_1 + y_2 + ... + y_N}{N} = \sum_i^N y_i \qquad 5.1$$

where y_i represents the height of i^{th} asperity and N is the total number of asperities. The mean of asperity heights after stretching is similarly given by

$$y_{mn} = \frac{y_{1n} + y_{2n} + ... + y_{Nn}}{N} = \sum_{in}^N y_{in} \qquad 5.2$$

where y_{in} represents the new value of the i^{th} asperity height. The new value of the individual asperity height is calculated as the difference between the original height and change in height due to Poisson's ratio effect

$$y_{in} = y_i - y_i \nu\varepsilon = y_i\left(1 - \nu\varepsilon\right) \qquad (i = 1.....N) \qquad 5.3$$

Therefore, substituting (3) in (2) yields the new mean asperity height as

$$y_{mn} = \frac{y_1\left(1-\nu\varepsilon\right) + y_2\left(1-\nu\varepsilon\right) + ... + y_N\left(1-\nu\varepsilon\right)}{N} = \frac{\left(y_1 + y_2 + ... + y_N\right)\left(1-\nu\varepsilon\right)}{N} = y_m \times \left(1-\nu\varepsilon\right) \qquad 5.4$$

The standard deviation of the surface asperities before and after stretching are given by

$$\sigma_s = \sqrt{\frac{\sum_{i=1}^N \left(y_i - y_m\right)^2}{N-1}} \quad \text{and} \quad \sigma_{sn} = \sqrt{\frac{\sum_{i=1}^N \left(y_{in} - y_{mn}\right)^2}{N-1}} \qquad 5.5$$

Further manipulating, the after stretching standard deviation yields

$$\sigma_{sn} = \sqrt{\frac{\sum_{i=1}^N \left\{y_i \times \left(1-\nu\varepsilon\right) - y_m \times \left(1-\nu\varepsilon\right)\right\}^2}{N-1}} = \left(1-\nu\varepsilon\right) \times \sqrt{\frac{\sum_{i=1}^N \left(y_i - y_m\right)^2}{N-1}}$$
$$= \left(1-\nu\varepsilon\right) \times \sigma_s \qquad 5.6$$

The new value of asperity density is given by

$$\eta_n = \eta \times (1 - \varepsilon) \tag{5.7}$$

The percent reduction in the asperity density is the stain of the surface. The analysis presented and derived equations (5.1~5.7) indicates that the change in the standard deviation and mean of asperity height is a function of the material Poisson's ratio and the strain in the surface.

5.4 Post stretch asperity PDF

The above formulation shows that the spread of surface asperities will change with the application of strain along the surface. The new values of mean of asperity heights and its standard deviation are related to the old values, Poisson's ratio and induced strain. The only unknown is the type of spread after the surface stretch. If the surface asperities are assumed to be arranged in the form of a Gaussian distribution (before surface stretch), then after stretching, their distribution will remain Gaussian. The final height of each individual peak is given by equations (5.5), (5.6), and (5.7) showing that every member of the population is uniformly scaled by a fixed quantity, *(1-νε)*. It is assumed that the PDF of the asperities will remain Gaussian after stretching. The Gaussian distributions before, *f(y)*, and after. $f(y_n)$, stretching are given by

$$f_{(y)} = \frac{1}{\sigma\sqrt{2\pi}} e^{-\left(\frac{(y-y_m)^2}{2\sigma_s^2}\right)} \quad \text{and} \quad f_{(y_n)} = \frac{1}{\sigma_n\sqrt{2\pi}} e^{\left(\frac{-(y_n-y_{mn})^2}{2\sigma_{sn}^2}\right)} \tag{5.8}$$

Expanding the after stretching distribution and rearranging yields the after stretching PDF as function of the material Poisson's ratio and induced strain according to

$$f_{(y_n)} = \frac{1}{\sigma(1-\varepsilon\nu)\sqrt{2\pi}} e^{\left(\frac{-(y(1-\varepsilon\nu)-y_m(1-\varepsilon\nu))^2}{2(\sigma(1-\varepsilon\nu))^2}\right)} = \frac{1}{\sigma(1-\varepsilon\nu)\sqrt{2\pi}} e^{\left(\frac{-(y-y_m)^2}{2\sigma^2}\right)}$$
$$= \frac{1}{(1-\varepsilon\nu)} f_{(y)} \tag{5.9}$$

Thus, uniformly scaling a Gaussian population will not change the nature of the population, and the resultant population will remain Gaussian with the new values of mean and standard deviation as evaluated in (5.4) and (5.6).

5.5 Estimation of Post-Stretch Quantities

The procedure for evaluating the new value of the dynamically surface roughness since it is a function of the induced strain and its effects on the resultant friction force is introduced considering the instantaneous curvature of the deformed surface. In addition, the modifications to the original implementation procedure are discussed.

The time delay between firing of two consecutive actuators is larger than the time period of the actuator motion i.e. the deformation of two consecutive actuators will not overlap with each other. Therefore, the surface profile generated by individual actuators displacement will not overlap. In the one dimensional case, the exact solution of the surface deformation profile due to a single actuator displacement input at the center with both ends fixed as shown in the active zone in Figure 5.1(b), can be calculated in closed form using beam theory. The fixed endpoint boundary conditions are defined based on the fact that the flexible surface is attached to the actuator tips. Therefore, the boundary conditions are defined to have zero displacement and zero slope.

The identified closed form solution, based on beam theory, for the surface deformation is used to estimate the instantaneous value of the linear "surface" deformation at the micropart location. The boundary conditions for beam deflection are shown in Figure 5.2 with the closed form solution given by equation (5.10) [62]

$$
\begin{aligned}
h_x &= \frac{Px^2}{48EI}\left(3l-4x\right) \\
h_f &= \frac{Pl^3}{192EI} \Rightarrow P = h_f \frac{192EI}{l^3} \\
h_x &= \left(h_f \frac{192EI}{l^3}\right)\frac{x^2}{48EI}\left(3l-4x\right) = h_f \frac{4x^2}{l^3}\left(3l-4x\right)
\end{aligned}
\qquad 5.10
$$

where h_x is the deflection along the length of beam at distance *x*, *P* is the load at the center, *E* is material modulus, *I* is moment of inertia, and *l* is length of beam. h_f is the deflection of the beam at the center (between two actuators) which is the instantaneous value of the actuator stroke.

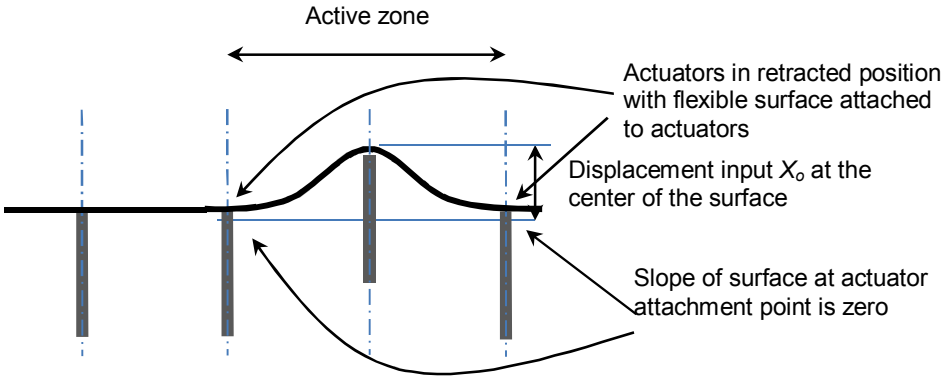

Figure 5.2: 1-D deformation of a surface is equivalent to the deformation of a beam with both sides clamped and displacement in center

5.6 Evaluation of surface strain

The induced surface strain is estimated only in the active zone as shown in Figure 5.2 and assumed to be instantaneously uniform in the active zone. In realizing a microconveyor, it is assumed that each actuator is attached to the surface and the motion of the surface at the point of contact is restricted along the surface. Therefore, the strain due to surface stretch is assumed to be local and the rest of the surface will remain undisturbed. The length of the curve of the deformed surface shape is estimated by integrating the surface deformation profile equation (5.10). The strain is evaluated by evaluating the difference between the curve length and original zone length (or distance between two actuators). The curve length is calculated by numerically evaluating the integral in equation (5.11) [63]

$$s = \int \sqrt{1 + \left(h_x'\right)^2}\, dx \qquad 5.11$$

where h_x' is the slope of the deflection of the beam and *s* is the curve length. The strain along the surface is given by

$$\varepsilon = \frac{s - s_o}{s_o} \qquad 5.12$$

where s_o is the original length of surface with the actuator in fully retracted position. Using this estimated value of strain along the surface and the roughness of the "equivalent surface" in the original configuration, the new value of surface roughness is estimated using equations (5.4) and (5.6). The instantaneous value of asperity density is estimated using equation (5.7).

The friction force is estimated using the mean distance between the micropart surface and deformed surface following the same procedures employed when the deformed surface was assumed not to affect the surface roughness. The mean distance between the surfaces is a function of the instantaneous value of PDF of asperity peaks and external applied load. This mean distance is obtained from the inversion of the "Applied load vs. Separation Distance" data and curve fitting of the inverted data. In the case of a continuously varying PDF and under the same applied load, the mean distance between the surfaces will continuously vary which will result in the need to continuously generate data and develop inverted "Applied load vs. Separation Distance" plots to be used to estimate the a continuously varying friction force.

In the numerical simulation to predict the micropart motion, each time step will correspond to new value of actuator height and a change in surface strain. Therefore, every integration time step will correspond to a new PDF of surface asperities, requiring a new set of data to be inverted and curve-fitted to estimate the new value of mean distance between the surface and micropart using the current value of external load applied on the micropart. This curve fitting is difficult to automate as the curve fitting needs to be precise in the vicinity of zero loads even though a low quality fit could be acceptable at higher loads. This issue is addressed by developing a priori and later using tabulated data of mean distance as function of the applied load for various predetermined values of surface roughness. This range is defined based on the surface material properties and estimated actuator stroke.

Instead of using a single equation to estimate the separation distance as was the case with a fixed value of PDF of asperity peaks, a 2-D linear interpolation is applied to estimate the mean distance

between the two surfaces for the instantaneous values of surface roughness and external applied load. The sample of the input data for the above mentioned interpolation is shown in Figure 5.3. The data in Figure 5.3 were generated by considering the values for surface roughness and force found in the case where the surface stretch does not affect the surface roughness. The KE model introduced in chapter 3 is used to evaluate the applied force as a function of surface roughness and mean separation distance. This 2-D linear interpolation is employed as it provides for faster numerical implementation and execution and can be repeatedly computed in the simulation without consuming large CPU time. Once the value of the separation distance between the surfaces is known, equation (3.31) is used to calculate the friction force between the two surfaces.

5.7 Estimation of Micropart detachment

The detachment of the micropart from the surface, as was the case with constant surface roughness, is established by comparing the component of inertial force perpendicular to the surface with the maximum force required to separate the two surfaces represented by point A in Figure 3.11. Unlike the constant surface roughness case, in the case of variable surface roughness, the threshold force cannot be a simple point to compare with the inertial force on the micropart.

The data matrix generated for the estimation of the mean separation distance between the surfaces as a function of surface roughness and applied force (shown in Figure 5.3) is used to estimate the detachment of the micropart from the surface. The separation distance value at the minimum point for the “Separation Distance vs. Applied Load” graph for each considered roughness value is evaluated and is shown in Figure 5.3 by the solid line. The corresponding value of the applied load represents the value at which detachment of the micropart at the corresponding surface roughness takes place. The dotted line represents the minimum applied load required to cause the micropart to detach from the surface as a function of the change of surface roughness. This applied load will be used to estimate the corresponding mean separation distance between the surfaces.

The data matrix consists of discrete points of separation distance as function of force and surface roughness. These discrete points could be curve fitted and used to estimate the separation distance as

function of force and surface roughness values in the domain examined as shown with the dotted line. However, the generated data indicates discontinuities; a closer examination of the data shows that a curve that passes through all the separation distance data points it also encompasses regions in which micropart detachment has already occurred and indicated with the letter D. Thus, interpolation could not be performed for the points at which detachment already took place. Therefore, a slightly more conservative data set is employed to identify a curve fit. This new data set is shown with a solid line in Figure 5.3. Any interpolation above this line will be valid and would generate a valid result on the data matrix. The effect of this slight shift or conservative set will be a negligible decrease in the upper limit of the feasible frequency range.

The curve fit equation for the detachment of a micropart under variable surface roughness is given by

$$f_d = \left(0.0556\times10^{-3}\sigma_n^3 - 3.262\sigma_n^2 + 65.31\sigma_n - 449.9\right)\times10^{-6}\ \text{N} \tag{5.13}$$

where, σ_n represents the standard deviation of the instantaneous value of surface roughness and f_d represents the maximum force required to detach the micropart from the surface.

Roughness (St Dev)	14	15	16	17	18	19	20
Force (N)							
-0.0000045	45.8818	50.6244	55.4451	60.3754	65.3953	70.6641	76.3922
-0.0000050	45.9235	50.6947	55.5611	60.5434	65.6484	71.048	77.0519
-0.0000055	45.9652	50.7651	55.6772	60.7114	65.9239	71.4925	77.9199
-0.0000060	46.0104	50.8354	55.7932	60.8793	66.2299	72.0364	79.2387
-0.0000065	46.0729	50.9057	55.9093	61.0687	66.5569	72.88	D
-0.0000070	46.1355	50.9761	56.0349	61.3123	66.9369	73.7718	D
-0.0000075	46.1981	51.0685	56.1948	61.556	67.3823	79.1973	D
-0.0000080	46.2606	51.1723	56.3548	61.7997	67.915	D	D
-0.0000085	46.3232	51.276	56.5147	62.0631	68.6971	D	D
-0.0000090	46.3858	51.3798	56.6746	62.4172	69.9039	D	D
-0.0000095	46.4483	51.4836	56.8346	62.7714	D	D	D
-0.0000100	46.5109	51.5874	56.9945	63.1946	D	D	D
-0.0000105	46.5735	51.6911	57.2322	63.7437	D	D	D
-0.0000110	46.636	51.7949	57.4727	64.6866	D	D	D
-0.0000115	46.6986	51.8987	57.7131	66.4422	D	D	D
-0.0000120	46.7612	52.0039	57.9536	D	D	D	D
-0.0000125	46.8237	52.1694	58.3123	D	D	D	D
-0.0000130	46.8863	52.3349	58.6993	D	D	D	D
-0.0000135	46.9489	52.5004	59.1455	D	D	D	D
-0.0000140	47.0178	52.6659	59.798	D	D	D	D
-0.0000145	47.1153	52.8314	62.0806	D	D	D	D
-0.0000150	47.2128	52.9969	D	D	D	D	D
-0.0000155	47.3103	53.2456	D	D	D	D	D
-0.0000160	47.4078	53.4959	D	D	D	D	D
-0.0000165	47.5053	53.7461	D	D	D	D	D
-0.0000170	47.6028	53.9964	D	D	D	D	D
-0.0000175	47.7003	54.4471	D	D	D	D	D
-0.0000180	47.7977	54.9007	D	D	D	D	D
-0.0000185	47.8952	57.3628	D	D	D	D	D
-0.0000190	47.9927	D	D	D	D	D	D
-0.0000195	48.149	D	D	D	D	D	D
-0.0000200	48.31	D	D	D	D	D	D
-0.0000205	48.4709	D	D	D	D	D	D
-0.0000210	48.6319	D	D	D	D	D	D
-0.0000215	48.7929	D	D	D	D	D	D
-0.0000220	48.9539	D	D	D	D	D	D
-0.0000225	49.2242	D	D	D	D	D	D
-0.0000230	49.5383	D	D	D	D	D	D
-0.0000235	49.8525	D	D	D	D	D	D
-0.0000240	50.3413	D	D	D	D	D	D
-0.0000245	50.9849	D	D	D	D	D	D

Figure 5.3: Separation distance data (in nm) for interpolation of the applied force and standard deviation of surface roughness; detachment force in Newton, and standard deviation of surface roughness in nm. Note that D indicates micropart detachment.

5.8 Numerical Implementation

The numerical implementation of the effects of the changing surface roughness due to surface deformation in the previously developed numerical approach of micropart motion are incorporated by evaluating the local strain at every time instant. Using the position of micropart at the current time instant and considering the local value of actuator position, the deformation of the surface is estimated within that active zone assuming that the strain is uniform within the active zone.

Subsequently, using the estimated value of the local strain, new values of PDF of asperity heights and asperity density are evaluated using equations (5.6) and (5.7). The actuator motion profile is used to calculate the local value of surface acceleration. This surface acceleration is used to calculate the local inertia force perpendicular to surface and the value of applied load normal to the surface. Employing the instantaneous values of applied normal load, the 2-D matrix (shown in Figure 5.3) is interpolated to estimate the mean distance between the two surfaces as function of the estimated values of the instantaneous applied load and the standard deviation of asperity heights. This value of mean distance between the two surfaces is used along with the new asperity density to estimate the current value of friction force.

This information of the new friction force is processed though the remaining numerical approach (Figure 3.9 in chapter 3) to estimate the micropart motion considering the newly estimated friction force. The flowchart for the variable friction force evaluation process is shown in Figure 5.4.

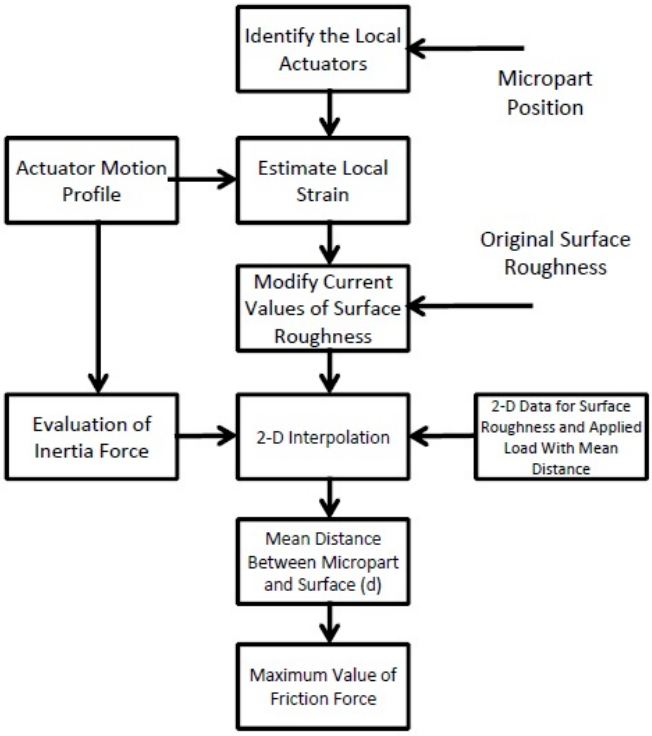

Figure 5.4: Flowchart for variable friction force evaluation between the two surfaces due to surface roughness changes

5.9 Results

The results from the numerical simulation with variable friction force are presented in Figure 5.5. The corresponding results of the system output assuming non-variable surface roughness and the output with variable surface roughness are shown on the same plot for comparison purposes. The comparison of the two graphs shows similar behavior. However, a small difference between the two configurations is observed with the variable surface roughness based results showing higher output compared with the constant surface roughness. Figure 5.5(a) shows the comparison of the horizontal velocity. The behavior of the system depicted in this plots was explained in chapter 3 (Figure 3.16(b)) and chapter 4 (Figure 4.8). The effect of reduced surface roughness due surface stretching results into larger magnitude velocity compared with the case when the surface roughness is constant. Figure 5.5(b) shows the comparison of the micropart displacement over the whole range of feasible frequencies. The variable surface roughness

results in greater displacements at all values of feasible frequencies as compared to the constant surface roughness case.

In addition, considering the small difference of displacement for both cases of constant and variable surface roughness, the assumption of constant surface roughness is valid for evaluation of micropart motion on a flexible surface.

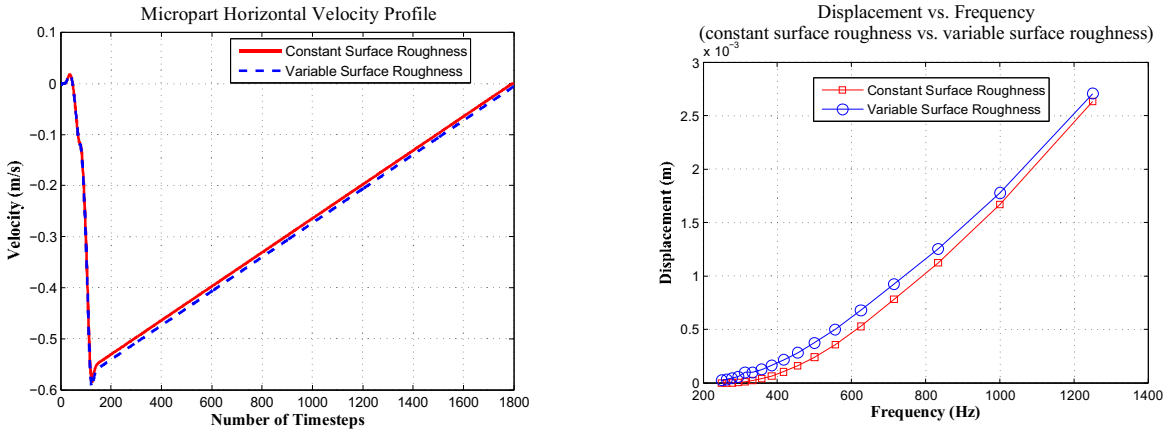

(a) (b)

Figure 5.5: Comparison of system output with variable surface roughness and constant surface roughness: (a) velocity profile comparison and (b) comparison of displacement against frequency

5.10 Conclusions

The comparative analysis of a microconveyor system with constant and variable surface roughness as the result of surface stretch shows that the displacement of the micropart is slightly larger when the effects of the surface stretch are considered. This is due to the fact that the surface stretch reduces the asperity density and the spread of asperities on the plane surface which in turn generates lower friction force between the two mating surfaces. The lower friction force results into a larger displacement of the micropart compared with the case of constant and larger surface roughness that yields higher friction force. However the small difference between the two formulations indicating that the micropart displacement with the assumption of constant roughness could be employed for the realization of a microconveyor.

CHAPTER 6

CONCLUSIONS AND FUTURE WORK

In this research a detailed analysis has been performed towards the realization of a micromanipulation or a microconveyor system in a dry friction environment considering the effects that dynamically changing microforces have on the micropart motion. A literature review was performed to identify the limitations of existing micropart manipulation techniques, in order to define the requirements and capabilities of the proposed new approach for micropart manipulation. A microconveyor is a system which has the ability to controllably translocate a micropart to a predefined location within the domain of operation and without direct contact between the micropart and actuators based on the active surface concept.

The dynamics of induced motion on a micropart on a carrier flexible surface is modeled while the surface undergoes controlled deformation by a single or multiple microactuators. At the microscale, the micropart weight is a negligible quantity compared with the surface forces, (van der Waals, Casimir, capillary and electrostatic forces) acting on the microparts. The mathematical model describing the forces acting on the micropart has been developed considering the relative significance of the surface forces which are strongly influenced by surface roughness, the characteristics of materials (surface and micropart) in contact and the mean distance between the surfaces (surface and micropart) in contact. A numerical methodology is developed to study through the mathematical model the dynamic effects of varying surface forces and the resultant friction force. Contact mechanics based surface roughness and friction model (based on the friction model proposed by Kogut and Etsion) are employed for the instantaneous evaluation of surface attraction and friction forces between the micropart and the carrier surface, and the magnitude of the forces are evaluated at each time step using the externally applied loads on the micropart which changes the mean distance between the in-contact surfaces. The surface roughness and friction model is inverted to evaluate the mean distance between the surfaces in-contact

for a given value of applied load at each integration time step. The discontinuity of coefficient of friction and the nonlinearity of the friction force are dynamically incorporated in the system model through a set of logical/conditional statements in the numerical methodology.

Using the developed mathematical model and numerical methodology, the motion patterns for the micropart movement are analyzed as a first step towards the realization of the proposed micromanipulation workcell. A qualitative and quantitative sensitivity analysis for the motion of the micropart is performed to estimate the most influential parameters on the micropart motion. The overall behavior of an array of actuators is explored by first analyzing the performance of a single actuator system for a range of micropart initial velocity and initial location of micropart relative to actuator. The single actuator study provided the foundation for extending to a multiactuator system or a linear array of actuators. The effects an array of actuators has on the micropart are estimated and analyzed. A genetic algorithm based numerical optimization methodology called differential evolution (DE) is used to estimate the optimum set of system control parameters to accomplish a desired task with given constraints. The effect of surface stretch on the surface roughness has been analyzed in detail along with the development of a mathematical model. Incorporating this model in the overall numerical approach, the effects of surface stretch on the micropart motion are estimated.

The conclusions and contributions from this research are presented in a tabulated form as follows:

- The motion of a micropart under controlled deformation of a flexible carrier surface is feasible.
- The dynamics of the micropart motion are a highly nonlinear and non-differentiable system which cannot be solved to identify in closed form an equation for the system output, thus numerical techniques must be employed.
- Under the influence of surface attraction forces, with weight being a negligible parameter, the motion pattern for micropart movement is counterintuitive; a micropart resting on a surface

that is controllably deformed by a single actuator tends to move towards the center of deformation instead of moving down towards the valley.

- There is always a feasible frequency range to operate the workcell; the micropart will not move if the operating frequency is below a minimum value and will detach from the surface (becomes airborne) if the operating frequency is larger than the maximum permissible value.
- Motion of the micropart is heavily influenced by the surface bonding energy and surface roughness; surface roughness is one of the most important parameters in micromanipulation and strongly influences the surface forces of attraction and friction force.
- The response generated by an array of actuators is not a simple linear combination of each individual actuator since the engaging micropart velocity by a consecutive must be considered.
- Depending upon the micropart initial velocity, the effect of an actuator can change from an accelerating mechanism to a decelerating device.
- For a multi actuator system, the range of feasible frequencies is a function of micropart engaging velocity and relative location to the actuator.
- The system response is negligibly affected by the variation of surface roughness due to strain along the surface; strain along the carrier surface is accommodated dynamically in the system dynamic model indicating that a constant surface roughness profile is a valid assumption to model system dynamics.

6.1 Future work

The dynamics of micropart motion has already been developed and used to evaluate the feasibility of the proposed approach, the system performance and the microconveyor response for a number of control and system parameters. It is recommended that this research work be extended in the following research directions:

- It is recommended that a verification of the proposed microconveyor system is further explored and verified through controlled experimentation.
- The developed numerical methodology is applicable to a 1-D motion analysis. It is recommended that the analysis be extended to 2-D microconveyor by considering the system as a surface instead of a line.
- In the current dynamic model the surface of the workcell is considered rigid along its thickness and assumes that the acceleration at the top of the surface is the same as the one imparted at the bottom of the surface by the attached microactuator; it is recommended that through the thickness compliance be studied and incorporated in the model if 'soft' or ‘thick’ materials are used for the carrier surface.
- In the case of a multiactuator system, it is recommended that the system performance (micropart translocation) is improved through an optimization approach to identify the optimum surface geometry while considering the constraints and capabilities of random actuator firing.

REFERENCES

1. Gauthier, M. and S. Régnier, *Robotic micro-assembly*. 2010: Wiley-IEEE Press.
2. El-Badry, H.M., *Micromanipulators and micromanipulation*. Vol. 3. 1963: Academic Press.
3. Goto, T., et al. *Compact packaging by robot with tactile sensors*. 1972.
4. Grossman, D.D. and M.W. Blasgen, *Orienting mechanical parts by computer-controlled manipulator.* Systems, Man and Cybernetics, IEEE Transactions on, 1975(5): p. 561-565.
5. Erdmann, M.A. and M.T. Mason, *An exploration of sensorless manipulation.* Robotics and Automation, IEEE Journal of, 1988. 4(4): p. 369-379.
6. Hitakawa, H., *Advanced parts orientation system has wide application.* ASSEMBLY AUTOM., 1988. 8(3): p. 147-150.
7. Erdmann, M., M.T. Mason, and G. Vaněček, *Mechanical parts orienting: The case of a polyhedron on a table.* Algorithmica, 1993. 10(2): p. 226-247.
8. Goldberg, K.Y., *Orienting polygonal parts without sensors.* Algorithmica, 1993. 10(2): p. 201-225.
9. Böhringer, K.F., B.R. Donald, and N.C. MacDonald. *Upper and lower bounds for programmable vector fields with applications to MEMS and vibratory plate parts feeders*. 1996. Citeseer.
10. Böhringer, K.F., et al., *Algorithms for sensorless manipulation using a vibrating surface.* Algorithmica, 2000. 26(3): p. 389-429.
11. Bohringer, K.F., et al. *A theory of manipulation and control for microfabricated actuator arrays*. 1994. IEEE.
12. Goyal, S. and A. Ruina, *Relation between load and motion for a rigid body sliding on a planar surface with dry friction: Limit surfaces, incipient and asymptotic motion.* Wear, 1988.
13. Suh, J.W., et al. *Combined organic thermal and electrostatic omnidirectional ciliary microactuator array for object positioning and inspection*. 1996.

14. Jacobson, J., et al., *Integrated force arrays: Theory and modeling of static operation.* Microelectromechanical Systems, Journal of, 1995. 4(3): p. 139-150.

15. Fujita, H., M. Ataka, and S. Konishi. *Cooperative work of arrayed microactuators*. 1994. IEEE.

16. Pister, K.S.J., R.S. Fearing, and R.T. Howe. *A planar air levitated electrostatic actuator system*. 1990. IEEE.

17. Furuhata, T., T. Hirano, and H. Fujita. *Array-driven ultrasonic microactuators*. 1991. IEEE.

18. Turitto, M., Y.A. Chapius, and S. Ratchev, *Pneumatic Contactless Feeder for Microassembly.* Precision Assembly Technologies for Mini and Micro Products, 2006: p. 53-62.

19. Rollot, Y., S. Régnier, and J.C. Guinot, *Simulation of micro-manipulations: Adhesion forces and specific dynamic models.* International journal of adhesion and adhesives, 1999. 19(1): p. 35-48.

20. Zhou, S.A., *On forces in microelectromechanical systems.* International journal of engineering science, 2003. 41(3): p. 313-335.

21. LI, G., Y. PENG, and X. ZHANG, *Analysis of micro-forces between micro-parts and their influence factors in MEMS.* 哈尔滨工业大学学报 (英文版), 2008: p. 02.

22. Savia, M. and H.N. Koivo, *Contact micromanipulation—Survey of strategies.* Mechatronics, IEEE/ASME Transactions on, 2009. 14(4): p. 504-514.

23. Israelachvili, J.N., *Intermolecular and Surface Forces: Revised Third Edition*. 2011: Academic press.

24. Burton, Z. and B. Bhushan, *Hydrophobicity, adhesion, and friction properties of nanopatterned polymers and scale dependence for micro-and nanoelectromechanical systems.* Nano letters, 2005. 5(8): p. 1607-1613.

25. Lowell, J. and A. Rose-Innes, *Contact electrification.* Advances in Physics, 1980. 29(6): p. 947-1023.

26. Greenwood, J. and J. Williamson, *Contact of nominally flat surfaces.* Proceedings of the Royal Society of London. Series A. Mathematical and Physical Sciences, 1966. 295(1442): p. 300.

27. Liu, G., Q. Wang, and C. Lin, *A survey of current models for simulating the contact between rough surfaces.* Tribology transactions, 1999. 42(3): p. 581-591.

28. Fischer-Cripps, A.C., *Introduction to contact mechanics*. 2000: Springer Verlag.

29. Hertz, H., *Miscellaneous papers*. 1896: Macmillan.

30. Johnson, K., K. Kendall, and A. Roberts, *Surface energy and the contact of elastic solids.* Proceedings of the Royal Society of London. A. Mathematical and Physical Sciences, 1971. 324(1558): p. 301.

31. Derjaguin, B., V. Muller, and Y.P. Toporov, *Effect of contact deformations on the adhesion of particles.* Journal of Colloid and interface science, 1975. 53(2): p. 314-326.

32. Maugis, D., *Adhesion of spheres: the JKR-DMT transition using a Dugdale model.* Journal of Colloid and interface science, 1992. 150(1): p. 243-269.

33. Morrow, C., M. Lovell, and X. Ning, *A JKR–DMT transition solution for adhesive rough surface contact.* Journal of Physics D: Applied Physics, 2003. 36: p. 534.

34. Greenwood, J. and J. Tripp, *The contact of two nominally flat rough surfaces.* Proceedings of the Institution of Mechanical Engineers, 1970. 185(1): p. 625-633.

35. Tabor, D., *The hardness of solids.* Review of Physics in Technology, 1970. 1: p. 145.

36. Fuller, K. and D. Tabor, *The effect of surface roughness on the adhesion of elastic solids.* Proceedings of the Royal Society of London. A. Mathematical and Physical Sciences, 1975. 345(1642): p. 327-342.

37. Chang, W., I. Etsion, and D. Bogy, *An elastic-plastic model for the contact of rough surfaces.* Journal of tribology, 1987. 109: p. 257.

38. Chang, W., I. Etsion, and D. Bogy, *Adhesion model for metallic rough surfaces.* Journal of tribology, 1988. 110: p. 50.

39. Chang, W., I. Etsion, and D. Bogy, *Static friction coefficient model for metallic rough surfaces.* Journal of tribology, 1988. 110: p. 57.

40. Zhao, Y., D.M. Maietta, and L. Chang, *An asperity microcontact model incorporating the transition from elastic deformation to fully plastic flow.* Journal of tribology, 2000. 122: p. 86.

41. Johnson, K.L., *Contact mechanics*. 1987: Cambridge Univ Pr.

42. Handzel-Powierza, Z., T. Klimczak, and A. Polijaniuk, *On the experimental verification of the Greenwood-Williamson model for the contact of rough surfaces.* Wear, 1992. 154(1): p. 115-124.

43. Kucharski, S., et al., *Finite-elements model for the contact of rough surfaces.* Wear, 1994. 177(1): p. 1-13.

44. Kogut, L., *Elastic-plastic contact analysis of a sphere and a rigid flat.* Journal of Applied Mechanics, 2002. 69: p. 657.

45. Kogut, L. and I. Etsion, *A semi-analytical solution for the sliding inception of a spherical contact.* Journal of tribology, 2003. 125(3): p. 499-506.

46. Kogut, L. and I. Etsion, *Adhesion in elastic-plastic spherical microcontact.* Journal of Colloid and interface science, 2003. 261(2): p. 372-378.

47. Kogut, L. and I. Etsion, *A static friction model for elastic-plastic contacting rough surfaces.* Transactions-American Society Of Mechanical Engineers Journal Of Tribology, 2004. 126(1): p. 34-40.

48. Feng, M. and T. Kenjo, *Friction and wear of spindle motor hydrodynamic bearings for information storage systems during startup and shutdown.* Microsystem technologies, 2007. 13(8): p. 987-997.

49. Bhushan, B., *Contact mechanics of rough surfaces in tribology: multiple asperity contact.* Tribology Letters, 1998. 4(1): p. 1-35.

50. Mao, K., Y. Sun, and T. Bell, *A numerical model for the dry sliding contact of layered elastic bodies with rough surfaces.* Tribology transactions, 1996. 39(2): p. 416-424.

51. Oden, J. and J. Martins, *Models and computational methods for dynamic friction phenomena.* Computer methods in applied mechanics and engineering, 1985. 52(1-3): p. 527-634.

52. Levinson, O., G. Halperin, and M. Varenberg, *Experimental investigation of the elastic–plastic contact area and static friction of a sphere on flat.* Journal of tribology, 2005. 127: p. 47.

53. Yoon, E.S., et al., *The effect of contact area on nano/micro-scale friction.* Wear, 2005. 259(7-12): p. 1424-1431.

54. Woods, R., Professor Department of Mechanical and Aerospace Engineering, UTA 2010 Personal Communication.

55. Price, K.V., R.M. Storn, and J.A. Lampinen, *Differential evolution: a practical approach to global optimization*. 2005: Springer-Verlag New York Inc.

56. Fleetwood, K., *An introduction to differential evolution*, 2010.

57. Babu, B. and R. Angira. *Optimization of non-linear functions using evolutionary computation*. 2001. Citeseer.

58. Babu, B. and S. Munawar. *Differential evolution for the optimal design of heat exchangers*. 2010.

59. Onwubolu, G.C. and B. Babu, *New optimization techniques in engineering*. Vol. 141. 2004: Springer Verlag.

60. Zhou, X. and M. Cakmak, *Stress–strain behavior as related to surface topography and thickness uniformity in uni-and biaxially stretched PVDF/PMMA blends.* Polymer Engineering & Science, 2007. 47(12): p. 2110-2117.

61. Azushima, A. and M. Sakuramoto, *Effects of plastic strain on surface roughness and coefficient of friction in tension-bending test.* CIRP Annals-Manufacturing Technology, 2006. 55(1): p. 303-306.

62. Hibbeler, R., *Statics and mechanics of materials*. 2004.

63. Do Carmo, M.P., *Differential geometry of curves and surfaces*. Vol. 1. 1976: Prentice-Hall Englewood Cliffs, NJ.

BIOGRAPHICAL INFORMATION

Mohsin Rizwan got his bachelor's degree in Mechanical Engineering from University of Engineering and Technology Lahore in 2001. After having five years' experience in design and manufacturing industry, he joined UTA as master's student in 2006. In summer 2008, he transferred from master's program to fast track BS to PhD.

He is recipient of several awards including National Talent Scholarship (Pakistan), STEM Doctoral Fellowship, Graduate School Dissertation Fellowship and university scholar for year 2010-2011. His research interests include the mathematical modeling of microscale systems, system optimization and MEMS controls. He plans to join faculty position and continue the research in the areas of MEMS and system modeling.